Delft University of Technology

Fingerprinting the Properties of WS_2 Nanostructures using Advanced Transmission Electron Microscopy Techniques

From Growth to Characterization

van Heijst, S.E.

DOI
10.4233/uuid:b9cf52ab-06fa-40bf-882e-96a72d8e234d

Publication date
2024

Document Version
Final published version

Citation (APA)
van Heijst, S. E. (2024). *Fingerprinting the Properties of WS_2 Nanostructures using Advanced Transmission Electron Microscopy Techniques: From Growth to Characterization*. [Dissertation (TU Delft), Delft University of Technology]. https://doi.org/10.4233/uuid:b9cf52ab-06fa-40bf-882e-96a72d8e234d

Important note
To cite this publication, please use the final published version (if applicable).
Please check the document version above.

Copyright
Other than for strictly personal use, it is not permitted to download, forward or distribute the text or part of it, without the consent of the author(s) and/or copyright holder(s), unless the work is under an open content license such as Creative Commons.

Takedown policy
Please contact us and provide details if you believe this document breaches copyrights.
We will remove access to the work immediately and investigate your claim.

This work is downloaded from Delft University of Technology.
For technical reasons the number of authors shown on this cover page is limited to a maximum of 10.

Fingerprinting the Properties of WS_2 Nanostructures using Advanced Transmission Electron Microscopy Techniques

From Growth to Characterization

Sabrya Esther van Heijst

FINGERPRINTING THE PROPERTIES OF WS_2 NANOSTRUCTURES USING ADVANCED TRANSMISSION ELECTRON MICROSCOPY TECHNIQUES

FROM GROWTH TO CHARACTERIZATION

FINGERPRINTING THE PROPERTIES OF WS_2 NANOSTRUCTURES USING ADVANCED TRANSMISSION ELECTRON MICROSCOPY TECHNIQUES

FROM GROWTH TO CHARACTERIZATION

Proefschrift

ter verkrijging van de graad van doctor
aan de Technische Universiteit Delft,
op gezag van de Rector Magnificus prof. dr. ir. T.H.J.J. van der Hagen,
voorzitter van het College voor Promoties,
in het openbaar te verdedigen op vrijdag 3 mei 2024 om 12:30 uur

door

Sabrya Esther VAN HEIJST

Master of Science in Applied Physics,
Technische Universiteit Delft, Nederland

geboren te Rotterdam, Nederland

Dit proefschrift is goedgekeurd door de promotoren.

Samenstelling promotiecommissie:

Rector Magnificus	voorzitter
Prof. dr. L. Kuipers	Technische Universiteit Delft, promotor
Dr. S. Conesa-Boj	Technische Universiteit Delft, promotor

Onafhankelijke leden:

Prof. dr. Y. M. Blanter	Technische Universiteit Delft
Prof. dr. F. Peiró Martínez	Universitat de Barcelona, Spain
Dr. T. van der Sar	Technische Universiteit Delft
Dr. S. Bhattacharyya	Universiteit Leiden
Prof. dr. G. A. Steele	Technische Universiteit Delft, reservelid

Overige leden:

Dr. M. Tinoco Rivas	Universidad Complutense de Madrid, Spain

Keywords: Transition metal dichalcogenides nanostructures, chemical vapor deposition, transmission electron microscopy, electron energy-loss spectroscopy, four-dimensional scanning transmission electron microscopy, electron microscope pixel array detector

Printed by: Gildeprint

Front & Back: Artistic impression of the crystal structure of WS_2 with (*back*) areas of (*top*) polytypism and (*bottom*) strain and twist.

Copyright © 2024 by S. E. van Heijst

ISBN (printed version) 978-94-6384-557-1

ISBN (electronic version) 978-94-6384-558-8

An electronic version of this dissertation is available at
`http://repository.tudelft.nl/`.

We keep moving forward, opening new doors, and doing new things
because we're curious and curiosity keeps leading us down new paths.

- Walt Disney

CONTENTS

Summary **ix**

Samenvatting **xi**

1 Introduction **1**
References 5

2 Fabrication of WS_2 Nanostructures via Chemical Vapor Deposition **11**
2.1 Introduction 12
2.2 Chemical Vapor Deposition 13
2.3 Optimization of the Chemical Vapor Deposition Process for the Synthesis of 2D WS_2 Flake 14
2.3.1 Choice in Substrate Materials 14
2.3.2 Properties of the Precursors 15
2.3.3 CVD Growth Conditions 17
2.3.4 Addition of Catalysts 20
2.4 Morphology Control in Chemical Vapor Deposition Processes 21
2.5 Chemical Vapor Deposition Furnace and Procedure for the Fabrication of WS_2 Nanostructures 23
References 25

3 Transmission Electron Microscopy Techniques: The Characterization of WS_2 Nanostructures **31**
3.1 Introduction 32
3.2 Analysis of EELS Spectral Images: EELSFITTER 34
3.2.1 Preprocessing Methods: Clustering and Noise Reduction 34
3.2.2 The Neural Network and Monte Carlo Replica Method 35
3.2.3 Bandgap Determination from the EELS Low-Loss Region 36
3.2.4 Local Thickness Determination from EEL spectra 37
3.2.5 Naturally Twisted WS_2 Flakes: A Case Study 37
3.3 Mapping Strain Distributions with 4D STEM-EMPAD: STRAINMAPPER 40
3.3.1 The Exit-Wave Power Cepstrum Approach 41
3.3.2 Peak Tracking and Clustering 41
3.3.3 Calculation of Strain Fields and Deformation Angles 42
3.3.4 Twisted $MoSe_2/WSe_2$ Heterostructures: A Case Study 44
References 49

4 Illuminating the Electronic Properties of WS_2 Polytypism with Electron Microscopy **55**
4.1 Introduction 56

4.2 Fabrication of WS_2 Nanoflowers 56
4.3 Mixed 2H/3R Polytypism in WS_2 Nanoflowers 58
4.4 Fingerprinting Electronic Excitations with Spatially-Resolved EELS 59
4.5 Bandgap Determination of Polytypic 2H/3R WS_2 using Machine Learning . 63
4.6 Conclusion 64
References 65

5 Heterostrain-Driven Bandgap Increase in Twisted WS_2: A Nanoscale Study 69
5.1 Introduction 70
5.2 Spatially-Resolved Bandgap and Thickness Correlation Analysis of Twisted WS_2 71
5.3 Mapping Strain Distributions in Twisted WS_2 with 4D STEM-EMPAD 74
  5.3.1 WS_2 Stacked Flakes 74
  5.3.2 Twisted WS_2 Flake 77
5.4 Correlation between Bandgap Energy and Strain Distribution in Twisted WS_2 Flake 79
5.5 Conclusion 80
References 80

6 Conclusion and Outlook 85
References 89

A Supplementary Materials to Chapter 4 93
A.1 Stacking Sequences in TMD Materials 94
A.2 Crystalline Structure of the WS_2 Nanoflowers 95

B Supplementary Materials to Chapter 5 97
B.1 Data Processing of EELS Spectral Images 98
  B.1.1 Bandgap Energy Uncertainty Estimation in Twisted WS_2. 98
  B.1.2 Local Thickness Mapping of Twisted WS_2 100
B.2 Mapping Strain Distributions in Twisted WS_2 with 4D STEM-EMPAD. . . . 101
  B.2.1 Additional Spatially-Resolved Strain Maps of a Twisted WS_2 Flake . . 101
  B.2.2 Application of Gaussian Filter to Spatially-Resolved Strain and Deformation Angle Maps 102
B.3 HAADF-STEM Analysis of Twisted WS_2: Revealing Atomic-Scale Structure . 105

C Transmission Electron Microscopy Acquisition Details 107
C.1 Acquisition Details of Chapter 3. 108
C.2 Acquisition Details of Chapter 4 and Appendix A 108
C.3 Acquisition Details of Chapter 5 and Appendix B 109

Curriculum Vitæ 111

List of Publications 113

Acknowledgements 115

SUMMARY

Two-dimensional (2D) layered materials have attracted the interest of the scientific community following the discovery of graphene and its extraordinary properties. Of particular interest is a class of materials called transition metal dichalcogenides (TMDs). The materials within this class were discovered to show similarly intriguing optical and electronic properties, when compared to graphene. Moreover, research indicated that these properties are also highly sensitive to the TMDs' underlying atomic structure. Gaining control over these structural properties would enable the tuning of the physical and chemical properties, and hence allow for the fabrication of novel TMD nanostructures with tailored functionalities. Driven by this potential, we strive to gain a comprehensive understanding of the relationship between the structural, chemical, and local electronic properties of nanostructures based on one such TMD material: tungsten disulfide (WS_2). This in order to aid us in the exploitation of the tunability of these physical properties through the fabrication of novel WS_2 nanostructures.

The first step in realizing this, necessitates a controlled fabrication method by which to synthesize the novel WS_2 nanostructures. To this end, various techniques have been proposed in literature. In the context of this thesis, the fabrication of the novel WS_2 nanostructures is achieved by use of chemical vapor deposition (CVD). This versatile technique has been reported as the preferred method in the fabrication of TMD materials as it simultaneously allows for the production of high-quality TMD materials, offers precise control over nanostructure dimensions and morphology, and has the potential for high scalability. Chapter 2 serves to provide an in-depth understanding of the CVD technique and its controllability in the context of 2D WS_2 nanostructures. Gaining this understanding makes possible the controlled fabrication of numerous intriguing TMD nanostructures, such as those presented in Chapters 4 and 5.

Following the fabrication of the novel WS_2 nanostructures, proper characterization of their properties is essential to achieve our aforementioned goals. A powerful tool for this purpose is transmission electron microscopy (TEM). This technique enables simultaneous inspection of structural, chemical and physical properties of TMD nanostructures with unprecedented spatial and spectral resolution, covering spatial ranges from the atomic scale up to the micrometer level and beyond. The various TEM-based techniques play a pivotal role in achieving this. For instance, scanning transmission electron microscopy (STEM) allows for structural characterization and electron energy-loss spectroscopy (EELS) can be utilized to study the local electronic properties of nanomaterials. Furthermore, the use of four-dimensional (4D) STEM coupled with an electron microscope pixel array detector (EMPAD) allows for the extraction of a wealth of additional information, such as details about variations in strain fields across specimens.

A comprehensive data analysis is required in order to fully exploit the potential of the aforementioned TEM-based techniques of EELS and 4D STEM-EMPAD. Therefore, two analysis frameworks have been developed to aid in the interpretation of their respective datasets. First, the framework developed for the analysis of EELS spectral images, called EELSFITTER, exploits machine learning to reveal interesting phenomenon within EEL spectra across specimens. Second, the analysis framework called STRAINMAPPER allows the extraction of strain from 4D STEM-EMPAD datasets by building upon the existing exit-wave power cepstrum (EWPC) approach. Chapter 3 provides an overview of the methodology behind these analysis frameworks and demonstrates their full functionality through case studies. By combining the strength of the TEM-based techniques and their respective analysis framework, complete and extensive studies of the properties of the fabricated WS_2 nanostructures can be achieved. This is demonstrated in Chapters 4 and 5.

Chapter 4 is devoted to the study of free-standing WS_2 flower-like nanostructures. These nanostructures were grown by means of CVD directly on a TEM microchip, negating the need for sample transfer for their subsequent characterization by state-of-the-art TEM. Through the use of STEM, the WS_2 nanoflowers were discovered to exhibit a 2H/3R polytypism. While TMD nanostructures with either the 2H or 3R crystalline phases have been routinely studied, our understanding of TMD nanomaterials with mixed 2H/3R polytypes remains limited. Due to their rich variety of shape-morphology configurations, the WS_2 nanoflowers make the ideal laboratory for studying the modifications in the local electronic properties of WS_2 based on this mixed polytypism. We utilized spatially-resolved EELS to fingerprint the edge, surface and bulk plasmonic excitations of the polytypic nanoflowers, and traced back their origin to specific structural characteristics. Moreover, the EELSFITTER analysis framework was used to probe their bandgap. This analysis revealed an indirect bandgap of $E_{\mathrm{BG}} = 1.6^{+0.3}_{-0.2}$ eV consistent with first-principle density functional theory (DFT) calculations carried out on 2H/3R WS_2 bulk.

In Chapter 5 instead we delve into the characterization of naturally twisted WS_2 specimens. These twisted nanostructures were similarly grown directly on a TEM microchip, with only a small modification to the nanoflower CVD process. Their twisted nature makes these nanostructures a likely candidate for the presence of strain. Hence, making them interesting for the investigation of the interplay between structural properties, local electronic properties and strain fields. More specifically we studied the interplay between specimen thickness, bandgap and strain fields. Our approach integrates EELS enhanced by the functionalities of EELSFITTER and 4D STEM-EMPAD analysis via STRAINMAPPER. Through this synergistic methodology, we unveil enhancements up to 20% in the bandgap energy with respect to the specimen thickness. This phenomenon is traced back to sizable deformation angles present within individual layers, which can be directly linked to distinct variations in local heterostrain fields.

The work presented in this thesis, especially in Chapters 4 and 5, provides insights into the understanding of the interplay between structural and physical properties in intricate CVD-grown WS_2 nanostructures obtained via characterization with complementary TEM-based techniques. With this we lay the foundational work in the quest to design novel TMD nanostructures with tailored functionalities.

SAMENVATTING

Sinds de ontdekking van grafeen en diens buitengewone eigenschappen hebben tweedimensionale (2D) gelaagde materialen veel aandacht getrokken binnen de wetenschappelijke gemeenschap. Een bijzonder interessante groep binnen deze materialen zijn de transitiemetaal dichalcogeniden (TMDs). Materialen in deze groep vertonen vergelijkbare fascinerende optische en elektronische eigenschappen als grafeen. Bovendien wees onderzoek uit dat deze eigenschappen gevoelig zijn voor de onderliggende atomaire structuur van de TMDs. Dit biedt de mogelijkheid om de chemische en fysische eigenschappen aan te passen via de structurele eigenschappen van het materiaal. Het fabriceren van unieke TMD nanostructuren met specifieke functionaliteiten komt hiermee een stap dichterbij. Gedreven door dit vooruitzicht streven we onze kennis te verbreden met betrekking tot de relatie tussen de structurele, chemische en lokaal elektronische eigenschappen van nanostructuren gebaseerd op zo'n TMD materiaal: wolfraamdisulfide (WS_2). Deze opgedane kennis zal ons helpen in het onderzoek naar het aanpassen van de fysische eigenschappen via de fabricage van unieke WS_2 nanostructuren.

De eerste stap hierin is het vinden van een gecontroleerde fabricagemethode voor de creatie van de unieke WS_2 nanostructuren. Uit de literatuur blijkt dat hiervoor vele methodes bestaan. In dit proefschrift gebruiken we een techniek genaamd chemische dampdepositie (CVD) voor de productie van unieke WS_2 nanostructuren. Deze veelzijdige techniek produceert TMDs van hoge kwaliteit, biedt goede controle over de afmetingen en morfologie van nanostructuren, en heeft de potentie tot opschaling. Dit maakt dat deze techniek de favoriet is voor de productie van TMD nanostructuren. Hoofdstuk 2 geeft een overzicht van de CVD techniek waarin diens veelzijdigheid op het gebied van gecontroleerde fabricage wordt belicht. Hierbij leggen we de focus op 2D WS_2 nanostructuren. Het implementeren van deze kennis maakt het mogelijk om verscheidene TMD nanostructuren te fabriceren, waaronder die gepresenteerd in Hoofdstuk 4 en 5.

De tweede stap, na de fabricage van de WS_2 nanostructuren, is het karakteriseren van hun eigenschappen. Een uitermate geschikte techniek hiervoor is transmissie-elektronenmicroscopie (TEM). Deze techniek maakt gelijktijdige inspectie van structurele, chemische en fysische eigenschappen van TMD nanostructuren mogelijk met een ongekende ruimtelijke en spectrale resolutie. De verschillende TEM-gebaseerde technieken spelen hierbij een vitale rol. Zo wordt de techniek scanning transmissie-elektronenmicroscopie (STEM) gebruikt voor de inspectie van het structurele karakter van nanomaterialen, terwijl elektronen-energieverlies-spectroscopie (EELS) wordt ingezet voor de analyse van hun lokaal elektronische eigenschappen. Verder kan een schat aan aanvullende informatie worden onthuld door het gebruik van vierdimensionale (4D) STEM in combinatie met een elektronenmicroscoop pixel-array detector (EMPAD), waaronder ook details over lokale variaties in spanningsvelden.

Om de potentie van de TEM-gebaseerde technieken EELS en 4D STEM-EMPAD volledig te benutten, is een uitgebreide data-analyse vereist. Hiervoor zijn twee data-analyse tools ontwikkeld die elk helpen bij de interpretatie van een van de bijbehorende datasets. De eerste data-analyse tool, EELSFITTER, is ontwikkeld voor het verwerken van datasets verkregen uit EELS metingen. Hierbij wordt machine learning gebruikt om interessante details in de EEL spectra aan het licht te brengen. De andere data-analyse tool, genaamd STRAINMAPPER, bouwt voort op de bestaande exit-wave power cepstrum (EWPC) methode voor het verkrijgen van informatie over spanningsvelden vanuit 4D STEM-EMPAD datasets. In Hoofdstuk 3 worden de methodes achter beide data-analyse tools uitvoerig besproken. Verder wordt hun volledige functionaliteit gedemonstreerd aan de hand van een voorbeeld. Door de kracht van de TEM-gebaseerde technieken te combineren met hun bijbehorende data-analyse tools, kan er volledig en uitgebreid onderzoek gedaan worden naar de eigenschappen van de gecreëerde WS_2 nanostructuren. Dit wordt gedemonstreerd in Hoofdstuk 4 en 5.

In Hoofdstuk 4 richten we ons op de studie van vrijstaande WS_2 nanostructuren met een bloemachtige formatie. Deze nanostructuren werden geproduceerd met behulp van CVD, direct op een TEM grid. Dit maakt het mogelijk om de nanostructuren direct te bestuderen met behulp van TEM. De kristalstructuur van de nanostructuren werd geïnspecteerd middels STEM, waaruit bleek dat deze een 2H/3R fase volgde. De kristalfases 2H en 3R zijn uitvoerig bestudeerd in de literatuur, maar er is weinig bekend over deze gemengde 2H/3R polytype. De variatie in oriëntatie en vorm van de bloemachtige WS_2 nanostructuren maakt ze een ideaal platform voor het bestuderen van deze gemengde kristalfase en diens effect op de lokaal elektronische eigenschappen. Hiervoor maakten we gebruik van EELS om de rand, oppervlak en bulk plasmon-excitaties in kaart te brengen. Hierna konden we deze excitaties toekennen aan specifieke structurele elementen. Verder werd EELSFITTER ingezet voor het analyseren van de bandgap van de nanostructuren. Deze bandgap bleek indirect met een waarde van $E_{\mathrm{BG}} = 1.6^{+0.3}_{-0.2}$ eV. Dit resultaat is in overeenstemming met berekeningen verricht op bulk 2H/3R WS_2 middels dichtheidsfunctionaaltheorie (DFT).

In Hoofdstuk 5 bespreken we het onderzoek aan WS_2 nanostructuren waarin de lagen onderling gedraaid zijn. Deze nanostructuren werden geproduceerd op vergelijkbare wijze als de bloemachtige nanostructuren, met enkel minimale aanpassingen aan het CVD proces. Door de gedraaide lagen in deze nanostructuren is er een reële kans op spanningsvelden binnen deze nanostructuren. Dit maakt ze ideale kandidaten voor het onderzoek naar het verband tussen structurele eigenschappen, lokaal elektronische eigenschappen en spanningsvelden. Hierin leggen wij de focus op het verband tussen de dikte van de nanostructuren, hun bandgap, en de aanwezigheid van spanningsvelden. De hiervoor gebruikte methode combineert EELS en 4D STEM-EMPAD met hun respectievelijke date-analyse tools EELSFITTER en STRAINMAPPER. Dit onderzoek leidt tot de ontdekking dat de bandgap een stijgende lijn volgt als functie van de dikte, met een stijging tot wel 20% in de waarde van de bandgap. Dit fenomeen bleek het gevolg van vervormingen in de individuele lagen van de nanostructuren, welke gepaard gingen met de aanwezigheid van beduidende fluctuaties in de lokale spanningsvelden.

Het werk gepresenteerd in dit proefschrift, met name in Hoofdstuk 4 en 5, biedt inzicht in de interactie tussen structurele en fysische eigenschappen in complexe WS_2 nanostructuren middels de inzet van complementaire TEM-gebaseerde technieken. Hiermee zetten we de eerste stap voor toekomstig onderzoek naar de creatie van unieke TMD nanostructuren met specifieke functionaliteiten.

1

INTRODUCTION

TWO-DIMENSIONAL LAYERED MATERIALS

IN recent years, interest in two-dimensional (2D) layered materials has surged, driven by their potential to exhibit exotic quantum mechanical effects on a macroscopic scale. These materials hold great potential for a wide range of applications, including magnetic resonance imaging (MRI), magnetic field sensors, high-density storage devices, water filtration, and quantum computing. Some of these applications have already been realized, while others are still in the early stages of development [1–6]. The wide range of applications underscores the broad spectrum of this group of materials.

One notable example of a 2D layered material is graphene. Upon its discovery, graphene, a single layer of carbon atoms, was recognized for its extraordinary properties [7–9]. However, graphene had a limitation: it lacked a crucial feature, a bandgap, which restricted its use in nanoelectronic devices. As a result of this limitation, the scientific community embarked on a quest to explore alternative 2D materials capable of forming atomic sheets with extraordinary properties, with a particular emphasis on those exhibiting semiconducting behavior [10].

This search led to the discovery of numerous 2D layered materials, including those with a bandgap. These materials exhibited a wide range of bandgaps, covering the spectrum from the visible to infrared, with the choice of material [10]. One class of materials that emerged as particularly interesting is transition metal dichalcogenides (TMDs). Each layer of these TMD materials comprises of a layer of transition metal atoms sandwiched between two layers of chalcogen atoms. Examples of materials in this class include tungsten disulfide (WS_2), molybdenum disulfide (MoS_2), and their selenide, and telluride counterparts.

Similarly intriguing optical and electronic properties, when compared to graphene, were discovered for this class of materials. Moreover, research indicated that these properties are also highly sensitive to the TMDs' underlying atomic structure. Hence, understanding the intricate relationship between structural and physical properties could enable the tuning of these properties for specific applications.

PROPERTY TUNABILITY IN TRANSITION METAL DICHALCOGENIDES

An example of the close relation between the structure and properties of TMD materials becomes apparent when reducing their dimensionality. In their bulk form, TMD crystals consist of various stacked layers, with each layer being composed as previously described. While within these layers, atoms are strongly bonded through covalent bonds, the layers themselves are held together by weak van der Waals forces. Due to the nature of these forces, it is possible to separate the TMDs, effectively decomposing the bulk crystal into individual monolayers [11]. Such a reduction in dimensionality typically leads to changes in the material's optical and electronic properties. As an example, WS_2 undergoes an indirect-to-direct bandgap transition and experiences a change in bandgap value when reduced from bulk to a monolayer [10]. Additionally, an enhancement in the strength of the photoluminescence is observed simultaneously [10].

In addition to dimensionality reduction, the arrangement of individual layers within TMD crystals offers another way to tune their properties. These arrangements, known as polytypes, are characterized by various stacking sequences. Each polytype is identified by a specific designation: a number, which corresponds to the number of layers in the unit cell (the smallest repeating unit of the crystal), and a letter, which indicates the type of symmetry observed in that arrangement.

Taking WS_2 as an example, the polytypes 2H and 3R are the most commonly observed due to their stability [12–15]. The symmetries possessed by 2H- and 3R-WS_2 are hexagonal and rhombohedral, respectively. Both these polytypes are semiconducting in nature, and exhibit similar optical and electronic properties [12, 16]. The notable distinction is the broken inversion symmetry in the 3R polytype, which makes it particularly interesting for applications in nonlinear optics, and valley- and spintronics [17–19]. Furthermore, these polytypes can exhibit differences in their chemical properties. For example, variations have been observed in their catalytic performance towards the hydrogen evolution reaction (HER) [20].

Another polytype of WS_2 is the metastable 1T polytype. Unlike the 2H and 3R polytypes, where the sulfur atomic layers within each monolayer are aligned, the 1T polytype features a displacement of one sulfur atomic layer transversally. This results in a trigonal symmetry. This difference in crystal symmetry is believed to have a substantial impact on the electronic properties, potentially leading to a transition from a semiconducting to a metallic nature [21, 22].

In addition to variations between polytypes, the occurrence of multiple polytypes within the same structure, a phenomenon known as polytypism, has also been observed in TMDs [23–25]. This provides yet another avenue for tuning the properties of these materials. An example of this was revealed by Wang *et al.* [23], as they discovered that a mixed 1T/2H polytypism in MoS_2 yields an enhancement in the photoelectrocatalytic properties. This enhancement was attributed not to the presence of the separate polytypes but instead to the synergistic effect of the 1T/2H phase.

In contrast to the perfectly aligned layers of the previously discussed polytypes, TMD homostructures can also feature twisted layers. The interest in these twisted structure have surged, particularly following the discovery of superconductivity and ferromagnetism in magic angle-rotated bilayer graphene [26, 27]. Extensive studies of twisted TMD structures have shown that the bandgap can be tuned based on the twist angle due to variations in interlayer coupling [28–31]. More specifically, it was observed that variations in the twist angles could result in bandgap energy changes of a few hundreds of nanometers, with non-twisted specimen exhibiting the lowest bandgap energy values. Moreover, twisted TMD structures have been found to exhibit improved electron mobility [29]. Recently even evidence of superconductivity has been reported in twisted bilayer tungsten diselenide (WSe_2) [32, 33].

A possible consequence of introducing twist in multilayer TMD structures is the development of strain. This strain may arise due to lattice mismatches between layers, or between TMD crystals and the substrate, as well as from mechanical bending of the crystals. The presence of strain can lead to local changes in the crystal structure, which in turn impacts the physical properties of these materials. For instance, the electronic band structure of these materials is known to undergo various modifications due to strain.

These variations can include alterations in bandgap values and shifts between indirect and direct bandgaps [30, 34–42]. Additionally, it has been theoretically predicted that strain can also induce a transition from semiconductor to metallic behavior [37, 38].

An example of this tuning of the electronic properties was demonstrated by Conley *et al.* [36]. They reported on the effects of uniaxial tensile strain, applied by controlled bending, on MoS_2 mono- and bilayers. Photoluminescence (PL) spectroscopy revealed both structures to follow an approximate linear decrease with applied strain at different rates: $\approx$ 45 meV/% strain for the monolayer, and $\approx$ 120 meV/% strain for the bilayer. Upon applying strain of $\approx$ 1% the monolayer MoS_2 was found to exhibit an indirect bandgap, instead of the conventional direct bandgap.

The impact of strain extends beyond just alterations in the electronic band structure. Notably, strain can lead to changes in the optical [35, 36, 41, 43, 44] and magnetic [39, 42, 45] properties. Moreover, strain can also induce enhancements in electron mobility [40] and result in the confinement of excitons [35, 46], further showcasing its significant influence on the physical properties of these materials.

It is important to emphasize that the strain effects can vary greatly in literature, as it is sensitive to the structural properties of the specimen investigated. This was already briefly mentioned in the above-provided example. Hence, highlighting the importance to study strain effects not just of the physical properties of the specimen but also its structural properties.

In summary, the opportunities for tuning the physical and chemical properties of TMD materials through their underlying atomic structure are plentiful. Gaining control over these structural properties would enable the fabrication of novel TMD nanostructures with tailored functionalities. This could lead to the use of TMD materials as building blocks for next-generation nanodevices, making it highly desirable in the quest to design novel nanostructures with tailored functionalities. With this motivation in mind we continue with the specific aim of this thesis.

THESIS SCOPE AND OUTLINE

The aim of this doctoral thesis is twofold. Firstly, we strive to gain a comprehensive understanding of the relationship between the structural, chemical, and local electronic properties of WS_2 nanostructures. Secondly, we aim to exploit the tunability of these physical properties through the fabrication of novel WS_2 nanostructures. Realizing this goal requires two key ingredients: *1)* a method for synthesizing novel WS_2 nanostructures, and *2)* a technique that allows the characterization of the structural, chemical, and local electronic properties simultaneously and on the single-atom scale.

In this thesis, we explore chemical vapor deposition (CVD) as method for the fabrication of novel WS_2 nanostructures. This versatile technique has been reported to offer good controllability in producing TMD nanostructures. **Chapter 2** will delve into this technique and its controllability.

Chapter 3 focuses on the chosen characterization technique for our fabricated structures: transmission electron microscopy (TEM). TEM is arguably the most efficient and versatile tool for characterizing novel materials over spatial ranges from the atomic scale up to the micrometer level and beyond [47]. This is mainly due to advancements made in both spatial and energy resolution.

Within TEM, the electron energy-loss spectroscopy (EELS) technique allows us to probe the local electronic properties of the examined nanostructures. To fully exploit this technique for characterization, theoretical modeling becomes essential. To address this need, we have developed EELSFITTER, an analysis framework based on machine learning, which is further discussed in **Chapter 3**.

Another featured technique in **Chapter 3** is four-dimensional (4D) scanning transmission electron microscopy (STEM). This method has shown great promise in the mapping of strain in 2D van der Waals materials like TMDs, especially when coupled with an electron microscopy pixel array detector (EMPAD). The analysis of the 4D STEM-EMPAD datasets requires the development of a second analysis framework, called STRAINMAPPER. The functionalities of this framework are also explained in **Chapter 3**.

Finally, **Chapter 4** and **Chapter 5** demonstrate the fabrication and characterization of two different WS_2 nanostructures.

Chapter 4 reports on the characterization of flower-like WS_2 nanostructures that exhibit a 2H/3R polytypism. The nature of their edge, surface, and bulk plasmonic excitations is traced back to specific structural characteristics through spatially-resolved EELS. Furthermore, the bandgap of these polytypic nanoflowers is probed using the EELSFITTER analysis framework, revealing an indirect bandgap consistent with first-principle density functional theory (DFT) calculations carried out on 2H/3R WS_2 bulk.

Moving on to **Chapter 5**, we delve into the characterization of naturally twisted WS_2 specimens. Due to their twisted nature, these structure are suspected to be subject to strain. We thoroughly investigate the interplay between the structure, specifically the thickness, bandgap, and strain fields. To achieve this, we utilize a synergistic methodology that combines EELS enhanced by the functionalities of EELSFITTER and 4D STEM-EMPAD analysis via STRAINMAPPER. The findings reveal a pronounced increase in the bandgap energy as a function of the local thickness, accompanied by noticeable fluctuations in the local strain fields.

Concluding this thesis, (**Chapter 6**) provides insights into the future prospects of researching novel TMD nanostructures, including those explored in this work.

REFERENCES

[1] M.-K. Tsang, Y.-T. Wong, and J. Hao, *Cutting-Edge Nanomaterials for Advanced Multimodal Bioimaging Applications,* Small Methods **2**, 1700265 (2018).

[2] N. Žurauskienė, *Engineering of Advanced Materials for High Magnetic Field Sensing: A Review,* Sensors **23**, 2939 (2023).

[3] H. Li, L. Tao, and J.-B. Xu, *Intrinsic memristive mechanisms in 2D layered materials for high-performance memory,* Journal of Applied Physics **129**, 050902 (2021).

[4] P. Kumar, H. Abuhimd, W. Wahyudi, M. Li, J. Ming, and L.-J. Li, *Review — Two-Dimensional Layered Materials for Energy Storage Applications,* ECS Journal of Solid State Science and Technology **5**, Q3021 (2016).

[5] S. Dervin, D. D. Dionysiou, and S. C. Pillai, *2D nanostructures for water purification: graphene and beyond,* Nanoscale **8**, 15115 (2016).

[6] X. Liu and M. C. Hersam, *2D materials for quantum information science,* Nature Reviews Materials **4**, 669 (2019).

[7] K. S. Novoselov, A. K. Geim, S. V. Morozov, D. Jiang, Y. Zhang, S. V. Dubonos, I. V. Grigorieva, and A. A. Firsov, *Electric Field Effect in Atomically Thin Carbon Films,* Science **306**, 666 (2004).

[8] V. Singh, D. Joung, L. Zhai, S. Das, S. I. Khondaker, and S. Seal, *Graphene based materials: Past, present and future,* Progress in Materials Science **56**, 1178 (2011).

[9] F. Bonaccorso, Z. Sun, T. Hasan, and A. C. Ferrari, *Graphene photonics and optoelectronics,* Nature Photonics **4**, 611 (2010).

[10] W. Choi, N. Choudhary, G. H. Han, J. Park, D. Akinwande, and Y. H. Lee, *Recent development of two-dimensional transition metal dichalcogenides and their applications,* Materials Today **20**, 116 (2017).

[11] C. M. Orofeo, S. Suzuki, Y. Sekine, and H. Hibino, *Scalable synthesis of layer-controlled WS_2 and MoS_2 sheets by sulfurization of thin metal films,* Applied Physics Letters **105**, 083112 (2014).

[12] I. Song, C. Park, and H. C. Choi, *Synthesis and properties of molybdenum disulphide: from bulk to atomic layers,* RSC Advances **5**, 7495 (2015).

[13] J. A. Wilson and A. D. Yoffe, *The transition metal dichalcogenides discussion and interpretation of the observed optical, electrical and structural properties,* Advances in Physics **18**, 193 (1969).

[14] J. He, K. Hummer, and C. Franchini, *Stacking effects on the electronic and optical properties of bilayer transition metal dichalcogenides MoS_2, $MoSe_2$, WS_2, and WS_2,* Physical Review B **89**, 075409 (2014).

[15] R. Suzuki, M. Sakano, Y. J. Zhang, R. Akashi, D. Morikawa, A. Harasawa, K. Yaji, K. Kuroda, K. Miyamoto, T. Okuda, K. Ishizaka, R. Arita, and Y. Iwasa, *Valley-dependent spin polarization in bulk MoS_2 with broken inversion symmetry,* Nature Nanotechnology **9**, 611 (2014).

[16] R. Yang, S. Feng, X. Lei, X. Mao, A. Nie, B. Wang, K. Luo, J. Xiang, F. Wen, C. Mu, Z. Zhao, B. Xu, H. Zeng, Y. Tian, and Z. Liu, *Effect of layer and stacking sequence in simultaneously grown 2H and 3R WS_2 atomic layers,* Nanotechnology **30**, 345203 (2019).

[17] J. Shi, P. Yu, F. Liu, P. He, R. Wang, L. Qin, J. Zhou, X. Li, J. Zhou, X. Sui, S. Zhang, Y. Zhang, Q. Zhang, T. C. Sum, X. Qiu, Z. Liu, and X. Liu, *3R MoS_2 with Broken Inversion Symmetry: a Promising Ultrathin Nonlinear Optical Device,* Advanced Materials **29**, 1701486 (2017).

[18] Z. Zeng, X. Sun, D. Zhang, W. Zheng, X. Fan, M. He, T. Xu, L. Sun, X. Wang, and A. Pan, *Controlled Vapor Growth and Nonlinear Optical Applications of Large-Area 3R Phase WS_2 and WSe_2 Atomic Layers,* Advanced Functional Materials **29**, 1806874 (2019).

[19] R. Akashi, M. Ochi, S. Bordács, R. Suzuki, Y. Tokura, Y. Iwasa, and R. Arita, *Two-Dimensional Valley Electrons and Excitons in Noncentrosymmetric 3R-MoS_2,* Physical Review Applied **4**, 014002 (2015).

[20] R. J. Toh, Z. Sofer, J. Luxa, D. Sedmidubský, and M. Pumera, *3R phase of MoS_2 and WS_2 outperforms the corresponding 2H phase for hydrogen evolution,* Chemical Communications **53**, 3054 (2017).

[21] F. Wypych and R. Schöllhorn, *1T-MoS_2, a new metallic modification of molybdenum disulfide,* Journal of the Chemical Society, Chemical Communications , 1386 (1992).

[22] R. Pan, X.-L. Fan, H. Zhang, and Y. Yang, *First-principles investigation on the interface of transition metal dichalcogenide MX_2 (M=Mo, W; X=S, Se) monolayer on Al_2O_3(0001),* Computational Materials Science **122**, 118 (2016).

[23] D. Wang, B. Su, Y. Jiang, L. Li, B. K. Ng, Z. Wu, and F. Liu, *Polytype 1T/2H MoS_2 heterostructures for efficient photoelectrocatalytic hydrogen evolution,* Chemical Engineering Journal **330**, 102 (2017).

[24] A. Yan, W. Chen, C. Ophus, J. Ciston, Y. Lin, K. Persson, and A. Zettl, *Identifying different stacking sequences in few-layer CVD-grown MoS_2 by low-energy atomic-resolution scanning transmission electron microscopy,* Physical Review B **93**, 041420 (2016).

[25] J.-U. Lee, K. Kim, S. Han, G. H. Ryu, Z. Lee, and H. Cheong, *Raman Signatures of Polytypism in Molybdenum Disulfide,* ACS Nano **10**, 1948 (2016).

[26] Y. Cao, V. Fatemi, S. Fang, K. Watanabe, T. Taniguchi, E. Kaxiras, and P. Jarillo-Herrero, *Unconventional superconductivity in magic-angle graphene superlattices,* Nature **556**, 43 (2018).

[27] M. Yankowitz, S. Chen, H. Polshyn, Y. Zhang, K. Watanabe, T. Taniguchi, D. Graf, A. F. Young, and C. R. Dean, *Tuning superconductivity in twisted bilayer graphene,* Science **363**, 1059 (2019).

[28] S. Zheng, L. Sun, X. Zhou, F. Liu, Z. Liu, Z. Shen, and H. J. Fan, *Coupling and Interlayer Exciton in Twist-Stacked WS_2 Bilayers,* Advanced Optical Materials **3**, 1600 (2015).

[29] M. Liao, Z. Wei, L. Du, Q. Wang, J. Tang, H. Yu, F. Wu, J. Zhao, X. Xu, B. Han, K. Liu, P. Gao, T. Polcar, Z. Sun, D. Shi, R. Yang, and G. Zhang, *Precise control of the interlayer twist angle in large scale* MoS_2 *homostructures,* Nature Communications **11**, 2153 (2020).

[30] Z. Wang, Q. Chen, and J. Wang, *Electronic Structure of Twisted Bilayers of Graphene/*MoS_2 *and* MoS_2/MoS_2*,* The Journal of Physical Chemistry C **119**, 4752 (2015).

[31] K. Liu, L. Zhang, T. Cao, C. Jin, D. Qiu, Q. Zhou, A. Zettl, P. Yang, S. G. Louie, and F. Wang, *Evolution of interlayer coupling in twisted molybdenum disulfide bilayers,* Nature Communications **5**, 4966 (2014).

[32] L. Wang, E.-M. Shih, A. Ghiotto, L. Xian, D. A. Rhodes, C. Tan, M. Claassen, D. M. Kennes, Y. Bai, B. Kim, K. Watanabe, T. Taniguchi, X. Zhu, J. Hone, A. Rubio, A. N. Pasupathy, and C. R. Dean, *Correlated electronic phases in twisted bilayer transition metal dichalcogenides,* Nature Materials **19**, 861 (2020).

[33] M. Bélanger, J. Fournier, and D. Sénéchal, *Superconductivity in the twisted bilayer transition metal dichalcogenide* WSe_2*: A quantum cluster study,* Physical Review B **106**, 235135 (2022).

[34] Y. Li, T. Wang, M. Wu, T. Cao, Y. Chen, R. Sankar, R. K. Ulaganathan, F. Chou, C. Wetzel, C.-Y. Xu, S. G. Louie, and S.-F. Shi, *Ultrasensitive tunability of the direct bandgap of 2D InSe flakes via strain engineering,* 2D Materials **5**, 021002 (2018).

[35] A. Castellanos-Gomez, R. Roldán, E. Cappelluti, M. Buscema, F. Guinea, H. S. J. van der Zant, and G. A. Steele, *Local Strain Engineering in Atomically Thin* MoS_2*,* Nano Letters **13**, 5361 (2013).

[36] H. J. Conley, B. Wang, J. I. Ziegler, R. F. Haglund, S. T. Pantelides, and K. I. Bolotin, *Bandgap Engineering of Strained Monolayer and Bilayer* MoS_2*,* Nano Letters **13**, 3626 (2013).

[37] W. S. Yun, S. W. Han, S. C. Hong, I. G. Kim, and J. D. Lee, *Thickness and strain effects on electronic structures of transition metal dichalcogenides: 2H-*MX_2 *semiconductors (*$M = Mo, W; X = S, Se, Te$*),* Physical Review B **85**, 033305 (2012).

[38] P. Johari and V. B. Shenoy, *Tuning the Electronic Properties of Semiconducting Transition Metal Dichalcogenides by Applying Mechanical Strains,* ACS Nano **6**, 5449 (2012).

[39] P. Lu, X. Wu, W. Guo, and X. C. Zeng, *Strain-dependent electronic and magnetic properties of* MoS_2 *monolayer, bilayer, nanoribbons and nanotubes,* Physical Chemistry Chemical Physics **14**, 13035 (2012).

[40] H. Shi, H. Pan, Y. W. Zhang, and B. I. Yakobson, *Quasiparticle band structures and optical properties of strained monolayer* MoS_2 *and* WS_2*,* Physical Review B **87**, 155304 (2013).

[41] C. R. Zhu, G. Wang, B. L. Liu, X. Marie, X. F. Qiao, X. Zhang, X. X. Wu, H. Fan, P. H. Tan, T. Amand, and B. Urbaszek, *Strain tuning of optical emission energy and polarization in monolayer and bilayer* MoS_2, Physical Review B **88**, 121301 (2013).

[42] H. Pan and Y.-W. Zhang, *Tuning the Electronic and Magnetic Properties of* MoS_2 *Nanoribbons by Strain Engineering,* The Journal of Physical Chemistry C **116**, 11752 (2012).

[43] Y. Wang, C. Cong, W. Yang, J. Shang, N. Peimyoo, Y. Chen, J. Kang, J. Wang, W. Huang, and T. Yu, *Strain-induced direct–indirect bandgap transition and phonon modulation in monolayer* WS_2, Nano Research **8**, 2562 (2015).

[44] C. Rice, R. J. Young, R. Zan, U. Bangert, D. Wolverson, T. Georgiou, R. Jalil, and K. S. Novoselov, *Raman-scattering measurements and first-principles calculations of strain-induced phonon shifts in monolayer* MoS_2, Physical Review B **87**, 081307 (2013).

[45] Y. Zhou, Z. Wang, P. Yang, X. Zu, L. Yang, X. Sun, and F. Gao, *Tensile Strain Switched Ferromagnetism in Layered* NbS_2 *and* $NbSe_2$, ACS Nano **6**, 9727 (2012).

[46] S. van der Lippe, A. Brokkelkamp, J. Rojo, and S. Conesa-Boj, *Localized Exciton Anatomy and BandGap Energy Modulation in 1D* MoS_2 *Nanostructures,* Advanced Functional Materials **33**, 2307610 (2023).

[47] D. B. Williams and C. B. Carter, *Transmission Electron Microscopy: A Textbook for Materials Science*, 2nd ed. (Springer, New York, NY, 2009).

2

FABRICATION OF WS_2 NANOSTRUCTURES VIA CHEMICAL VAPOR DEPOSITION

Owing to their exceptional optical and electronic properties, transition metal dichalcogenides (TMDs) hold great promise for various technological applications. Achieving practical application of TMDs necessitates controlled fabrication methods that offer scalability. Existing fabrication methods, such as exfoliation, chemical vapor deposition (CVD), and direct deposition, have been proposed in the literature. In this chapter, we focus on the CVD fabrication method in the context of TMD nanostructures, specifically two-dimensional (2D) tungsten disulfide (WS_2) nanostructures. CVD is considered the preferred fabrication method due to its ability to produce high-quality TMD materials, precise control over nanostructure dimensions and morphology, and potential for scalability. We discuss how various parameters involved in the CVD process affect growth kinetics, offering the desired level of control. Furthermore, we explore the intricate 2D nanostructure achievable through parameter optimization. Gaining an in-depth understanding of this technique enables the controlled fabrication of numerous intriguing TMD nanostructures, as demonstrated in Chapters 4 and 5 of this thesis.

2.1. INTRODUCTION

IN the dynamic and evolving field of nanotechnology, the fabrication of low-dimensional transition metal dichalcogenides (TMDs) emerges as a key area of focus. These materials, known for their unique optical and electronic properties, are at the heart of numerous potential applications in various technological fields. In recent years, the focus has shifted towards more scalable and controlled fabrication methods to meet the growing demand for high-quality TMDs in industrial applications. Several methods have been put forward in the literature, including exfoliation, chemical vapor deposition and direct deposition methods.

Exfoliation is a top-down fabrication method, where atomically thin layers of TMD materials are obtained by separating them from a bulk crystal. A distinction can be made between mechanical exfoliation and chemical exfoliation [1]. Mechanical exfoliation uses mechanical forces to separate the layers from the bulk crystal. The best-known method to achieve this is the use of adhesive tape [2]. Mechanical exfoliation results in TMD films with comparable quality to their bulk crystals [1, 3]. However, this method offers poor controllability in the number of layers [4, 5]. In addition, the exfoliation yield is low [1], making this method non-ideal for large-scale production.

On the other hand, chemical exfoliation uses methods like sonication or shearing to separate the layers in TMD crystals. This can be achieved either by using a suitable liquid to assist the process [6–9] or through chemical intercalation, which serves to widen the interlayer distances between the layers [8, 10, 11] prior to the sonication or shearing process. Chemical exfoliation typically yields a higher output and is therefore more suitable for large-scale production compared to mechanical exfoliation. However, liquid exfoliation is constrained by its relatively low monolayer yield, typically no more than a few tens of percent [4, 6, 8]. Furthermore, chemical exfoliation can lead to issues such as undesired phase transitions, chemical decomposition, and physical damage to the materials [1, 3, 12], depending on the specific process used. These issues can adversely affect the properties of the resulting TMD films.

Alternatively, TMD nanosheets can also be fabricated using direct deposition techniques. These include methods such as atomized spray casting deposition [5], sputtering [13], pulsed laser deposition [13] and e-beam evaporation [14]. Each of these techniques has its drawbacks and benefits. Generally, there is a trade-off between the ease of fabricating monolayers and achieving large-scale uniformity [5, 13, 14]. Furthermore, postprocess annealing is often required to improve the crystallinity of the fabricated films [13, 14].

Finally, chemical vapor deposition (CVD) is another method that can be utilized in the fabrication of low-dimensional TMD nanostructures. CVD yields high-quality TMD materials and allows for precise control over the number of layers, domain size, and morphology of the fabricated nanostructures [15]. This degree of control, combined with the technique's potential for high scalability [16], makes CVD a preferred method for fabricating TMD materials. Challenges associated with this techniques arise from the conditions required for material growth, such as the high temperatures necessary for CVD [4, 17, 18]. However, numerous studies have been conducted to explore ways to relax these stringent conditions [19–21].

In this chapter, we delve into the CVD fabrication of TMD nanostructures, with a particular focus of two-dimensional (2D) tungsten disulfide (WS_2) nanostructures. Initially, we provide a brief description of the CVD technique. Following this, we discuss the various parameters that influence the growth kinetics of this synthesis method, offering an overview of the diverse possibilities presented by the versatile technique. Our discussion then extends to the more complex 2D morphologies achievable through CVD. Finally, we highlight the specific CVD furnace and procedural details employed within the scope of this thesis.

2.2. CHEMICAL VAPOR DEPOSITION

CVD is a bottom-up approach to the synthesis of TMD materials. This process can be considered multi-step, beginning with the excitation of precursors into their desired vaporous phases. These gaseous species are then transported to a substrate using a carrier gas, which is assumed to flow in a laminar manner. As a result, a boundary layer exist at the interface with the substrate, where the gas velocity is zero. For the gaseous precursors to reach the substrate, they must diffuse through this boundary layer. Subsequent surface reactions on the substrate leads to the production of solid-phase materials. Lastly, any by-products created during these reactions diffuse back through the boundary layer and are removed by the main laminar flow of the carrier gas [17, 22]. The sequence of events occurring during the CVD process near the substrate is illustrated in Figure 2.1a.

Multiple variants of CVD exist that are applicable in the fabrication of TMD materials. These include direct sulfurization, in case of sulfide-based TMDs, and the vapor phase reaction method.

Sulfurization is the process where a substrate coated with a pre-deposited film of a material, in this case a transition metal (denoted as M), is exposed to a sulfur (S) containing atmosphere at a high temperature. This exposure initiates surface reactions that facilitate the formation of a new compound (MS_2), incorporating the sulfur [16]. This technique is schematically illustrated in Figure 2.1b (top).

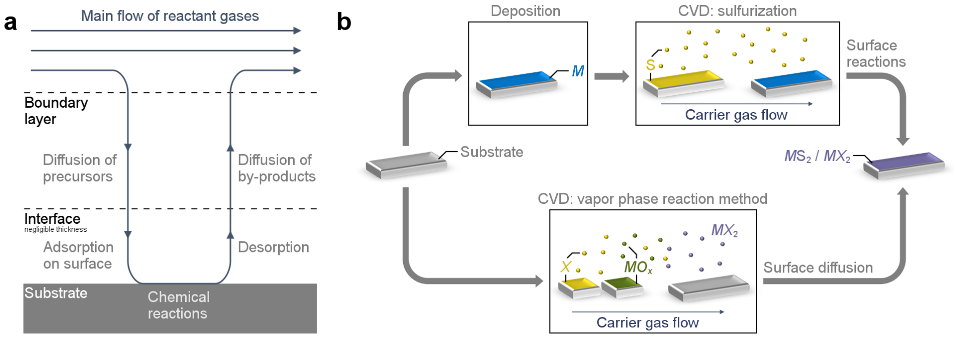
a
Main flow of reactant gases
Boundary layer
Diffusion of precursors
Diffusion of by-products
Interface
negligible thickness
Adsorption on surface
Desorption
Substrate
Chemical reactions
b
Deposition
M
CVD: sulfurization
S
Carrier gas flow
Surface reactions
Substrate
MS_2 / MX_2
CVD: vapor phase reaction method
X
MO_x
MX_2
Carrier gas flow
Surface diffusion

Figure 2.1: (a) Schematic illustration summarizing the CVD process steps taking place at the location of the substrate. Adapted with permission from [17]. Copyright © 1999 by Noyes Publications. (b) Simplified schematic overview of the CVD methods of sulfurization (top) and vapor phase reaction (bottom).

The vapor phase reaction method differs slightly from the sulfurization method. In this approach, instead of having a pre-deposited metal precursor, both the metal and chalcogen (X) precursors are kept separately from the substrate. Typically, a metal oxide compound (denoted as MO_x) is used as the metal precursor. Upon heating, chalcogen vapors induce the reduction of the metal oxide precursor, forming volatile suboxide compounds. These volatile species, including the chalcogen, are then transported to the substrate. Two potential pathways exist for the suboxide compounds to contribute to the growth of the desired TMD material (MX_2). The first pathway involves the suboxide compounds diffusing to the substrate, where they react further with the chalcogen vapors to form the TMD material. Alternatively, the TMD material can initially form in the vapor phase through continued reactions between the suboxide compounds and chalcogen vapors, and then diffuse to the substrate to produce the solid TMD material [18, 23]. To provide a clear understanding of this CVD method, a simplified schematic overview is presented in Figure 2.1b (bottom).

CVD processes are typically carried out in a CVD furnace. These furnaces often feature multiple heating zones, allowing for individual control of the evaporation temperatures of precursors and the reaction temperature at the substrate [24]. In some cases the choice is made to use a single-zone CVD furnace instead. In these cases the different required temperatures are achieved by leveraging the natural temperature gradient present within the furnace [23–26].

2.3. OPTIMIZATION OF THE CHEMICAL VAPOR DEPOSITION PROCESS FOR THE SYNTHESIS OF 2D WS_2 FLAKES

The synthesis of TMDs via CVD processes is influenced by a variety of factors. These include the properties of the substrate and precursors, as well as growth conditions like the process pressure, reaction temperature, reaction time, and the flow of atomic gas. Over the years, these influencing factors have been the focus of extensive research. In the following sections, we provide a review of some key scientific studies that have explored the effects of these factors on the CVD synthesis of 2D WS_2 nanosheets.

2.3.1. CHOICE IN SUBSTRATE MATERIALS

The choice of substrates in CVD processes is somewhat constrained, largely due to the demanding conditions of the CVD process itself. For example, the high temperatures typically required to initiate surface reactions necessitates substrates that can withstand such conditions. This aspect of CVD is often seen as a limitation, as it frequently necessitates the transfer of the synthesized TMD nanostructures to more suitable substrates for device application [4].

Furthermore, another factor that limits substrate selection is the sensitivity of TMD material growth to the properties of the substrates surface [15, 18]. This sensitivity underscores the critical role of the substrate in determining the quality and characteristics of the resulting TMD materials. At the fundamental level, the substrate used in the CVD growth of TMDs must be atomically flat and chemically inert [15, 18]. The effectiveness of inert versus non-inert substrate materials was investigated by Yanshuo Zhang and colleagues [27]. They studied the use of metal foils as substrates for synthesizing WS_2 using the vapor phase reaction method. Their findings revealed that gold films are a suitable substrate choice. However, other metal foils, including Pr-Ru alloys and Nb foils, were found to degrade during the CVD process, resulting in the conversion into powdered sulfides.

Substrates that have been found suitable for the growth of high-quality WS_2 include the aforementioned gold foils [27], magnesium oxide (MgO) [28], graphite [29], hexagonal boron nitride (h-BN) [29–31], quartz [32], sapphire [24, 29, 33–35], and the most commonly used silicon/silicon dioxide (Si/SiO_2) [19–21, 23, 25, 26, 32, 36–41].

2.3.2. PROPERTIES OF THE PRECURSORS

The properties of the precursors used in a CVD process significantly influence the growth of TMDs. In particular, these properties are crucial in determining the final morphology and yield of the grown TMD nanosheets. It is important to note here that these effects vary depending on the specific CVD methods previously discussed.

PRE-DEPOSITED FILMS AS PRECURSOR IN DIRECT SULFURIZATION

In the direct sulfurization method, the pre-deposited film acts as the metal-based precursor. The thickness of this film has been a focus of frequently study, as it is known to influence the growth orientation and the layer count of the synthesized WS_2 nanosheets.

In the synthesis of TMDs, there are two possible growth orientations: horizontal and vertical. Horizontally grown TMD layers expand in the planar direction, with their basal planes parallel to the growth substrates, as illustrated in Figure 2.2a. In contrast, vertically grown TMD layers stand upright on the substrate, exposing their edge sites rather than their basal planes (Figure 2.2b) [25]. Horizontal WS_2 layers are commonly characterized by the formation of triangular flakes and their intersections or junctions.

By altering the thickness of the pre-deposited tungsten film, the growth orientation of the resulting WS_2 nanosheets can be controlled. It has been observed that sulfurizing a tungsten film with a thickness of less than 5 nm typically leads to horizontal growth, while films thicker than 10 nm tend to yield vertical growth [23–25, 28, 32]. For films with intermediate thicknesses, a mix of both growth orientations can be observed, with the proportion of vertically aligned layers increasing as the tungsten film thickness increases [25].

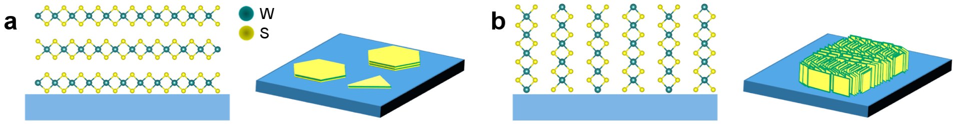

Figure 2.2: Schematic representations of (a) horizontally and (b) vertically grown TMDs. Horizontally grown TMD nanosheets are seen to have exposed basal planes, while vertically grown TMD nanosheets expose their edges instead. Adapted with permission from [25]. Copyright © 2014, American Chemical Society.

Furthermore, the thickness of the pre-deposited tungsten film is also a determining factor in the final thickness of the WS_2 nanosheets. Jung *et al.* [25] investigated the relationship between the thickness of the pre-deposited tungsten film and that of the resulting WS_2 nanosheets. Their findings indicated a linear relationship for vertical growth, with a slope of approximately 3.5. For horizontal growth, similar dependence was found, but with a slope that is 2 to 3 times smaller. This dependence in the horizontal growth was independently also discovered by Orofeo *et al.* [28]. Leveraging this knowledge, it becomes possible to fabricate large-area ($\sim$cm^2) WS_2 nanosheets with a predetermined thickness, including monolayer thickness, by precisely controlling the thickness of the pre-deposited tungsten film.

The observed slope in the relationship between film thickness and growth orientation suggests a volume expansion in the basal plane. Jung *et al.* [25] proposes that this volume expansion is crucial in the transition from vertical to horizontal growth, which is induced by changing the thickness of the pre-deposited tungsten film. For thin and often discontinuous pre-deposited films, the volume expansion upon sulfurization can easily be accommodated for through horizontal growth. However, for thicker pre-deposited films, such expansion cannot be easily accommodated for if the layers were to grow horizontally, leading to a preference for vertical growth. In cases of intermediate film thicknesses, a combination of both vertical and horizontal growth can occur. In this scenario, horizontally grown layers often become discontinuous, bent, and overlap, forming polycrystalline structures to release strain energy.

Besides using a pre-deposited tungsten film, WS_2 can also be synthesized through the sulfurization of pre-deposited tungsten trioxide (WO_3) films [36–39]. Similarly, the thickness of the pre-deposited WO_3 films is reported to determine the thickness and, consequently, the layer count of the resulting WS_2 [36–39]. For horizontally grown WS_2, the relationship between the thicknesses of the WO_3 and WS_2 layers is found to be quite similar to that observed with tungsten pre-deposited film.

POWDER-BASED PRECURSORS OF THE VAPOR PHASE REACTION METHOD PROCESSES

For the vapor phase reaction method, metal-based powders are used as precursor instead. In this method, key precursors properties that significantly influence the yield of horizontally grown WS_2 include the type and amount of the powder, as well as its distance from the substrate.

In the synthesis of WS_2 flakes, tungsten oxide-based precursors are commonly chosen, with WO_3 being the typical selection. Alternatively, the use of $WO_{2.9}$ has also been reported [20, 23]. Liu *et al.* [23] conducted a comparative study of these two powders as precursors. With all other parameters held constant, they found a higher yield of WS_2 growth when using $WO_{2.9}$ as the precursor. This increased efficiency is hypothesized to stem from the elimination of the need to reduce the WO_3 precursor in the initial stages of the growth, as previously discussed. Despite this, both WO_3 and $WO_{2.9}$ can be considered suitable precursors for the growth of WS_2.

Furthermore, the synthesis yield is influenced by the amount of precursor used and its proximity to the substrate. Yanshuo Zhang and their team [27] studied both the precursor amount and precursor-substrate distance in relation to WS_2 growth. Firstly, their study shows that an increase in the amount of available precursor significantly boost the yield of WS_2 growth. In their experiments, nearly doubling the substrate coverage was achieved by using twice the amount of WO_3. This approach enabled them to achieve full monolayer WS_2 coverage on their substrate.

Additionally, the study revealed that the distance between the precursor and substrate also influences substrate coverage. Shorter distances between the precursor and substrate led to a higher density of triangular WS_2 flakes, thereby increasing the coverage. This observed trend is attributed to the decrease in the availability of the WO_3 precursor as the distance from the source increases [27]. A similar trend in substrate coverage with varying precursor-substrate distances was observed by Yu Zhang *et al.* [33], demonstrating that this trend persists even under different reaction temperatures.

2.3.3. CVD GROWTH CONDITIONS

The morphology and size of the horizontally grown WS_2 flakes are significantly influenced by the growth conditions employed during the CVD process. Critical factors include the process pressure, reaction temperature, reaction time, and the atomic gas flow.

PROCESS PRESSURE

It is important to note that CVD processes can be carried out under both low pressure conditions and atmospheric pressure conditions. However, these pressure options generally require different sets of growth conditions to achieve successful WS_2 growth.

Researchers, such as Liu *et al.* [23] and Elías *et al.* [39], have investigated the impact of changing the process pressure. In their experiments, Liu *et al.* [23] solely changed the process pressure while keeping other parameters constants. They found the growth of 2D WS_2 films favored the atmospheric pressure CVD process over its low-pressure counterpart. Instead, Elías *et al.* [39] achieved uniform, large-area few-layer WS_2 nanostructures of a high quality using both low-pressure and atmospheric pressure procedures. Notably, they adjusted the argon flow rate, using 50 sccm for the low-pressure process and 100 sccm for the atmospheric pressure process.

REACTION TEMPERATURE

One of the critical conditions influencing the CVD synthesis of WS_2 is the reaction temperature, which refers to the temperature at which the substrate is maintained during the CVD process. This distinction becomes particularly important when dealing with CVD processes following the vapor phase reaction method. This is because, in these cases, the evaporation temperature of the tungsten-based precursor can often be regulated separately.

Regarding the influence of the reaction temperature, the following trend has been consistently reported in the literature for CVD processes employing the vapor phase reaction method. At low temperatures, no growth of WS_2 is observed. A minimum temperature threshold must be reached before triangular WS_2 flakes begin to form. These flakes tend to increase in size, sometimes by as much as an order of magnitude, as the reaction temperature is raised to a specific point. However, a further increase in reaction temperature results in a decrease in the size of the grown flakes [23, 27, 40]. It's worth noting that the exact temperatures required for WS_2 flake formation and the onset of size reduction may vary depending on the other growth conditions. Generally, a temperature around 800 °C is required for the initiation of WS_2 flakes growth, and the reduction in flake size typically starts at temperatures around 900 °C.

The hypothesized reason for the observed trend in the literature is a change in surface diffusion and reactivity of the precursors. Moderate increases in temperature facilitate surface diffusion and the reaction with sulfur, which, in turn, promotes the growth of larger flakes. However, at elevated temperatures, the adsorption amount of the sulfurized precursor declines, causing the decrease in the size of the flakes [23, 27, 40].

The effect of the reaction temperature on the growth of WS_2 nanosheets via direct sulfurization is much less well-studied. Morrish *et al.* [42] reported on this effect for vertically grown WS_2. They revealed that the reaction rate rises upon increasing the reaction temperature. Hence, an increase in reaction temperature leads to a more rapid sulfurization of the pre-deposited film. They also observed that a minimum temperature is required to achieve full sulfurization of the pre-deposited film after a fixed time. Generally, this minimally required reaction temperature is slightly lower than the temperatures needed in the vapor phase reaction method to achieve the growth of WS_2.

REACTION TIME

We define the reaction time as the duration of the process from reaching the desired temperatures until the cool-down process begins. Changing this duration leads to variations in the yield of CVD-grown WS_2 produced by the process.

In the context of the vapor phase reaction method, increasing the reaction time results in the growth of larger WS_2 flakes. However, the increase in flake size reaches a plateau at a specific reaction time, beyond which the flakes remain unchanged in size [23, 27]. Prolonging the reaction time beyond this point may lead to damage in the grown WS_2, as reported by Liu *et al.* [23].

The impact of altering the reaction time on the growth of WS_2 nanosheets through direct sulfurization is interpreted somewhat differently. In their study, Morrish *et al.* [42] investigated this phenomenon in the context of vertically grown WS_2. Their findings demonstrate that the pre-deposited film undergoes continuous sulfurization over time until the entire film has been transformed into WS_2. Extending the process beyond this point does not result in any further changes in the thickness or S:W ratio of the synthesized WS_2.

ATOMIC GAS FLOW

As discussed earlier, CVD processes utilize a carrier gas to transport the precursors to the substrate. Besides the reaction temperature and time, the growth of 2D WS_2 flakes via CVD can also be controlled by modifying the flow rate or composition of this carrier gas.

Studies on this phenomenon have revealed that altering the flow rate of the carrier gas in the vapor phase reaction method induces both changes in morphology and size. For low flow rates, the resulting WS_2 flakes exhibit a truncated triangular shape. As the flow rate is increased, the flake morphology gradually evolves to resemble an equilateral triangle (Figures 2.3a-c). Once this shape is achieved, further increase of the flow rate leads to an increase in size (Figure 2.3d) [23, 40]. However, at a certain flow rate value, this increase in size becomes unstable, and the reported effects of this instability vary. For example, Liu *et al.* [23] observed that increasing the flow rate beyond this value resulted in the edges of their monolayer WS_2 flakes becoming jagged. In contrast, Fu *et al.* [40] noted a decrease in the size of their monolayer WS_2 flakes.

The observed trend in morphology and size changes can be attributed to the availability of precursors at the reaction site. It is hypothesized that WS_2 monolayers initially assume a hexagonal shape during their formation. The edges of this hexagonal shape exhibit slight variations in atomic structure, resulting in different growth rates along these edges. Increasing the atomic gas flow in the CVD process alters the ratio of available precursors. This change promotes the growth of three out of the six edges of the hexagonal-shaped flake, leading to the transformation in morphology from hexagonal to truncated triangle, and eventually to an equilateral triangle. Furthermore, the increased flow rate enhances the mass transfer process, resulting in an increase in the size of the grown flakes. When the flow rate exceeds its optimal value and becomes too high, the gas carries away the precursor species before they can reach the correct location on the substrate. This can lead to defect formation [23] or a reduction in flake size [40].

A similar effect is anticipated for the direct sulfurization method [41], where the rate of sulfurization of the pre-deposited film initially increases and subsequently decreases with an increase in the flow rate of the carrier gas.

Apart from the flow rate, the composition of the carrier gas can also play a role in changing the growth kinetics of 2D WS_2 flakes. Argon is the most commonly used carrier gas for WS_2 synthesis. However, deviating from this composition under specific conditions may yield improved results.

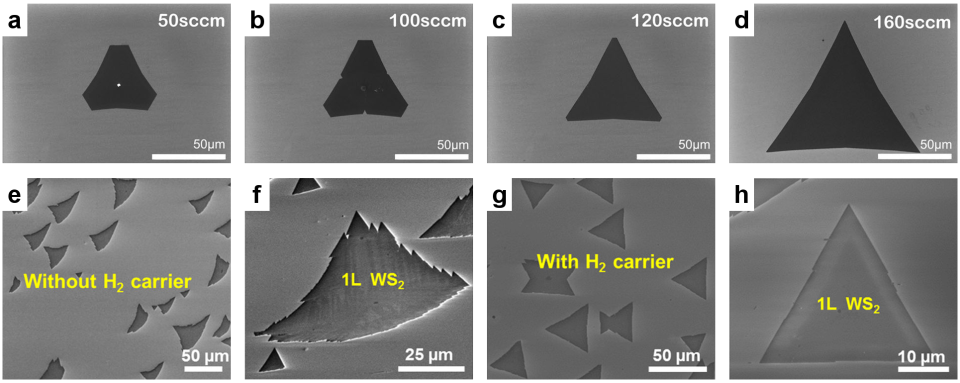

Figure 2.3: Scanning electron microscopy (SEM) images of WS_2 flakes fabricated by the vapor phase reaction method, where the synthesis was carrier out under various conditions of the carrier gas. (a-d) WS_2 flakes grown on a Si/SiO_2 substrate under various flow rates of a pure argon carrier gas flow. Adapted with permission from [23]. Copyright © 2017, CC BY 4.0. (e-h) WS_2 flakes grown on a sapphire substrate using a carrier gas of (e-f) pure argon and (g-h) a mixture of argon and H_2. Adapted with permission from [33]. Copyright © 2013, American Chemical Society.

An example of this phenomenon was demonstrated by Yu Zhang *et al.* [33] in their study. They aimed to synthesize large-area, high-quality WS_2 flakes on sapphire substrates using the vapor phase reaction method. Their process was carrier out under low pressure, at a reaction temperature of 900 °C, and for a reaction time of 1 hour. When they used argon as the carrier gas, they observed the growth of asymmetrical triangular WS_2 flakes with jagged edges on the sapphire substrate (Figures 2.3e-f). However, when they replaced the carrier gas with a mixture of argon and a small amount of hydrogen (H_2), the resulting WS_2 flakes exhibited an equilateral triangular shape with straight edges (Figures 2.3g-h). One possible reason for this change is the fact that H_2 is a reductive reagent that more strongly promotes the reduction of WO_3 compared to sulfur. By facilitating the reduction of WO_3, it creates a rich WO_{3-x} environment, which favors the formation of equilateral triangular-shaped flakes.

2.3.4. ADDITION OF CATALYSTS

The growth of high-quality WS_2 via CVD typically necessitates high temperatures, especially when employing the vapor phase reaction method. These high temperatures impose limitations on the choice of substrate materials, often requiring transfer of as-grown materials to different substrates for device applications [4]. However, there are methods that can reduce the required temperature. One such method involves the use of a catalyst within the CVD process.

Thangaraja *et al.* [19] investigated the use of the WO_3 powder itself as a catalyst. They found that by deposition WO_3 powder directly on the growth substrate, they could grow large (several tens of micrometers) high-quality WS_2 monolayers at a temperature of 750 °C. Without the presence of the WO_3 powder on top of the substrate, growth at this temperature would not occur.

Alternatively, Li *et al.* [20] explored the use of various alkali metal halides as catalyst in the growth of WS_2. In their study, they mixed these alkali metal halides with $WO_{2.9}$ powder and kept this mixture separate from the substrate. They achieved the growth of large, highly crystalline WS_2 monolayers at reaction temperatures as low as 700 °C, depending on the specific alkali metal halides used. They attribute this relaxation of the growth conditions to the formation of tungsten oxyhalide species. These species have significantly lower melting points, making them more volatile compared to WO_3 and $WO_{2.9}$. The resulting monolayers were found to be pure WS_2, free from impurities or contamination due to the alkali metal halides.

Significantly lower reaction temperatures can be achieved by using tellurium as a catalyst. This was demonstrated in a study by Gong *et al.* [21], where a mixture of tungsten and tellurium powder deposited on the substrate reduced the reaction temperature to 500 °C. It is important to emphasize that bulk tungsten powder is not commonly used in the fabrication of WS_2. Tungsten oxide compounds are preferred as their melting point is much lower than that of pure tungsten [21]. Therefore, using bulk tungsten powder without the assistance of tellurium would likely necessitate even higher temperatures compared to similar processes using WO_3 or $WO_{2.9}$. The introduction of tellurium significantly relaxes the required growth conditions without compromising the quality of the micrometer-sized WS_2 monolayers or leaving unwanted residues.

Catalyst can play a crucial role not only in relaxing the growth conditions but also in controlling the morphology of 2D WS_2 nanostructures. For example, McCreary *et al.* [26] demonstrated the use of perylene-3,4,9,10-tetracarboxylic acid tetrapotassium salt (PTAS) as a catalyst, which allowed for the growth of continuous monolayer WS_2 films on a millimeter scale. Without the use of this catalyst, their CVD recipe primarily yielded truncated triangular WS_2 flakes grown on only a portion of the provided substrate. However, when PTAS was used as a catalyst, a small amount of PTAS contamination could also be found on the substrate.

In another study, Liang *et al.* [35] explored the use of carbon nanoparticles as a catalyst to achieve a better control in morphology. They successfully achieved the growth of strictly bilayer WS_2 flakes, tens of micrometers in size, by using this catalyst. These WS_2 bilayers were of high quality and free of contamination.

2.4. MORPHOLOGY CONTROL IN CHEMICAL VAPOR DEPOSITION PROCESSES

CVD techniques offer a high degree of control over the morphology of fabricated nanostructures. While we have highlighted examples of this control in the previous section, primarily focusing on simple 2D WS_2 nanostructures, it is important to note that this morphological control extends beyond these structures. CVD can be employed to create a wide range of more complex and intricate nanostructures with precise control.

One such complex nanostructure is denoted as the nanoflower [43–45], which will be explored in Chapter 4. These nanostructures possess flower-like morphologies composed of randomly oriented flakes arising from a common point. Due to their morphology, these nanostructures possesses a vast amount of exposed edges combined with a large surface area. Edge-rich TMD nanostructures have been reported to exhibit various enhanced properties, which could be beneficial for their use in various applications. For instance, they exhibit enhanced catalytic performance [46–52]. This as a result of the edges serving as active sites for chemical reactions, as opposed to the inert basal plane [48].

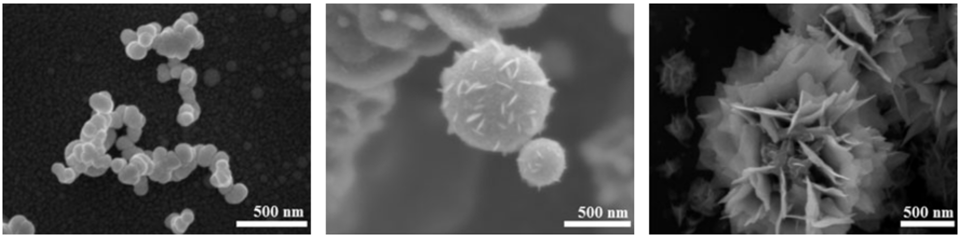

Figure 2.4: Observed growth evolution of WS_2 nanoflowers by Prabakaran *et al.* [43]. Nanoflowers are found to evolve from small flakes growing on tungsten nanoparticles formed during the initial stages of the CVD fabrication process. Used with permission of the Royal Society of Chemistry, from [43] © 2014; permission conveyed through Copyright Clearance Center, Inc.

This characteristic makes them promising candidates as catalyst for applications such as the hydrogen evolution reaction (HER) [46–48, 50], carbon dioxide reduction [51, 52], and gas sensing [49]. Furthermore, the random orientation of the flakes that make up the nanoflowers provides opportunities for light trapping [53]. Additionally, nanoflowers have also been found to perform exceptionally well as field emitter [44, 45, 54], thanks to their exposed edges and overall morphology.

Prabakaran *et al.* [43] reported on the growth evolution of these flower-like nanostructures (Figure 2.4). They observed the formation of nanoparticles in the initial stages of growth. Continued reactions between the nanoparticles and sulfur vapors led to the growth of flake-like structures on these nanoparticles. Finally, these WS_2 flakes transformed the nanoparticles into the nanoflower morphology.

Another type of WS_2 nanostructure that possesses an increased number of exposed edges is pyramid-like structures [55, 57–59]. However, these structures are primarily studied for their intriguing electronic properties, such as ferromagnetism [60] and high mobility [61, 62], as well as optical properties [55, 57, 59], including their improved non-linear response compared to mono- and few-layer structures [59].

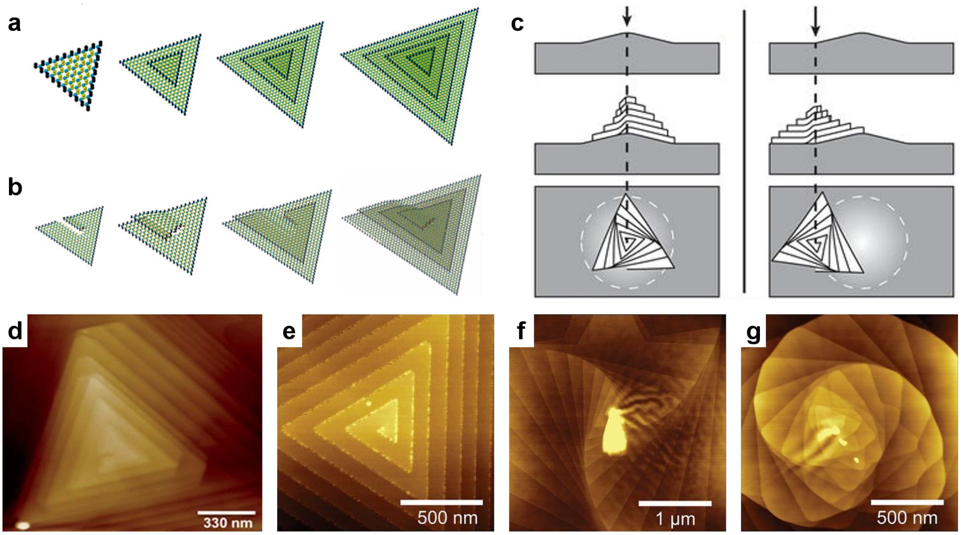

Figure 2.5: (a-b) Schematic illustrations of the (a) layer-by-layer growth mechanism and (b) screw-dislocation-driven growth mechanism. Adapted with permission from [55]. Copyright © 2018, American Chemical Society. (c) Schematic illustration showing the effects of non-Euclidean surfaces on the growth of spiral pyramid-like structures. A protruded substrate where the protrusion and the center of the screw dislocation align yields a fastened supertwisted spiral (left), while if it's aligned with the edge an unfastened supertwisted spiral is obtained (right). From [56]/ Reprinted with permission from AAAS. (d-g) Atomic force microscopy (AFM) images of a (d) layer-by-layer grown simple pyramid-like structure and (e) spiraling pyramid-like structure grown on flat surfaces, as well as (f-g) supertwisted spirals grown on non-Euclidean surfaces. (d) Used with permission of the Royal Society of Chemistry, from [57] © 2016; permission conveyed through Copyright Clearance Center, Inc. (e-g) From [56]/ Reprinted with permission from AAAS.

Pyramid-like structures come in various forms. In its simplest form, it consists of an aligned stack of layers, each slightly smaller than the preceding one (Figure 2.5d). The growth of these pyramid-like structures follows the layer-by-layer growth mechanism as shown in Figure 2.5a. A more complex structure (Figure 2.5e) arises when its growth instead follows a screw-dislocation-driven growth mechanism (Figure 2.5b). One can control the growth mechanism by adjusting the concentration of the tungsten-based precursor [55, 57]. Low concentrations promote screw-dislocation-driven growth, while high concentrations promote growth via the layer-by-layer mechanism.

As mentioned earlier, twisting provides an additional means to tune the properties of TMD nanostructures. Beyond twisted bilayers [63, 64], a recent study by Zhao *et al.* [56] has shown the possibility of obtaining continuously twisted multilayer structures called supertwisted spirals (Figure 2.5f-g). While the previously discussed aligned spiraling pyramid-like structures can be grown on flat surfaces, the introduction of non-Euclidean surfaces provides a method to synthesize twisted subsequent spiraling layers at a fixed angle. These non-Euclidean surfaces can be created by the introduction of protrusions on a substrate, for example, as a result of the deposition of nanoparticles. These protrusions locally create cone and hyperbolic-shaped surfaces, yielding the growth of "fastened" (right-handed) or "unfastened" (left-handed) supertwisted spirals, respectively, as depicted in Figure 2.5c. In Chapter 5 we study twisted superstructures, including those resembling the supertwisted spirals discussed by Zhao *et al.* [56].

2.5. CHEMICAL VAPOR DEPOSITION FURNACE AND PROCEDURE FOR THE FABRICATION OF WS_2 NANOSTRUCTURES

Figure 2.6 provides a schematic illustration of the Carbolite Gero gradient tube furnace used for the fabrication of the WS_2 nanostructures explored in Chapters 4 and 5, as briefly introduced in the previous section. This furnace consists of a long quartz reactor tube placed inside an electric oven. This electric oven features three separate heating elements, creating three heating zones within the furnace, enabling individual temperature control. It is important to note that due to limited thermal isolation, heating in one zone might cause a temperature increase in the neighboring zone(s) when the temperature gradient becomes too large.

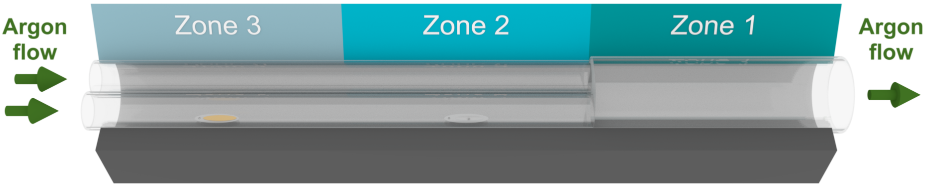

Figure 2.6: Schematic illustration of the three-zone gradient tube furnace from Carbolite Gero. This furnace is connected to an argon gas source at the entrance (at zone 3), and a bubbler system and subsequent exhaust at the back end (at zone 1). For the synthesis of WS_2, sulfur powder is provides as chalcogen precursor in zone 3, while the substrate and tungsten-based precursor are loaded in zone 2.

A gas system is integrated into the setup, allowing for an argon flow from the source, connected to the entrance (located at zone 3), to the exhaust at the back end (positioned at zone 1). Using a flow rate meter, the flow rate of the argon carrier gas can be precisely regulated within a range of 100 to 1000 sccm. Since the argon flow is split between the two tubes present in the system, each tube will receive half of the flow rate set on the flow rate meter. At the back end of the furnace, the gas is passed through a bubbler system before being safely disposed of via the exhaust.

The procedure adopted for the atmospheric pressure CVD growth of WS$_2$ using this system is schematically represented in Figure 2.7. Two of the three available zones are used during this procedure. The central zone (zone 2) holds the substrate and tungsten-based precursor, while sulfur powder is loaded upstream in zone 3. After loading the crucibles containing the substrate and precursors, the system undergoes a pretreatment to remove any oxygen remnants. During this pretreatment, the system is flushed with a 500 sccm argon flow for 30 minutes (t_{pre}).

Following this pretreatment, the temperature of the central zone (zone 2) is ramped up at a target rate of 10 °C/min. This temperature ramping continues until this zone reaches the desired reaction temperature (T_{reaction}). The argon flow is reduced from 500 sccm to the desired reaction flow rate once a temperature of 500 °C has been attained. Once the desired reaction temperature has been reached, zone 3 is heated to a temperature of 220 °C (T_{sulfur}). Upon reaching the respective target temperature in zone 3, the CVD furnace is maintained at the reaction conditions for the duration of the reaction time (t_{reaction}). When the reaction time has elapsed, the furnace is allowed to cool down naturally to room temperature under continued argon flow.

It is important to note that for high reaction temperatures (exceeding 700 °C), the target temperature of zone 3 (220 °C) may be reached before the desired reaction temperature is realized in zone 2, due to the limited thermal isolation between the heating zones. In such cases, the reaction time is defined to start when zone 2 reaches the desired reaction temperature. As, at that moment, both zones have reached or exceeded their respective target temperatures.

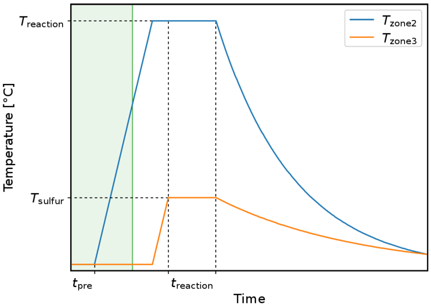

Figure 2.7: Representation of the temperature control aimed for within the atmospheric pressure CVD growth of WS$_2$ using the system depicted in Figure 2.6. The ideal profile of the temperature for both zone 2 (T_{zone2}) and zone 3 (T_{zone3}) are given. Here, perfect thermal isolation is assumed. The green shaded area illustrates the time period for which the flow rate is 500 sccm. After this, a reduced argon flow rate is supplied to the system.

REFERENCES

[1] Z. Zhang, P. Yang, M. Hong, S. Jiang, G. Zhao, J. Shi, Q. Xie, and Y. Zhang, *Recent progress in the controlled synthesis of 2D metallic transition metal dichalcogenides,* Nanotechnology **30**, 182002 (2019).

[2] R. F. Frindt, *Single Crystals of MoS_2 Several Molecular Layers Thick,* Journal of Applied Physics **37**, 1928 (1966).

[3] R. Gatensby, T. Hallam, K. Lee, N. McEvoy, and G. S. Duesberg, *Investigations of vapour-phase deposited transition metal dichalcogenide films for future electronic applications,* Solid-State Electronics **125**, 39 (2016).

[4] X. Yu and K. Sivula, *Layered 2D semiconducting transition metal dichalcogenides for solar energy conversion,* Current Opinion in Electrochemistry **2**, 97 (2017).

[5] H. Y. Qi, W. T. Mi, H. M. Zhao, T. Xue, Y. Yang, and T. L. Ren, *A large-scale spray casting deposition method of WS_2 films for high-sensitive, flexible and transparent sensor,* Materials Letters **201**, 161 (2017).

[6] E. Varrla, C. Backes, K. R. Paton, A. Harvey, Z. Gholamvand, J. McCauley, and J. N. Coleman, *Large-Scale Production of Size-Controlled MoS_2 Nanosheets by Shear Exfoliation,* Chemistry of Materials **27**, 1129 (2015).

[7] R. J. Smith, P. J. King, M. Lotya, C. Wirtz, U. Khan, S. De, A. O'Neill, G. S. Duesberg, J. C. Grunlan, G. Moriarty, J. Chen, J. Wang, A. I. Minett, V. Nicolosi, and J. N. Coleman, *Large-Scale Exfoliation of Inorganic Layered Compounds in Aqueous Surfactant Solutions,* Advanced Materials **23**, 3944 (2011).

[8] V. Nicolosi, M. Chhowalla, M. G. Kanatzidis, M. S. Strano, and J. N. Coleman, *Liquid Exfoliation of Layered Materials,* Science **340**, 1226419 (2013).

[9] J. N. Coleman, M. Lotya, A. O'Neill, S. D. Bergin, P. J. King, U. Khan, K. Young, A. Gaucher, S. De, R. J. Smith, I. V. Shvets, S. K. Arora, G. Stanton, H.-Y. Kim, K. Lee, G. T. Kim, G. S. Duesberg, T. Hallam, J. J. Boland, J. J. Wang, J. F. Donegan, J. C. Grunlan, G. Moriarty, A. Shmeliov, R. J. Nicholls, J. M. Perkins, E. M. Grieveson, K. Theuwissen, D. W. McComb, P. D. Nellist, and V. Nicolosi, *Two-Dimensional Nanosheets Produced by Liquid Exfoliation of Layered Materials,* Science **331**, 568 (2011).

[10] Z. Qin, D. Zeng, J. Zhang, C. Wu, Y. Wen, B. Shan, and C. Xie, *Effect of layer number on recovery rate of WS_2 nanosheets for ammonia detection at room temperature,* Applied Surface Science **414**, 244 (2017).

[11] P. Joensen, R. F. Frindt, and S. R. Morrison, *Single-layer MoS_2,* Materials Research Bulletin **21**, 457 (1986).

[12] Z. Lin, Y. Liu, U. Halim, M. Ding, Y. Liu, Y. Wang, C. Jia, P. Chen, X. Duan, C. Wang, F. Song, M. Li, C. Wan, Y. Huang, and X. Duan, *Solution-processable 2D semiconductors for high-performance large-area electronics,* Nature **562**, 254 (2018).

[13] C. Muratore, A. A. Voevodin, and N. R. Glavin, *Physical vapor deposition of 2D Van der Waals materials: a review,* Thin Solid Films **688**, 137500 (2019).

[14] S. Hussain and S. Dam, *Synthesis of vertically stacked, highly oriented* WS_2 *thin films by Electron beam evaporation,* Thin Solid Films **734**, 138851 (2021).

[15] P.-C. Shen, Y. Lin, H. Wang, J.-H. Park, W. S. Leong, A.-Y. Lu, T. Palacios, and J. Kong, *CVD Technology for 2-D Materials,* IEEE Transactions on Electron Devices **65**, 4040 (2018).

[16] Y. Shi, H. Li, and L.-J. Li, *Recent advances in controlled synthesis of two-dimensional transition metal dichalcogenides via vapour deposition techniques,* Chemical Society Reviews **44**, 2744 (2015).

[17] H. O. Pierson, *Handbook of Chemical Vapor Deposition (CVD): Principles, Technology, and Applications*, 2nd ed. (Noyes Publications / William Andrew Publishing, LLC, Norwich, NY, 1999).

[18] H. Li, Y. Li, A. Aljarb, Y. Shi, and L.-J. Li, *Epitaxial Growth of Two-Dimensional Layered Transition-Metal Dichalcogenides: Growth Mechanism, Controllability, and Scalability,* Chemical Reviews **118**, 6134 (2018).

[19] A. Thangaraja, S. M. Shinde, G. Kalita, and M. Tanemura, *Effect of* WO_3 *precursor and sulfurization process on* WS_2 *crystals growth by atmospheric pressure CVD,* Materials Letters **156**, 156 (2015).

[20] S. Li, S. Wang, D.-M. Tang, W. Zhao, H. Xu, L. Chu, Y. Bando, D. Golberg, and G. Eda, *Halide-assisted atmospheric pressure growth of large* WSe_2 *and* WS_2 *monolayer crystals,* Applied Materials Today **1**, 60 (2015).

[21] Y. Gong, Z. Lin, G. Ye, G. Shi, S. Feng, Y. Lei, A. L. Elías, N. Perea-Lopez, R. Vajtai, H. Terrones, Z. Liu, M. Terrones, and P. M. Ajayan, *Tellurium-Assisted Low-Temperature Synthesis of* MoS_2 *and* WS_2 *Monolayers,* ACS Nano **9**, 11658 (2015).

[22] A. Stoffel, A. Kovács, W. Kronast, and B. Müller, *LPCVD against PECVD for micromechanical applications,* Journal of Micromechanics and Microengineering **6**, 1 (1996).

[23] P. Liu, T. Luo, J. Xing, H. Xu, H. Hao, H. Liu, and J. Dong, *Large-Area* WS_2 *Film with Big Single Domains Grown by Chemical Vapor Deposition,* Nanoscale Research Letters **12**, 558 (2017).

[24] I. Hotovy, L. Spiess, M. Sojkova, I. Kostic, M. Mikolasek, M. Predanocy, H. Romanus, M. Hulman, and V. Rehacek, *Structural and optical properties of* WS_2 *prepared using sulfurization of different thick sputtered tungsten films,* Applied Surface Science **461**, 133 (2018).

[25] Y. Jung, J. Shen, Y. Liu, J. M. Woods, Y. Sun, and J. J. Cha, *Metal Seed Layer Thickness-Induced Transition From Vertical to Horizontal Growth of* MoS_2 *and* WS_2*,* Nano Letters **14**, 6842 (2014).

[26] K. M. McCreary, A. T. Hanbicki, G. G. Jernigan, J. C. Culbertson, and B. T. Jonker, *Synthesis of Large-Area WS_2 monolayers with Exceptional Photoluminescence,* Scientific Reports **6**, 19159 (2016).

[27] Y. Zhang, J. Shi, G. Han, M. Li, Q. Ji, D. Ma, Y. Zhang, C. Li, X. Lang, Y. Zhang, and Z. Liu, *Chemical vapor deposition of monolayer WS_2 nanosheets on Au foils toward direct application in hydrogen evolution,* Nano Research **8**, 2881 (2015).

[28] C. M. Orofeo, S. Suzuki, Y. Sekine, and H. Hibino, *Scalable synthesis of layer-controlled WS_2 and MoS_2 sheets by sulfurization of thin metal films,* Applied Physics Letters **105**, 083112 (2014).

[29] Y. Kobayashi, S. Sasaki, S. Mori, H. Hibino, Z. Liu, K. Watanabe, T. Taniguchi, K. Suenaga, Y. Maniwa, and Y. Miyata, *Growth and Optical Properties of High-Quality Monolayer WS_2 on Graphite,* ACS Nano **9**, 4056 (2015).

[30] M. Okada, T. Sawazaki, K. Watanabe, T. Taniguch, H. Hibino, H. Shinohara, and R. Kitaura, *Direct Chemical Vapor Deposition Growth of WS_2 Atomic Layers on Hexagonal Boron Nitride,* ACS Nano **8**, 8273 (2014).

[31] Y. Zhao, Z. Zhang, J. Huang, L. Feng, L. Cao, X. Li, T. Liu, Q. Zong, and H. Wang, *Salt-promoted growth of monolayer tungsten disulfide on hexagonal boron nitride using all chemical vapor deposition approach,* Applied Surface Science **605**, 154812 (2022).

[32] N. Perea-López, A. L. Elías, A. Berkdemir, A. Castro-Beltran, H. R. Gutiérrez, S. Feng, R. Lv, T. Hayashi, F. López-Urías, S. Ghosh, B. Muchharla, S. Talapatra, H. Terrones, and M. Terrones, *Photosensor Device Based on Few-Layered WS_2 Films,* Advanced Functional Materials **23**, 5511 (2013).

[33] Y. Zhang, Y. Zhang, Q. Ji, J. Ju, H. Yuan, J. Shi, T. Gao, D. Ma, M. Liu, Y. Chen, X. Song, H. Y. Hwang, Y. Cui, and Z. Liu, *Controlled Growth of High-Quality Monolayer WS_2 Layers on Sapphire and Imaging Its Grain Boundary,* ACS Nano **7**, 8963 (2013).

[34] Z.-Q. Xu, Y. Zhang, S. Lin, C. Zheng, Y. L. Zhong, X. Xia, Z. Li, P. J. Sophia, M. S. Fuhrer, Y.-B. Cheng, and Q. Bao, *Synthesis and Transfer of Large-Area Monolayer WS_2 Crystals: Moving Toward the Recyclable Use of Sapphire Substrates,* ACS Nano **9**, 6178 (2015).

[35] J. Liang, L. Zhang, X. Li, B. Pan, T. Luo, D. Liu, C. Zou, N. Liu, Y. Hu, K. Yang, and S. Huang, *Carbon-nanoparticle-assisted growth of high quality bilayer WS_2 by atmospheric pressure chemical vapor deposition,* Nano Research **12**, 2802 (2019).

[36] H. R. Gutiérrez, N. Perea-López, A. L. Elías, A. Berkdemir, B. Wang, R. Lv, F. López-Urías, V. H. Crespi, H. Terrones, and M. Terrones, *Extraordinary Room-Temperature Photoluminescence in Triangular WS_2 Monolayers,* Nano Letters **13**, 3447 (2013).

[37] A. Berkdemir, H. R. Gutiérrez, A. R. Botello-Méndez, N. Perea-López, A. L. Elías, C.-I. Chia, B. Wang, V. H. Crespi, F. López-Urías, J.-C. Charlier, H. Terrones, and M. Terrones, *Identification of individual and few layers of WS_2 using Raman Spectroscopy,* Scientific Reports **3**, 1755 (2013).

[38] J.-G. Song, J. Park, W. Lee, T. Choi, H. Jung, C. W. Lee, S.-H. Hwang, J. M. Myoung, J.-H. Jung, S.-H. Kim, C. Lansalot-Matras, and H. Kim, *Layer-Controlled, Wafer-Scale, and Conformal Synthesis of Tungsten Disulfide Nanosheets Using Atomic Layer Deposition,* ACS Nano **7**, 11333 (2013).

[39] A. L. Elías, N. Perea-López, A. Castro-Beltrán, A. Berkdemir, R. Lv, S. Feng, A. D. Long, T. Hayashi, Y. A. Kim, M. Endo, H. R. Gutiérrez, N. R. Pradhan, L. Balicas, T. E. Mallouk, F. López-Urías, H. Terrones, and M. Terrones, *Controlled Synthesis and Transfer of Large-Area* WS_2 *Sheets: From Single Layer to Few Layers,* ACS Nano **7**, 5235 (2013).

[40] Q. Fu, W. Wang, L. Yang, J. Huang, J. Zhang, and B. Xiang, *Controllable synthesis of high quality monolayer* WS_2 *on a* SiO_2*/Si substrate by chemical vapor deposition,* RSC Advances **5**, 15795 (2015).

[41] M. Bolhuis, J. Hernandez-Rueda, S. E. van Heijst, M. Tinoco Rivas, L. Kuipers, and S. Conesa-Boj, *Vertically-oriented* MoS_2 *nanosheets for nonlinear optical devices,* Nanoscale **12**, 10491 (2020).

[42] R. Morrish, T. Haak, and C. A. Wolden, *Low-Temperature Synthesis of n-Type* WS_2 *Thin Films via* H_2S *Plasma Sulfurization of* WO_3*,* Chemistry of Materials **26**, 3986 (2014).

[43] A. Prabakaran, F. Dillon, J. Melbourne, L. Jones, R. J. Nicholls, P. Holdway, J. Britton, A. A. Koos, A. Crossley, P. D. Nellist, and N. Grobert, WS_2 *2D nanosheets in 3D nanoflowers,* Chemical Communications **50**, 12360 (2014).

[44] X. Li, J. Ge, and Y. Li, *Atmospheric Pressure Chemical Vapor Deposition: An Alternative Route to Large-Scale* MoS_2 *and* WS_2 *Inorganic Fullerene-like Nanostructures and Nanoflowers,* Chemistry – A European Journal **10**, 6163 (2004).

[45] Y. B. Li, Y. Bando, and D. Golberg, MoS_2 *nanoflowers and their field-emission properties,* Applied Physics Letters **82**, 1962 (2003).

[46] T. F. Jaramillo, K. P. Jorgensen, J. Bonde, J. H. Nielsen, S. Horch, and I. Chorkendorff, *Identification of Active Edge Sites for Electrochemical* H_2 *Evolution from* MoS_2 *Nanocatalysts,* Science **317**, 100 (2007).

[47] R. J. Toh, Z. Sofer, J. Luxa, D. Sedmidubský, and M. Pumera, *3R phase of* MoS_2 *and* WS_2 *outperforms the corresponding 2H phase for hydrogen evolution,* Chemical Communications **53**, 3054 (2017).

[48] J. Kibsgaard, Z. Chen, B. N. Reinecke, and T. F. Jaramillo, *Engineering the surface structure of* MoS_2 *to preferentially expose active edge sites for electrocatalysis,* Nature Materials **11**, 963 (2012).

[49] S.-Y. Cho, S. J. Kim, Y. Lee, J.-S. Kim, W.-B. Jung, H.-W. Yoo, J. Kim, and H.-T. Jung, *Highly Enhanced Gas Adsorption Properties in Vertically Aligned* MoS_2 *Layers,* ACS Nano **9**, 9314 (2015).

[50] H. Wang, Q. Zhang, H. Yao, Z. Liang, H.-W. Lee, P.-C. Hsu, G. Zheng, and Y. Cui, *High Electrochemical Selectivity of Edge versus Terrace Sites in Two-Dimensional Layered* MoS_2 *Materials,* Nano Letters **14**, 7138 (2014).

[51] M. Asadi, B. Kumar, A. Behranginia, B. A. Rosen, A. Baskin, N. Repnin, D. Pisasale, P. Phillips, W. Zhu, R. Haasch, R. F. Klie, P. Král, J. Abiade, and A. Salehi-Khojin, *Robust carbon dioxide reduction on molybdenum disulphide edges,* Nature Communications **5**, 4470 (2014).

[52] A. J. Meier, A. Garg, B. Sutter, J. N. Kuhn, and V. R. Bhethanabotla, MoS_2 *Nanoflowers as a Gateway for Solar-Driven* CO_2 *Photoreduction,* ACS Sustainable Chemistry & Engineering **7**, 265 (2019).

[53] B. Rahmati, I. Hajzadeh, R. Karimzadeh, and S. M. Mohseni, *Facile, scalable and transfer free vertical-*MoS_2 *nanostructures grown on Au/*SiO_2 *patterned electrode for photodetector application,* Applied Surface Science **455**, 876 (2018).

[54] F. Giubileo, A. Grillo, M. Passacantando, F. Urban, L. Iemmo, G. Luongo, A. Pelella, M. Loveridge, L. Lozzi, and A. Di Bartolomeo, *Field Emission Characterization of* MoS_2 *Nanoflowers,* Nanomaterials **9**, 717 (2019).

[55] X. Fan, Y. Zhao, W. Zheng, H. Li, X. Wu, X. Hu, X. Zhang, X. Zhu, Q. Zhang, X. Wang, B. Yang, J. Chen, S. Jin, and A. Pan, *Controllable Growth and Formation Mechanisms of Dislocated* WS_2 *Spirals,* Nano Letters **18**, 3885 (2018).

[56] Y. Zhao, C. Zhang, D. D. Kohler, J. M. Scheeler, J. C. Wright, P. M. Voyles, and S. Jin, *Supertwisted spirals of layered materials enabled by growth on non-Euclidean surfaces,* Science **370**, 442 (2020).

[57] P. V. Sarma, P. D. Patil, P. K. Barman, R. N. Kini, and M. M. Shaijumon, *Controllable growth of few-layer spiral* WS_2, RSC Advances **6**, 376 (2016).

[58] G. H. Ryu, J. Chen, Y. Wen, S. Zhou, R.-J. Chang, and J. H. Warner, *Atomic structural catalogue of defects and vertical stacking in 2H/3R mixed polytype multilayer* WS_2 *pyramids,* Nanoscale **11**, 10859 (2019).

[59] I. Komen, S. E. van Heijst, S. Conesa-Boj, and L. Kuipers, *Morphology-induced spectral modification of self-assembled* WS_2 *pyramids,* Nanoscale Advances **3**, 6427 (2021).

[60] Q. Zhou, S. Su, P. Cheng, X. Hu, M. Zeng, X. Gao, Z. Zhang, and J.-M. Liu, *Robust ferromagnetism in zigzag-edge rich* MoS_2 *pyramids,* Nanoscale **10**, 11578 (2018).

[61] J. Zheng, X. Yan, Z. Lu, H. Qiu, G. Xu, X. Zhou, P. Wang, X. Pan, K. Liu, and L. Jiao, *High-Mobility Multilayered* MoS_2 *Flakes with Low Contact Resistance Grown by Chemical Vapor Deposition,* Advanced Materials **29**, 1604540 (2017).

[62] L. Chen, B. Liu, A. N. Abbas, Y. Ma, X. Fang, Y. Liu, and C. Zhou, *Screw-Dislocation-Driven Growth of Two-Dimensional Few-Layer and Pyramid-like* WSe_2 *by Sulfur-Assisted Chemical Vapor Deposition,* ACS Nano **8**, 11543 (2014).

[63] S. Zheng, L. Sun, X. Zhou, F. Liu, Z. Liu, Z. Shen, and H. J. Fan, *Coupling and Interlayer Exciton in Twist-Stacked* WS_2 *Bilayers,* Advanced Optical Materials **3**, 1600 (2015).

[64] S. Carr, D. Massatt, S. Fang, P. Cazeaux, M. Luskin, and E. Kaxiras, *Twistronics: Manipulating the electronic properties of two-dimensional layered structures through their twist angle,* Physical Review B **95**, 075420 (2017).

3

TRANSMISSION ELECTRON MICROSCOPY TECHNIQUES: THE CHARACTERIZATION OF WS_2 NANOSTRUCTURES

Transmission electron microscopy (TEM) represents a powerful tool for characterizing transition metal dichalcogenides (TMDs) and other two-dimensional (2D) layered materials. It enables simultaneous inspection of their structural, chemical and physical properties with unprecedented spatial and spectral resolution, covering spatial ranges from the atomic scale up to the micrometer level and beyond. TEM-based techniques, such as scanning transmission electron microscopy (STEM) for the structural characterization and electron energy-loss spectroscopy (EELS) for local electronic properties, among others, play a pivotal role in achieving this. Employing four-dimensional (4D) STEM coupled with an electron microscope pixel array detector (EMPAD), opens the door to extracting a vast wealth of additional information, including details about variations in strain fields across specimens. To fully exploit the potential of TEM-based techniques, comprehensive data analysis is required. Therefore, two analysis frameworks have been developed to aid in interpreting EELS and 4D STEM-EMPAD datasets. This chapter provides an overview of the methodology behind these analysis frameworks and demonstrates their full functionality through case studies. Moreover, the analysis frameworks are employed in characterizing the nanostructures presented in Chapters 4 and 5 of this thesis.

3.1. INTRODUCTION

THE unique functionalities of two-dimensional (2D) layered materials, including transition metal dichalcogenides (TMDs), are highly sensitive to structural variations, even at the single atom scale. Gaining insights to understand the close relationship between structural, chemical, and physical properties would open the door to the application of TMDs as building blocks of next-generation nanodevices. Motivated by this, the properties of these materials and their correlation have been the focus of extensive research. Commonly used techniques adopted in these studies include photoluminescence (PL) [1–6] and Raman spectroscopy [5–10]. Today, however, transmission electron microscopy (TEM) is arguably the most efficient and versatile tool for the characterization of novel materials over spatial ranges from the atomic scale up to the micrometer level and beyond [11]. This is mostly due to all the improvements within this technique in terms of both spatial and energy resolution. This excellent spatial and spectral resolution sets TEM and its related techniques apart from PL and Raman spectroscopy in the characterization of TMD nanostructures.

In a transmission electron microscope, an electron beam is directed through a specimen, and information is gathered from the transmitted electron beam. Various operation modes are possible, each providing different information about the specimen [11]. For example, one can obtain information about the structure and composition at the atomic scale using a mode called scanning transmission electron microscopy (STEM). In this mode, the electron beam is focused to a small spot, which is subsequently scanned over the specimen. The images obtained from this operation mode show differences in intensity based on the atomic number of the atom at which is it focused. Therefore, creating an image that clearly displays differences between atoms within the atomic structure [11], thus providing information with excellent spatial resolution.

In addition to characterizing structural properties through STEM, a transmission electron microscope can be equipped with a multitude of spectrometers, enabling the probing of various properties. One TEM-related spectroscopy technique that is highly useful for characterizing novel materials is EELS, which stands for electron energy-loss spectroscopy. When electrons pass through the specimen, they lose energy to some degree due to scattering events. By mapping the energy-loss distribution of a specimen, EELS provides access to a wealth of information related to the structural, chemical, and local electronic properties of nanoscale materials. Here, the local electronic properties are contained within the low energy-loss range of the EEL spectra. This includes the excitonic signature and bandgap of the materials [12–17]. From the higher energy-loss range of the EEL spectra, instead, information regarding the chemical composition can be extracted [17, 18]. Combining the information obtained from both of these ranges enables the correlation of the optoelectronic properties and chemical composition of materials, as demonstrated by Tizei *et al.* [17] for heterogeneous layers of $MoS_{2(1\text{-}x)}Se_{2x}$.

Moreover, coupling this technique with STEM allows for the inspection of structural, chemical, and local electronic properties across entire large-scale specimens. Recent breakthroughs in instrumentation and data acquisition [19–21] have enabled state-of-the-art STEM-EELS analyses to study these properties with highly competitive spatial and spectral resolution. However, interpreting the spectra collected with this technique in the desired energy-loss region can be challenging. This underscores the need for theoretical modeling to assist in understanding the obtained data.

Besides being a powerful tool for characterizing nanomaterial properties, TEM has also demonstrated the capability to access information about strain fields within these materials. This characteristic is highly beneficial in the study of TMDs, as their properties have been found to change in the presence of strain. Hence, TEM-based techniques facilitate the investigation of the interrelationship between properties and strain fields.

Several TEM-based techniques are available for analyzing strain in 2D materials, including selected area diffraction (SAD) [22, 23], convergent beam electron diffraction (CBED) [24, 25], and geometric phase analysis (GPA) [26–29]. These electron diffraction based methods rely on diffraction contrast, making them challenging to implement for 2D layered materials. This due to the often weak diffraction signal produced by the thin layers of which they are composed. Therefore, specialized patterned probes would be required to accurately quantify the strain fields at nanoscale resolution using these methods [30, 31]. Moreover, GPA and related methods have a limited field-of-view, typically a few tens of nanometers, as they require atomic-resolution imaging. Consequently, these methods are unable to inspect strain fields over entire micron-sized nanostructures.

Alternatively, four-dimensional (4D) STEM has recently emerged as a promising technique for strain mapping in nanomaterials. This technique employs STEM in scanning nanobeam electron diffraction (NBED) mode to capture NBED patterns for each real-space scan position [32, 33]. This acquisition can be achieved by using STEM in conjunction with specialized detectors such as an electron microscope pixel array detector (EMPAD) [34]. Unlike conventional cameras, an EMPAD detector enables the capture of the entire unsaturated diffraction pattern at a high dynamic range and readout speed [34]. Using 4D STEM-EMPAD all conventional imaging metrics of STEM can be reproduced. However, the true potential of the EMPAD lies in fully utilizing the additional information contained within the scattering images it captures, such as for strain field capture [35, 36].

The 4D STEM-EMPAD approach results in a comprehensive 4D dataset, allowing for the extraction of variations in strain throughout the specimen through data processing. This approach is highly advantageous as it enables the mapping of strain in entire micron-sized specimens while preserving nanoscale resolution.

It is important to emphasize that interpreting both EELS and 4D STEM-EMPAD datasets requires comprehensive data analysis. In this chapter, we delve into two frameworks developed to assist in these analyses. First, we focus on the analysis of EELS spectral images. This analysis framework, called EELSFITTER, exploits machine learning to reveal interesting phenomenon within EEL spectra across specimens. Next, we highlight the STRAINMAPPER analysis framework, which allows the extraction of strain from 4D STEM-EMPAD datasets by building upon the existing exit-wave power cepstrum (EWPC) approach. In addition to providing an overview of the methodology behind these analysis frameworks, we also demonstrate their full functionality and workings through their application in case studies.

3.2. ANALYSIS OF EELS SPECTRAL IMAGES: EELSFITTER

As previously mentioned STEM-EELS provides access to a vast amount of information related to the properties of nanoscale materials. In this context, the information within the low energy-loss range ($\Delta E \lesssim 50$ eV) is of particular interest. This region contains crucial information regarding various features including plasmons, excitons, phonons, and inter- and intra-band transitions [37–40]. Therefore, the ability to chart the features within this region allows for the characterization of the local electronic properties.

However, the low-loss phenomena contained within this region risk being overshadowed by the so-called zero-loss peak (ZLP) [41]. As the name suggests, this intense and narrow peak contains all the contributions from electrons that either passed through the specimen without scattering or scattered elastically, thus experiencing no energy-loss. In the low-loss region, the EELS signal is largely dominated by the ZLP, yielding the need for a robust subtraction of the ZLP to chart and identify the features in the low-loss region. Adding to the challenge is the dependence of the magnitude and shape of the ZLP on multiple factors [42, 43], including various operational parameters of the TEM and the specimen itself.

Several approaches to ZLP subtraction exist [42, 44–52]. These methods often rely on specific model assumptions about the ZLP properties, especially concerning its parametric functional dependence on the electron energy-loss [39, 46, 47]. Alternatively, these methods may assume full symmetry around $\Delta E = 0$, allowing the mirroring of the $\Delta E < 0$ regime of the EEL spectra [48]. More recently, integrated software applications for background subtraction have also been utilized for ZLP subtraction [49–52]. However, these traditional methods come with some limitations and potential pitfalls. These include the need to specify an *ad hoc* parametric functional dependence, the absence of a detailed estimate of the associated uncertainties, and a certain degree of arbitrariness in the procedure induced by *ad hoc* choices such as those related to fitting ranges. Hence, there is a need for a ZLP subtraction method which bypasses these limitations of traditional approaches.

To address these challenges, an open-source analysis framework called EELSFITTER [53–55] was developed. This framework utilizes an approach developed in the context of high energy physics [56]. It combines artificial neural networks to provide an unbiased parametrization of the ZLP profile [57] with Monte Carlo sampling to yield a faithful uncertainty estimate [58].

In the following, we will discuss the methodology associated with the EELSFITTER framework. This methodology has previously been highlighted in works of Roest *et al.* [53], Brokkelkamp *et al.* [54] and van der Lippe *et al.* [55]. Along with a description of the methodology, we will present a case study to further demonstrate the functionalities of the EELSFITTER analysis framework.

3.2.1. PREPROCESSING METHODS: CLUSTERING AND NOISE REDUCTION

As already stated, the ZLP includes contributions from elastic scattering events, which arise from interactions with the atoms of the specimen. These scattering events are more likely to occur as the specimen's thickness increases. Hence, the ZLP is sensitive to the local thickness variations in the specimen. To train a deep-learning model that parameterizes the ZLP while accounting for these variations, the spectra in the spectral image must be grouped based on specimen thickness. To achieve this, the EELSFITTER framework employs the unsupervised machine learning method K-means clustering. Since determining the actual specimen thickness requires prior ZLP model training, the integrated intensity is instead used as a proxy for thickness.

Another factor to take into account in the analysis of the spectra in the spectral image is the signal-to-noise ratio. Recording the EELS spectral image at a higher spatial resolution is crucial for identifying and characterizing localized features within nanomaterials. However, this high spatial resolution can result in individual EEL spectra that are noisy. In such a case, it is advisable to improve the signal-to-noise ratio before training the deep-learning model. Two methods are available for this purpose. First, information from neighboring pixels can be combined using a technique known as pooling or sliding-window averaging [54]. This method was implemented in the earlier versions of EELSFITTER. Second, the data can be treated with principal component analysis (PCA) [59]. PCA has become the preferred method of denoising since its introduction in later versions of EELSFITTER. It is important to emphasize that in most cases, the untreated EEL spectra can be used to train the deep-learning model, and denoising methods are only implemented after training to assist in subsequent analyses.

3.2.2. THE NEURAL NETWORK AND MONTE CARLO REPLICA METHOD

Once the spectra in the spectral images are clustered and denoised (if required), the next step is to train a deep-learning model to parameterize the ZLP. To estimate and propagate uncertainties associated with the ZLP parametrization and subtraction procedure, the EELSFITTER framework adopts a variant of the Monte Carlo replica method [54]. The first step within this method is the generation of a large number of Monte Carlo "replicas". Each replica consists of a subset of spectra, specifically a randomly selected representative spectrum from each cluster, characterized by a different integrated intensity. The training of the deep-learning model is performed for each replica separately.

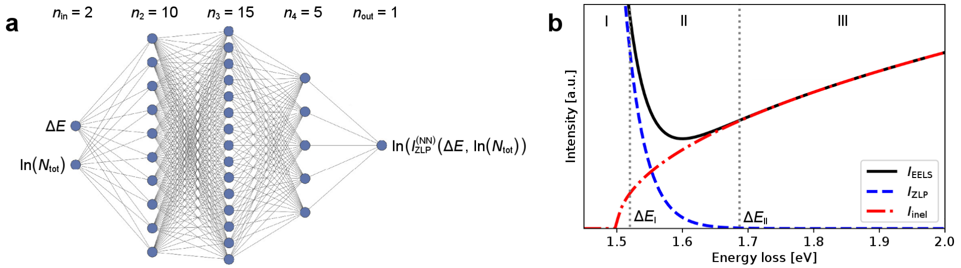

Figure 3.1: (a) The neural network architecture using for the parametrization of the ZLP. The input neurons are the energy-loss, ΔE, and the logarithm of the integrated intensity, $\ln(N_{tot})$, while the output is the model prediction for the ZLP intensity. Adapted from [54]. (b) A toy model for the EEL spectrum displaying the signal as is (I_{EELS}) as well as the contributions of the ZLP (I_{ZLP}) and inelastic scattering events (I_{inel}) separately. The EEL spectrum is divided into three regions for the training of the neural network, where the borders of the regions are given by the hyperparameters ΔE_I and ΔE_{II}. Adapted from [53].

For this purpose, a neural network is used, of which its architecture is shown in Figure 3.1a. The inputs to this neural network are the energy-loss, ΔE, and the logarithm of the integrated intensity, $\ln(N_{\mathrm{tot}})$. These input parameters are rescaled to lie between 0.1 and 0.9 before being fed to the neural network to improve the speed of the training process. Subsequently, the model parameters are determined by minimizing a cost function.

To train the neural network, each spectrum is divided into three regions, as shown in Figure 3.1b. In region I, the ZLP contribution dominates the total signal, so the model is trained to match the measured data in this region. In region II (at higher energy losses), where inelastic scattering becomes significant, the model is trained to ensure that the ZLP monotonically decreases. In region III, where the ZLP contributions are near-zero, the condition $I_{\mathrm{ZLP}}(\Delta E) \to 0$ is imposed on the model using the Lagrange multiplier method.

As seen in Figure 3.1b the regions are defined by two hyperparameters, ΔE_{I} and ΔE_{II}. These hyperparameters are automatically determined using the kneedle algorithm and the first local minimum [60]. Here, the hyperparameter ΔE_{I} is set at the kneedle location, which represents the point of highest curvature on the curve between the full width at half maximum (FWHM) of the ZLP and the first local minimum. In cases where the specimen's contribution to the signal doesn't exceed the noise floor and ZLP tail, ΔE_{I} is adjusted from the kneedle location through multiplication. ΔE_{II} is determined by fitting a log10 function through the kneedle location and the local minimum, and then identifying where it intersects with a single count.

Training the deep-learning model on all Monte Carlo replicas yields a Monte Carlo distribution of ZLP models, allowing for the subtraction of the ZLP from the recorded EEL spectra in each pixel of the spectral image. The use of the Monte Carlo replica method also provides a reliable estimation of errors without the need for approximations [58].

3.2.3. Bandgap Determination from the EELS Low-Loss Region

The ZLP subtraction from EEL spectra enables the extraction of information that was previously obscured by the ZLP. For example, ZLP subtraction facilitates the analysis of the bandgap energy and its characteristics. This is because the onset of inelastic scattering in an EELS signal provides valuable information about the bandgap energy, denoted as E_{BG}. Additionally, the shape of this onset, which depends on the underlying band structure, reveals the nature of the bandgap. To extract information about the bandgap, we recognize, as discussed by Rafferty *et al.* [40, 44], that the behavior of the subtracted inelastic EEL spectrum (I_{inel}) in the onset region can be modeled as:

$$I_{\mathrm{inel}}(\Delta E) \simeq A(\Delta E - E_{\mathrm{BG}})^{b}, \qquad \Delta E \geq E_{\mathrm{BG}} \tag{3.1}$$

While the value of I_{inel} vanishes for $\Delta E < E_{\mathrm{BG}}$. Here, A represents a normalization constant, and the exponent b conveys information about the nature of the bandgap. Specifically, for semiconductor materials with a direct bandgap, the exponent is expected to be $b \simeq 1/2$, while for an indirect bandgap, an exponent of approximately $b \simeq 3/2$ is anticipated.

The bandgap energy (E_{BG}), normalization constant (A), and the exponent (b) can be determined through a least-squares fit to the ZLP-subtracted spectra. This polynomial fit is conducted within a limited energy range, which must be carefully selected to ensure stable results. The use of the Monte Carlo replica method during ZLP parametrization training provides bandgap information with a reliable error estimate.

3.2.4. LOCAL THICKNESS DETERMINATION FROM EEL SPECTRA

Disentangling the ZLP and the inelastic scattering contribution in an EEL spectrum has various applications in addition to the bandgap analysis described prior. Within the EELSFITTER framework, one of these applications focuses on the determination of local thickness, while another involves the evaluation of the complex dielectric function, as demonstrated elsewhere [54].

Various methods are available to analyze the local thickness from EEL spectra, and two of them are implemented in the EELSFITTER framework. The first method is the Kramers-Kronig sum-rule method [45, 54]. In this method the refractive index, among other parameters, is used to determine the thickness. The alternative method is the log-ratio method [61]. This method relies on the mass-density to calculate thicknesses. The choice of the most accurate method depends on the specific recorded EELS data and is influenced by factors such as microscope configuration [62].

3.2.5. NATURALLY TWISTED WS_2 FLAKES: A CASE STUDY

To illustrate the capabilities of the EELSFITTER framework, we present a case study. For this case study we use the specimen shown in the annular dark-field (ADF) STEM image given in Figure 3.2a. This specimen, consisting of two slightly twisted triangular flakes of tungsten disulfide (WS_2), was synthesized by means of chemical vapor deposition (CVD) directly on a TEM microchip. Consequently, the specimen rests on a substrate composed of a 5 nm-thick silicon nitride (Si_3N_4) film that spans across this TEM microchip.

Figure 3.2b displays the spatially-resolved EELS map, also known as an EELS spectral image, acquired on the twisted flakes specimen. Each pixel within this map corresponds to the intensity of an individual EEL spectrum. Figure 3.2c shows one such EEL spectrum obtained from the base flake, here PCA was applied to improve the signal-to-noise ratio.

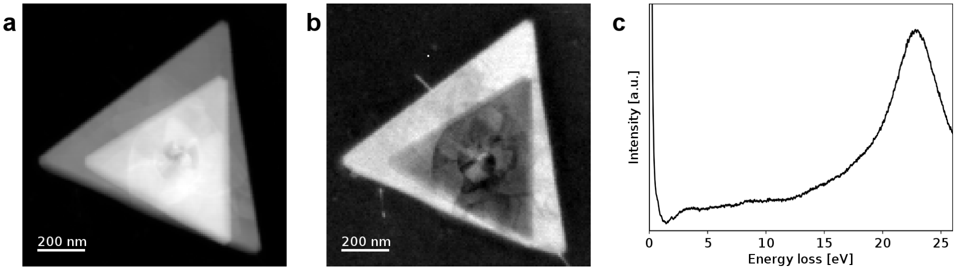

Figure 3.2: (a) Low-magnification ADF-STEM images of a WS_2 specimen consisting of a stack of two, slightly twisted, flakes. (b) Spatially-resolved EELS map of the specimen shown in (a), where each pixel corresponds to the intensity of an single EEL spectrum. (c) A representative EEL spectrum extracted from the base flake.

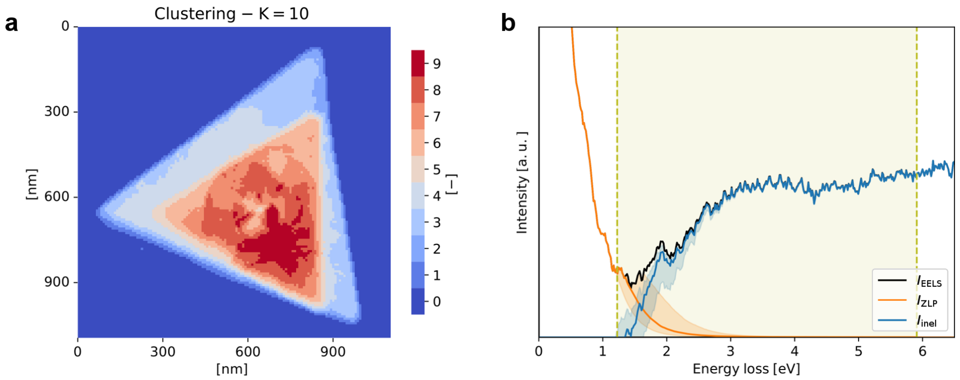

Figure 3.3: (a) The outcome of the K-means clustering procedure applied to the twisted flakes specimen. Here each color represents one of the K = 10 clusters. (b) The results of the ZLP parametrization in a single EEL spectrum, recorded in the base flake, displaying both the original (I_{EELS}) and subtracted inelastic (I_{inel}) EEL spectra as well as the modeled ZLP (I_{ZLP}). The bands indicate the 68% confidence level uncertainties associated to the ZLP model prediction and subtracted EEL spectrum. The shaded area indicates the region between the hyperparameters ΔE_{I} and ΔE_{II}.

CLUSTERING AND TRAINING

Before initializing the training of the deep-learning model to parameterize the ZLP, the EEL spectra contained in the EELS spectral image are subjected to clustering. The outcome of this clustering, which is based on the integrated intensity of the EEL spectra, is shown in Figure 3.3a. For this particular specimen, the optimal number of clusters was determined to be 10. In this clustering, cluster 0 contains all EEL spectra associated with the substrate, while remaining clusters house the EEL spectra of the specimen.

After clustering the spectra in the spectral image, the next step in the specimen analysis involves training the deep-learning model. Figure 3.3b provides a summary of the training results for a single EEL spectrum corresponding to the base flake. In this graph, both the original (I_{EELS}) and subtracted inelastic (I_{inel}) EEL spectra are plotted, along with the modeled ZLP (I_{ZLP}). The uncertainty bands indicate the 68% confidence level intervals associated to the ZLP model prediction and the subtracted EEL spectrum. The shaded area indicates the region between the hyperparameters ΔE_{I} and ΔE_{II}, where the contributions from inelastic scattering are masked by the ZLP before subtraction. Once again, it's important to emphasize that data denoising using PCA was performed only after training and was not required before the training process.

SPATIALLY-RESOLVED BANDGAP AND THICKNESS DETERMINATION

The separation of the ZLP and inelastic scattering contributions in the EEL spectra now allows for the analysis of the specimen's local electronic properties, specifically the bandgap and local thickness.

Figure 3.4 depicts the outcome of the bandgap analysis conducted on the twisted flakes specimen. For each EEL spectrum contained in the EELS spectral image, a polynomial fit is performed on the subtracted inelastic EEL spectrum using Equation 3.1. The shape of these spectra in the onset region indicated that the bandgap was indirect in nature.

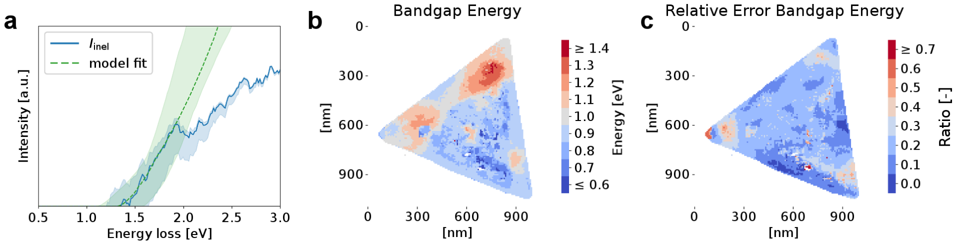

Figure 3.4: (a) The results of fitting Equation 3.1 to the onset of the subtracted inelastic EEL spectrum ($I_{\rm inel}$). Here the exponent b was set to a fixed value of $^3/_2$ due to the shape of the onset. The bands indicate the 68% confidence level uncertainties associated to the subtracted EEL spectrum and bandgap fit. (b) Spatially-resolved bandgap energy map corresponding to the twisted flakes specimen. (b) The relative uncertainties (68% confidence level intervals) associated to the bandgap energy map in (a). A mask has been applied to exclude substrate-only pixels and specimen pixels with a relative uncertainty exceeding 100%.

Consequently, the exponent b in Equation 3.1 was fixed at a value of $^3/_2$ for the evaluation of the twisted flakes specimen. The results of such a fit, along with the corresponding uncertainty bands, are displayed in Figure 3.4a for the EEL spectrum shown in Figure 3.3b.

Performing these fits across the entire specimen leads to the generation of maps as depicted in Figures 3.4b and 3.4c, which represent the bandgap energy and its corresponding uncertainty, respectively. In these maps, a mask has been applied to remove substrate-only pixels and specimen pixels with a relative uncertainty exceeding 100%. As illustrated in Figures 3.4b-c, the bandgap energy ranges from 0.7 to 1.3 eV, with associated uncertainties mostly below 20%, although a few areas exhibit increased uncertainties of up to 60%. Notably, the bandgap values extracted from the thicker region of the specimen, which includes the top flake, tend to be slightly lower compared to those from the base flake, though the difference is minimal.

Moving on to the analysis of local thickness, which results are shown in Figure 3.5a. This map provides information about the combined thickness of the specimen and underlying substrate, which in this case is the 5 nm-thick Si_3N_4 film. The accuracy of the local thickness map is demonstrated by its ability to accurately determine the thickness of the

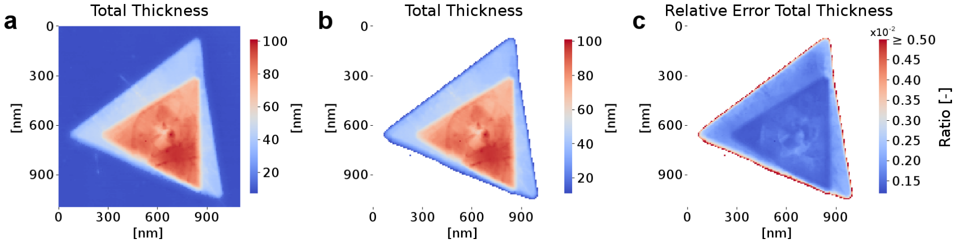

Figure 3.5: (a-b) Spatially-resolved map showing the combined thickness of the twisted flakes specimen and the underlying 5 nm-thick Si_3N_4 film substrate. (c) Relative errors of the thickness maps from (b). In (b-c) a mask is applied to exclude pixels corresponding to the substrate.

substrate. Figure 3.5b shows the same local thickness map with a mask applied to removed substrate-only pixels. This visualization allows for a clearer highlighting of variations in specimen thickness. While for a thick specimen the differences are minimal, it becomes particularly beneficial for thinner specimens. The corresponding map of relative uncertainty, displayed in Figure 3.5c, reveals negligible uncertainties well below 1%.

The local thickness analysis reveals that the base flake exhibits a maximum thickness of approximately 42 nm. With the addition of the top flake, the specimen reaches a maximum thickness of around 91 nm.

3.3. MAPPING STRAIN DISTRIBUTIONS WITH 4D STEM-EMPAD: STRAINMAPPER

As previously introduced, 4D STEM has emerged as a promising technique for strain mapping in nanoscale materials. In this approach, the utilization of an EMPAD detector plays a crucial role, as it allows for the capture of nanobeam electron diffraction (NBED) patterns for each real-space position. The resulting comprehensive 4D dataset enables the mapping of variations in strain throughout entire micron-sized specimens while preserving nanoscale resolution.

To extract the desired information from the 4D dataset, data processing is required. One conventional method for extracting strain information from the 4D dataset is tracking of the NBED diffraction disks [35, 63–65]. However, a challenge arises when applying this approach to complex nanostructures. The NBED patterns of these types of structures often contain contributions from different crystal structures, crystal orientations and materials. Disk tracking is often not equipped to disentangle these individual contributions. In addition, this technique does not account for the contribution of non-ideal sample tilt which is likely to be present when evaluation micron-sized specimen. While advanced techniques such as precession electron diffraction (PED) can counteract these contributions from non-ideal sample tilt, they require the use of specialized equipment and increase acquisition time [66, 67]. Hence, there is the need to develop data processing methods that overcome these limitations through an alternative route and enable strain evaluation in these more complex nanostructures.

To address this need, the open-source analysis framework STRAINMAPPER [68] was developed. This framework significantly enhances the capabilities of an existing approach to strain analyses based on 4D STEM, the exit-wave power cepstrum approach [36]. By incorporating advanced features such as the automated tracking of inter-atomic spacing peaks and the integration of clustering within the analysis framework, STRAINMAPPER enables the extraction of local intra-layer strain and rigid rotation (or deformation) angles from 4D NBED datasets even for the more complex micron-sized structures.

In the following, we will highlight the method by which STRAINMAPPER extracts the desired information from 4D NBED datasets, as previously explained by Bolhuis *et al.* [68]. To illustrate the implementation of the STRAINMAPPER framework, we will present the analysis of a twisted molybdenum-/tungsten diselenide ($MoSe_2$/WSe_2) heterostructure. This case study provides further details about the workings of the described method.

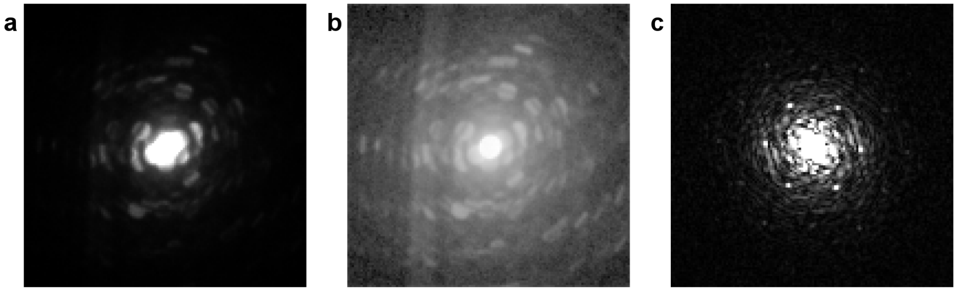

Figure 3.6: (a) A NBED pattern obtained from a twisted WS_2 specimen. This diffraction pattern serves as the starting point for generating the EWPC pattern. (b) The logarithm of the NBED pattern displayed in (b), the second step in generating the EWPC pattern. (c) The EWPC pattern generated by taking the FFT of (b). The visualization utilizes a capped linear scale, enhancing the visibility of the features within the pattern. Adapted from [69].

3.3.1. THE EXIT-WAVE POWER CEPSTRUM APPROACH

As mentioned earlier, the STRAINMAPPER framework builds upon an existing approach to strain analysis based on 4D STEM, namely the exit-wave power cepstrum (EWPC) approach. At the core of this approach lies the conversion of the NBED patterns, recorded by the EMPAD detector, into EWPC patterns. This conversion, developed by Padgett *et al.* [36], enables the isolation of the intensity contributions of the crystal lattice in the NBED pattern and filters out any contributions from non-ideal sample orientation. To visualize the EWPC approach, Figure 3.6 depicts the various steps within the conversion.

Figure 3.6a shows a single NBED pattern collected from a twisted WS_2 specimen. This NBED pattern serves as the starting point for generating the corresponding EWPC pattern. As a first step in this conversion, a logarithmic transformation is applied to the NBED pattern. This transformation results in the pattern shown in Figure 3.6b. Due to the transformation, the diffraction disks within the NBED pattern become apparent. This NBED pattern perfectly illustrates why disk tracking for complex nanostructures is challenging and emphasizes the need for alternative approaches.

Next, a fast Fourier transform (FFT) is employed to convert the logarithmic NBED pattern into the EWPC pattern depicted in Figure 3.6c. Despite the non-ideal tilt of the twisted WS_2 specimen, six sharp peaks (the inter-atomic spacing peaks) characteristic of TMD materials are clearly distinguishable within the EWPC pattern. In contrast, the short-range contributions of the non-ideal sample tilt are contained within the center of the EWPC pattern. As a result, these contributions do not affect the visibility of the inter-atomic spacing peaks. This is of great importance for the next steps in the STRAINMAPPER framework.

3.3.2. PEAK TRACKING AND CLUSTERING

The conversion of the NBED patterns to their respective EWPC patterns revealed the presence of inter-atomic spacing peaks. These peaks provide a reliable representation of the underlying structural information. By tracking the variations in the positions of these peaks across all EWPC patterns in a 4D dataset, local strain fields can be determined.

Therefore, the next step in the STRAINMAPPER analysis approach involves identifying the approximate location of the inter-atomic spacing peaks for each of the EWPC patterns in the acquired 4D dataset. This tracking of the peaks is performed using a difference of Gaussians (DoG) detection scheme [70]. To ensure the short-range contributions of the non-ideal sample tilt are disregarded during the peak detection, an annular mask can be used, limiting the region in which peak detection is performed.

Next, the peak positions identified by the DoG detection scheme in each EWPC pattern are superimposed to form a weighted point cloud. This weighted point cloud depicts all unique peak positions and their corresponding weights (number of occurrences). Subsequently, K-means clustering is used to group the unique peak positions into clusters that correspond to the inter-atomic spacing of the crystal lattice. All peak positions within the same cluster are assumed to correspond to the same feature in the EWPC pattern. Variations in the peak positions are attributed to shifts or rotations of this peak across the different EWPC patterns of the specimen. This part of the STRAINMAPPER analysis approach will be further elaborated in the case study discussed in Section 3.3.4.

As previously emphasized, the DoG detection scheme provides approximate peak positions of the inter-atomic spacing peaks with single-pixel accuracy. To achieve higher accuracy in mapping local strain fields, an essential step is to determine the precise peak position with sub-pixel accuracy. To accomplish this, the peak positions found by the DoG detection scheme are used as the centers of small circular masks (radius of a few pixels). These masks define the region in which the peak centers are expected. Subsequently, the sub-pixel maximum within this circular region is determined by calculating the center-of-mass (CoM) of the EWPC intensity. These sub-pixel maxima now provide precise peak positions within the EWPC patterns, enabling accurate mapping of the strain fields.

3.3.3. CALCULATION OF STRAIN FIELDS AND DEFORMATION ANGLES

To extract local strain and rigid rotation (or deformation) angles from the acquired 4D NBED dataset, it is sufficient to track the variations in the positions of just two inter-atomic spacing peaks. In other words, the calculations require the selection of two of the clusters determined in the previous step. These selected clusters must satisfy two rules: *1)* they have to be non-parallel, and *2)* they should belong to the same set of peaks in the EWPC pattern. For the latter it is important to remember that the NBED, and thus the EWPC pattern, can contain contributions from different crystal structures, crystal orientations, and materials. Each of these contributions will result in peaks within the EWPC pattern. It is crucial to disentangle these contributions to access information related to each structural elements separately. An example of this will be seen in the case study discussed in Section 3.3.4.

The precise peak positions, with sub-pixel accuracy, within the two selected clusters can now be used to evaluate the local strain and rigid rotation for each real-space scan position with respect to a chosen reference area. It is important to note that the peak positions can be described by vectors, where the origin of the coordinate system lies at the center of the EWPC pattern.

The first step in this evaluation involves constructing a deformation matrix **D**. This method is commonly used in GPA for finite displacements [71]. The deformation matrix **D** can be calculated, depending on the preferred coordinate system, as:

$$\mathbf{D_{car}} = \mathbf{A}\mathbf{A_0}^{-1} \quad \text{or} \quad \mathbf{D_{vec}} = \mathbf{A_0}^{-1}\mathbf{A} \tag{3.2}$$

In this context, the matrix **A** comprises the vectors associated with the peak positions found in the specific EWPC pattern being evaluated, while the matrix $\mathbf{A_0}$ comprises the vectors associated with the peak positions found within the chosen reference area. The coordinate system in which the deformation matrix is described is denoted by the subscript. The deformation matrix $\mathbf{D_{car}}$ describes the deformation using the Cartesian coordinate system as a basis, while the deformation matrix $\mathbf{D_{vec}}$ describes the deformation in the basis of the vectors associated with the peak positions in the reference area. The choice of which coordinate system to use depends on the specific requirements of the analysis.

The deformation matrix **D** contains information regarding both the relative local strain fields and the rigid rotation. By performing a polar decomposition of the deformation matrix **D**, this information can be separated. The final result gives us the strain matrix **E** containing the strain components along the x- and y-directions, as well as the xy component (shear strain), and the rigid rotation matrix, allowing for the determination of the rigid rotation (or deformation) angle. Since this calculation is performed for each real-space scan position, one can generate maps for each strain component as well as the rigid rotation (or deformation) angle, showcasing their variations across the inspected specimen.

DIFFERENCES BETWEEN TWIST AND THE RIGID ROTATION (DEFORMATION) ANGLE

It is important to emphasize that the rigid rotation (or deformation) angle is generally different from a twist (global rotation) angle between two adjacent layers. To clarify the relationship between the rigid rotation (or deformation) angle θ and the twist (or global rotation) angle, the schematic in Figure 3.7 highlights their differences and similarities.

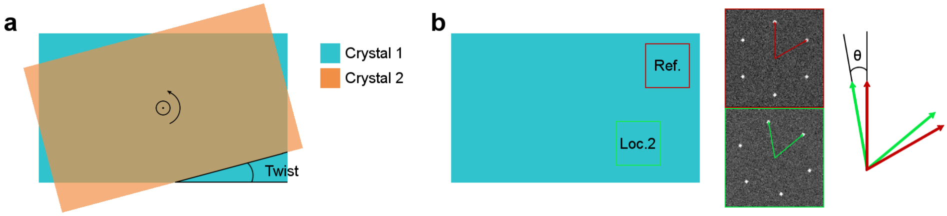

Figure 3.7: Schematic representations to highlight the relationship between (a) a global rotation (twist) between adjacent layers/crystals, and (b) the rigid rotation (or deformation) angle θ which characterizes a rotation deformation within the crystal structure with respect to a fixed reference. The latter is determined from pairs of non-collinear vectors in the EWPC pattern. Adapted from [69].

First, a twist (or global rotation) refers to an overall change in orientation between two adjacent layers (or crystals) when all other parameters of the crystal lattice remain unchanged. In other words, it represents the macroscopic (mis)alignment of one layer (or crystal) relative to another, as depicted in Figure 3.7a. Hence, a twist angle dictates the relative positioning of adjacent layers within a heterostructure or multi-layer system.

On the other hand, the rigid rotation (or deformation) angle (θ) is a measure of the rotation deformation within the crystal structure with respect to a fixed reference. It is determined from pairs of non-collinear vectors in the EWPC pattern, as exemplified in Figure 3.7b, where these vectors are indicated within an EWPC pattern obtained at a measurement location (green) and the fixed reference (red). The angle by which the measurement EWPC vectors are rotated with respect to those in the reference EWPC is what is denoted as the rigid rotation or deformation angle θ. Unlike the twist (global rotation) angle, which is macroscopic, the rigid rotation (deformation) angle is modulated with nanoscale variations across a specimen.

3.3.4. TWISTED $MoSe_2/WSe_2$ HETEROSTRUCTURES: A CASE STUDY

To further illustrate the capabilities of the STRAINMAPPER analysis framework and its potential for strain analysis in 2D (TMD) materials, we present a case study. In this case study, the local strain fields and deformation angle within a twisted $MoSe_2/WSe_2$ heterostructures are evaluated. This twisted heterostructure is created by stamping flakes of $MoSe_2$ and WSe_2 on top of each other at an angle of approximately 15° (as measured from the FFT shown in Figure 3.8c).

Figure 3.8a shows an ADF-STEM image of the specimen. The area depicted contains an interface between a single flake and a heterostructure region. A high-resolution STEM analysis of the heterostructure region within the specimen (Figure 3.8b) reveals the presence of a Moiré pattern, indicating the twisted nature of the two flakes within the heterostructure. The corresponding FFT is shown in Figure 3.8c. Two distinct diffraction patterns can be observed, providing further confirmation of the twisted nature of the heterostructure.

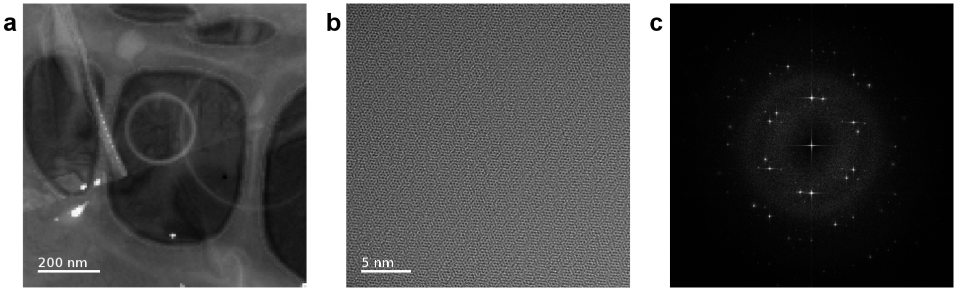

Figure 3.8: (a) ADF-STEM image of a twisted $MoSe_2/WSe_2$ heterostructure obtained from the 4D STEM-EMPAD dataset. The area shown contains an interface between a single flake region (bottom) and a heterostructure region (top). Representative (b) high-angle annular dark-field (HAADF) STEM image acquired on the heterostructure, and (c) the corresponding FFT. Adapted from [69].

Peak Tracking and Clustering

Figure 3.9a shows the ADF-STEM image highlighting the region within the twisted $MoSe_2/WSe_2$ heterostructure that is to be analyzed. In this image, the individual flakes are marked in blue and orange. The nanobeam diffraction map obtained at the red dot in Figure 3.9a was transformed into the EWPC pattern shown in Figure 3.9b. In this specific pattern, twelve peaks were identified. Six of these peaks correspond to the bottom flake (blue), while the other six peaks correspond to the top flake (orange). This EWPC pattern showcases a clear example of an EWPC pattern which contains contributions from different TMD flakes that are not perfectly aligned on the atomic scale.

Next, the positions of the inter-atomic spacing peaks observed in the EWPC pattern are determined. A visual representation of the workings of the DoG peak detection algorithm is shown in Figure 3.9c. The peak detection algorithm is carried out within the region dictated by the annular mask (blue), yielding the peak positions (red dots) with single-pixel accuracy. By performing this peak detection in each EWPC pattern, and superimposing the results, the weighted point cloud shown in Figure 3.9d is generated. Herein, each spot corresponds to a unique peak position and its color reveals the number of occurrences for that specific peak position.

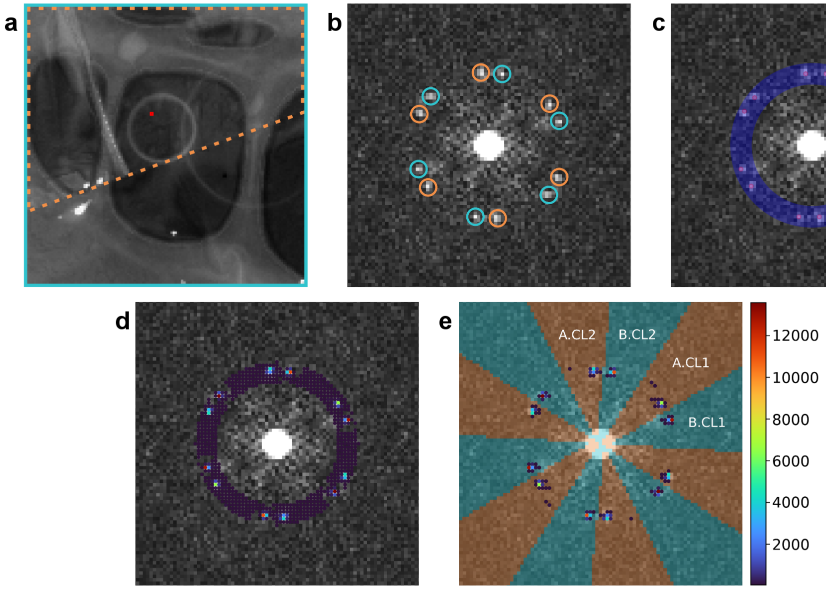

Figure 3.9: (a) ADF-STEM image as also shown in Figure 3.8a, where the two flakes that make up the heterostructure are outlined in blue (solid) and orange (dashed). (b) EWPC pattern extracted at the red pixel in (a). A linear capped scale is used to enhance the visibility of the inter-atomic spacing peaks. (c) Visual representation of the DoG peak detection for a single EWPC pattern. The annular mask dictates the area in which peak detection is performed, and the red dots show the determined peak positions. (d-e) Weighted point cloud representations displaying all uniquely tracked peak positions (spots) along with their corresponding weights (color) (d) before applying a threshold and (e) after applying a threshold (≤ 50). The colored divisions in (e) represent clustering of the point cloud. The origin of the peaks within each cluster is illustrated by their color. The blue clusters correspond to peaks from the bottom flake (outlined in blue in (a)), while the orange clusters correspond to peaks from the top flake (outlined in orange in (a)). Adapted from [69].

Figure 3.9d reveals that some peak positions appear with a high frequency across the EWPC patterns contained in the 4D dataset, forming hotspots in the weighted point cloud. The remaining spots in the weighted point cloud are found to correspond to peak positions appearing only a few times and can likely be attributed to erroneously tracked peaks. To improve the quality of the strain and deformation angle maps, it is necessary to remove these erroneously tracked peaks. To this end, a threshold filter is applied that eliminates all low-frequency spots. For the twisted $MoSe_2/WSe_2$ heterostructure the threshold is set to a value of 50, resulting in the removal of all peak positions that appear less than 50 times across all EWPC patterns.

The filtered weighted point cloud resulting from the application of this threshold filter is given in Figure 3.9e. The remaining peak positions are group into twelve clusters, depicted by the colored divisions. Similarly to the individual EWPC pattern, the origin of the peak positions within the clusters are presented by the color of the divisions. With six clusters corresponding to the bottom flake (blue) and top flake (orange) each.

THRESHOLD APPLICATION FOR IMPROVED STRAIN AND DEFORMATION ANGLE MAPS

To showcase the effectiveness of the threshold filter, we investigate the peak positions that were removed as a result of its application. Figure 3.10a shows the collection of all peak positions falling within the threshold range (≤ 50). The clustering is kept consistent with that shown in Figure 3.9e, where two non-parallel clusters associated with the top flake (orange) have been labeled as A.CL1 and A.CL2.

Figures 3.10b and 3.10c display the local x-coordinates associated with each peak position found in cluster 1 (A.CL1) and cluster 2 (A.CL2), respectively. These maps illustrate which pixels were removed due to the threshold application. The majority of eliminated pixels are located outside the region covered by the top flake. In these pixels, the EWPC pattern should contain a singular set of six peaks, arranged in a hexagonal pattern, associated to the bottom flake. Any additional peaks tracked within these pixels that are attributed to the top flake are false positives, and their removal is justified. However, it is evident that the eliminated pixels are not limited to this region; some pixels associated

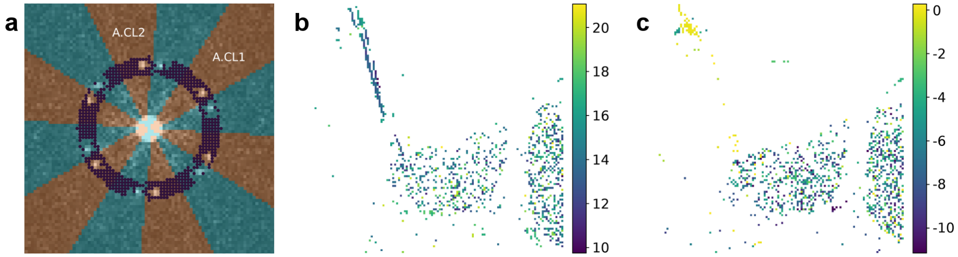

Figure 3.10: (a) Filtered point cloud revealing all tracked peak positions (spots) with a weight below 50. This illustrates the spots that are filtered out when applying the threshold to obtain the filtered weighted point cloud as shown in Figure 3.9d. The colored divisions correspond to the same clustering shown in Figure 3.9e. (b-c) Spatially-resolved maps of the x-coordinates associated with each peak position found within (b) cluster 1 (A.CL1) and (c) cluster 2 (A.CL2) as indicated in (a). These maps illustrate the pixels that were removed after applying the threshold.

with the top flake are also removed. These pixels predominantly contain erroneously tracked peaks. It is worth noting that in the process of determining the optimal threshold for eliminating erroneously tracked peak positions within EWPC patterns, the removal of some specimen-specific pixels is inevitable.

MAPPING OF THE STRAIN FIELDS AND DEFORMATION ANGLE

In order to determine the local strain and rigid rotation within the twisted $MoSe_2/WSe_2$ heterostructure, two decisions must be made. First, a reference area needs to be assigned, which will serve as the baseline for evaluating the relative strain fields and rigid rotation. In this case, the reference area was intentionally selected to encompass a region within the inspected area that contains all twelve spots in the EWPC pattern (thus containing both flakes) and lies over the vacuum.

Second, two non-parallel clusters must be chosen. As previously discussed, these non-parallel clusters should belong to the same set of EWPC peaks as to provide information about the same structural element. Due to the nature of the twisted $MoSe_2/WSe_2$ heterostructure, two structural elements are present; the individual flakes. Consequently, to analyze the strain and rigid rotation in the twisted $MoSe_2/WSe_2$ heterostructure, calculations needs to be performed separately for each flake. The clusters selected for the two-set analysis are indicated in Figure 3.9e and are labeled as cluster set A and cluster set B, representing the top and bottom flakes, respectively. The vectors associated with the peak positions in these chosen clusters serve as the basis for the resulting maps of strain and rigid rotation.

The spatially-resolved strain fields (ε_{xx}, ε_{yy}, and ε_{xy}) obtained from cluster set A, corresponding to vectors along the x and y directions, are presented in Figures 3.11a-c. The corresponding spatially-resolved map of the deformation angle (θ) is presented in Figure 3.11g. The strain maps obtained from cluster set B, corresponding to vectors along the x' and y' directions, are presented in Figures 3.11d-f, with the corresponding deformation angle map shown in Figure 3.11h. To enhance visualization and reduce pixelation artifacts and outliers, a Gaussian filter was applied to smoothen these maps. It is evident that for some real-space scan positions, empty pixels appear in the strain and deformation angle maps, indicating that one of the two selected peaks was either untracked or inaccurately tracked.

The strain maps reveal that the flakes within this specimen experience some strain (Figures 3.11a-f) relative to the reference area. This strain is mainly located at the edges of the holes within the lacey carbon film that supports the flakes. The transition between lying on the carbon support and being spanned over the vacuum could contribute to this observed strain. Additionally, the fold within the top flake is an area of interest in the strain maps also.

The spatially-resolved deformation angle map obtained for the bottom flake (Figure 3.11h) indicates that only moderate amounts of rigid rotation with respect to the reference are present. In contrast, a relative deformation angle of 2° can be observed in the top flake between the right side of the fold (where the reference is chosen) and the left side of the fold (Figure 3.11g).

In addition to the deformation angle θ, the twist (global rotation) angle can also be extracted using the STRAINMAPPER framework for this twisted $MoSe_2/WSe_2$ heterostructure. This is done by selecting clusters A.CL2 and B.CL2 denoted in Figure 3.9e and determining the angle between the EWPC peaks for each EWPC pattern, yielding the results shown in Figure 3.11i. This analysis is possible only in the heterostructure region of the specimen, where the peaks in cluster A.CL2 and B.CL2 are both present.

From this twist angle mapping, it can be seen that the two flakes have a twist angle of approximately 15° (13°) between them on the right (left) side of the fold, respectively. The 15° twist angle is consistent with the angle measured from the FFT in Figure 3.8c, while the 13° results from a slight twist of the top flake due to its folding.

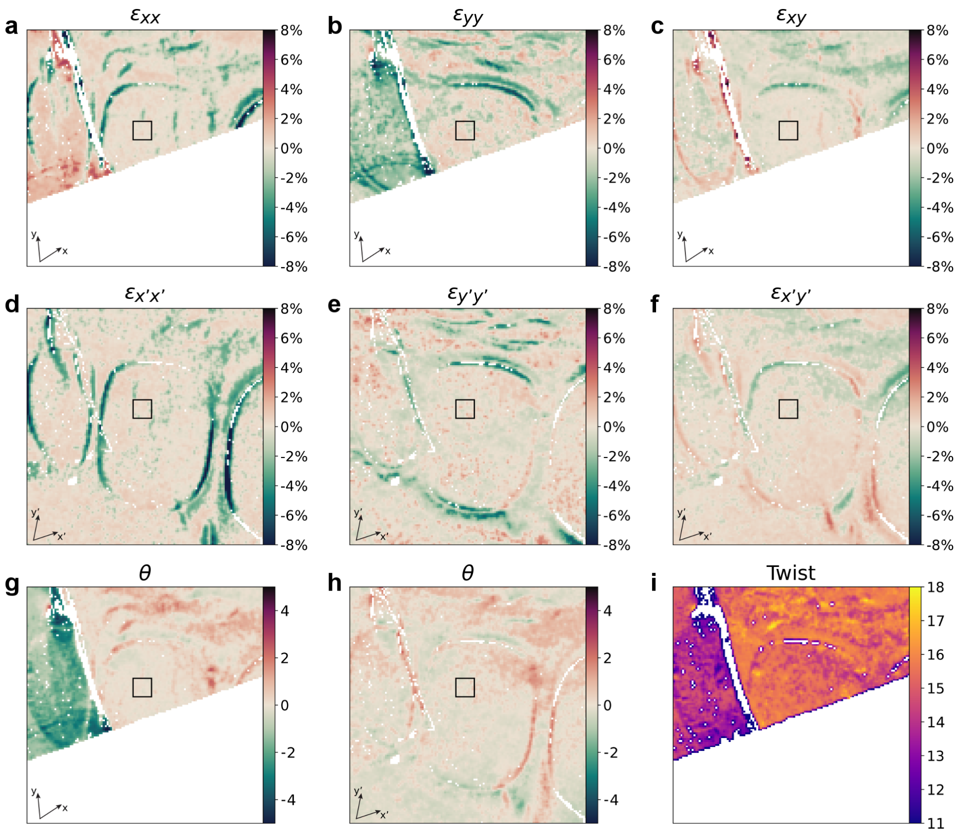

Figure 3.11: Spatially-resolved (a-f) strain (ε_{xx}, ε_{yy}, and ε_{xy}) and (g-h) deformation angle θ obtained using the marked clusters in Figure 3.9e denoted by (a-c),(g) A and (d-f),(h) B. The reference area is indicated by the black square in (a-h). All maps were subjected to a Gaussian filter to smooth out the outliers. (i) The spatially-resolved map of the twist angle between the $MoSe_2$ and WSe_2 flakes of the heterostructure. Adapted from [69].

REFERENCES

[1] Z. Wu, W. Zhao, J. Jiang, T. Zheng, Y. You, J. Lu, and Z. Ni, *Defect Activated Photoluminescence in* WSe_2 *Monolayer,* The Journal of Physical Chemistry C **121**, 12294 (2017).

[2] P. K. Chow, R. B. Jacobs-Gedrim, J. Gao, T.-M. Lu, B. Yu, H. Terrones, and N. Koratkar, *Defect-Induced Photoluminescence in Monolayer Semiconducting Transition Metal Dichalcogenides,* ACS Nano **9**, 1520 (2015).

[3] G. Eda, H. Yamaguchi, D. Voiry, T. Fujita, M. Chen, and M. Chhowalla, *Photoluminescence from Chemically Exfoliated* MoS_2*,* Nano Letters **11**, 5111 (2011).

[4] A. Splendiani, L. Sun, Y. Zhang, T. Li, J. Kim, C.-Y. Chim, G. Galli, and F. Wang, *Emerging Photoluminescence in Monolayer* MoS_2*,* Nano Letters **10**, 1271 (2010).

[5] H. R. Gutiérrez, N. Perea-López, A. L. Elías, A. Berkdemir, B. Wang, R. Lv, F. López-Urías, V. H. Crespi, H. Terrones, and M. Terrones, *Extraordinary Room-Temperature Photoluminescence in Triangular* WS_2 *Monolayers,* Nano Letters **13**, 3447 (2013).

[6] C. R. Zhu, G. Wang, B. L. Liu, X. Marie, X. F. Qiao, X. Zhang, X. X. Wu, H. Fan, P. H. Tan, T. Amand, and B. Urbaszek, *Strain tuning of optical emission energy and polarization in monolayer and bilayer* MoS_2*,* Physical Review B **88**, 121301 (2013).

[7] A. Berkdemir, H. R. Gutiérrez, A. R. Botello-Méndez, N. Perea-López, A. L. Elías, C.-I. Chia, B. Wang, V. H. Crespi, F. López-Urías, J.-C. Charlier, H. Terrones, and M. Terrones, *Identification of individual and few layers of* WS_2 *using Raman Spectroscopy,* Scientific Reports **3**, 1755 (2013).

[8] M. O'Brien, N. McEvoy, D. Hanlon, T. Hallam, J. N. Coleman, and G. S. Duesberg, *Mapping of Low-Frequency Raman Modes in CVD-Grown Transition Metal Dichalcogenides: Layer Number, Stacking Orientation and Resonant Effects,* Scientific Reports **6**, 19476 (2016).

[9] J.-U. Lee, K. Kim, S. Han, G. H. Ryu, Z. Lee, and H. Cheong, *Raman Signatures of Polytypism in Molybdenum Disulfide,* ACS Nano **10**, 1948 (2016).

[10] X. H. Wang, C. C. Zheng, and J. Q. Ning, *Influence of curvature strain and Van der Waals force on the inter-layer vibration mode of* WS_2 *nanotubes: A confocal micro-Raman spectroscopic study,* Scientific Reports **6**, 33091 (2016).

[11] D. B. Williams and C. B. Carter, *Transmission Electron Microscopy: A Textbook for Materials Science*, 2nd ed. (Springer, New York, NY, 2009).

[12] X. Hu, P. Yasaei, J. R. Jokissari, S. Ogut, A. Salehi, and R. F. Klie, *Nanoscale Thermometry for 2D Materials,* Microscopy and Microanalysis **23**, 1724 (2017).

[13] M. D. Kapetanakis, W. Zhou, M. P. Oxley, J. Lee, M. P. Prange, S. J. Pennycook, J. C. Idrobo, and S. T. Pantelides, *Low-loss electron energy loss spectroscopy: An atomic-resolution complement to optical spectroscopies and application to graphene,* Physical Review B **92**, 125147 (2015).

[14] S. Susarla, L. H. G. Tizei, S. Y. Woo, A. Zobelli, O. Stephan, and P. M. Ajayan, *Low Loss EELS of Lateral MoS_2/WS_2 Heterostructures,* Microscopy and Microanalysis **25**, 640 (2019).

[15] M. Pelaez-Fernandez, Y. Lin, K. Suenaga, and R. Arenal, *Low-Loss EELS Investigations on Atomically Thin $Mo_xW_{(1\text{-}x)}S_2$ Nanoflakes for Delving into Their Optoelectronic Properties,* Microscopy and Microanalysis **24**, 1576 (2018).

[16] M. Bar Sadan, M. Heidelmann, L. Houben, and R. Tenne, *Inorganic WS_2 nanotubes revealed atom by atom using ultra-high-resolution transmission electron microscopy,* Applied Physics A **96**, 343 (2009).

[17] L. H. G. Tizei, Y.-C. Lin, M. Mukai, H. Sawada, A.-Y. Lu, L.-J. Li, K. Kimoto, and K. Suenaga, *Exciton Mapping at Subwavelength Scales in Two-Dimensional Materials,* Physical Review Letters **114**, 107601 (2015).

[18] H. Kim, V. Kanade, M. Kim, K. S. Kim, B. An, H. Seok, H. Yoo, L. E. Chaney, S. Kim, C. Yang, G. Y. Yeom, D. Whang, J. Lee, and T. Kim, *Wafer-Scale and Low-Temperature Growth of 1T-WS_2 Film for Efficient and Stable Hydrogen Evolution Reaction,* Small **16**, 1905000 (2020).

[19] M. Terauchi, M. Tanaka, K. Tsuno, and M. Ishida, *Development of a high energy resolution electron energy-loss spectroscopy microscope,* Journal of Microscopy **194**, 203 (1999).

[20] B. Freitag, S. Kujawa, P. M. Mul, J. Ringnalda, and P. C. Tiemeijer, *Breaking the spherical and chromatic aberration barrier in transmission electron microscopy,* Ultramicroscopy **102**, 209 – 214 (2005).

[21] M. Haider, S. Uhlemann, E. Schwan, G. Rose, B. Kabius, and K. Urban, *Electron microscopy image enhanced,* Nature **392**, 768 – 769 (1998).

[22] H.-J. Kim, H. Kim, S. Yang, and J.-Y. Kwon, *Grains in Selectively Grown MoS_2 Thin Films,* Small **13**, 1702256 (2017).

[23] F. Uesugi, *Strain mapping in selected area electron diffraction method combining a Cs-corrected TEM with a stage scanning system,* Ultramicroscopy **135**, 80 (2013).

[24] P. M. Jones, G. M. Rackham, J. W. Steeds, and F. C. Frank, *Higher order Laue zone effects in electron diffraction and their use in lattice parameter determination,* Proceedings of the Royal Society of London. A. Mathematical and Physical Sciences **354**, 197 (1977).

[25] S. J. Rozeveld and J. M. Howe, *Determination of multiple lattice parameters from convergent-beam electron diffraction patterns,* Ultramicroscopy **50**, 41 (1993).

[26] M. J. Hÿtch, E. Snoeck, and R. Kilaas, *Quantitative measurement of displacement and strain fields from HREM micrographs,* Ultramicroscopy **74**, 131 (1998).

[27] M. Tinoco, L. Maduro, M. Masaki, E. Okunishi, and S. Conesa-Boj, *Strain-Dependent Edge Structures in* MoS_2 *Layers,* Nano Letters **17**, 7021 (2017).

[28] M. de la Mata, C. Magén, P. Caroff, and J. Arbiol, *Atomic Scale Strain Relaxation in Axial Semiconductor III–V Nanowire Heterostructures,* Nano Letters **14**, 6614 (2014).

[29] R. Bierwolf, M. Hohenstein, F. Phillipp, O. Brandt, G. E. Crook, and K. Ploog, *Direct measurement of local lattice distortions in strained layer structures by HREM,* Ultramicroscopy **49**, 273 (1993).

[30] S. E. Zeltmann, A. Müller, K. C. Bustillo, B. Savitzky, L. Hughes, A. M. Minor, and C. Ophus, *Patterned probes for high precision 4D-STEM bragg measurements,* Ultramicroscopy **209**, 112890 (2020).

[31] A. Londoño-Calderon, R. Dhall, C. Ophus, M. Schneider, Y. Wang, E. Dervishi, H. S. Kang, C.-H. Lee, J. Yoo, and M. T. Pettes, *Visualizing Grain Statistics in MOCVD* WSe_2 *through Four-Dimensional Scanning Transmission Electron Microscopy,* Nano Letters **22**, 2578 (2022).

[32] V. B. Ozdol, C. Gammer, X. G. Jin, P. Ercius, C. Ophus, J. Ciston, and A. M. Minor, *Strain mapping at nanometer resolution using advanced nano-beam electron diffraction,* Applied Physics Letters **106**, 253107 (2015).

[33] Y. Han, K. Nguyen, M. Cao, P. Cueva, S. Xie, M. W. Tate, P. Purohit, S. M. Gruner, J. Park, and D. A. Muller, *Strain Mapping of Two-Dimensional Heterostructures with Subpicometer Precision,* Nano Letters **18**, 3746 (2018).

[34] M. W. Tate, P. Purohit, D. Chamberlain, K. X. Nguyen, R. Hovden, C. S. Chang, P. Deb, E. Turgut, J. T. Heron, D. G. Schlom, D. C. Ralph, G. D. Fuchs, K. S. Shanks, H. T. Philipp, D. A. Muller, and S. M. Gruner, *High Dynamic Range Pixel Array Detector for Scanning Transmission Electron Microscopy,* Microscopy and Microanalysis **22**, 237 (2016).

[35] Y. Jiang, Z. Chen, Y. Han, P. Deb, H. Gao, S. Xie, P. Purohit, M. W. Tate, J. Park, S. M. Gruner, *et al.*, *Electron ptychography of 2D materials to deep sub-ångström resolution,* Nature **559**, 343 (2018).

[36] E. Padgett, M. E. Holtz, P. Cueva, Y.-T. Shao, E. Langenberg, D. G. Schlom, and D. A. Muller, *The exit-wave power-cepstrum transform for scanning nanobeam electron diffraction: robust strain mapping at subnanometer resolution and subpicometer precision,* Ultramicroscopy **214**, 112994 (2020).

[37] J. Geiger, *Inelastic Electron Scattering in Thin Films at Oblique Incidence,* Physica Status Solidi (b) **24**, 457 (1967).

[38] B. Schaffer, K. Riegler, G. Kothleitner, W. Grogger, and F. Hofer, *Monochromated, spatially resolved electron energy-loss spectroscopic measurements of gold nanoparticles in the plasmon range,* Micron **40**, 269 (2009).

[39] R. Erni, N. D. Browning, Z. R. Dai, and J. P. Bradley, *Analysis of extraterrestrial particles using monochromated electron energy-loss spectroscopy,* Micron **36**, 369 (2005).

[40] B. Rafferty and L. M. Brown, *Direct and indirect transitions in the region of the band gap using electron-energy-loss spectroscopy,* Physical Review B **58**, 10326 (1998).

[41] F. J. García de Abajo, *Optical excitations in electron microscopy,* Reviews of Modern Physics **82**, 209 (2010).

[42] M. Stöger-Pollach, *Optical properties and bandgaps from low loss EELS: Pitfalls and solutions,* Micron **39**, 1092 (2008).

[43] J. Park, S. Heo, J.-G. Chung, H. Kim, H. Lee, K. Kim, and G.-S. Park, *Bandgap measurement of thin dielectric films using monochromated STEM-EELS,* Ultramicroscopy **109**, 1183 (2009).

[44] B. Rafferty, S. J. Pennycook, and L. M. Brown, *Zero loss peak deconvolution for bandgap EEL spectra,* Journal of Electron Microscopy **49**, 517 (2000).

[45] R. F. Egerton, *Electron Energy-Loss Spectroscopy in the Electron Microscope* (Plenum Press, New York, NY, 1996).

[46] A. D. Dorneich, R. H. French, H. Müllejans, S. Loughin, and M. Rühle, *Quantitative analysis of valence electron energy-loss spectra of aluminium nitride,* Journal of Microscopy **191**, 286 (1998).

[47] K. van Benthem, C. Elsässer, and R. H. French, *Bulk electronic structure of* $SrTiO_3$*: Experiment and theory,* Journal of Applied Physics **90**, 6156–6164 (2001).

[48] S. Lazar, G. A. Botton, M.-Y. Wu, F. D. Tichelaar, and H. W. Zandbergen, *Materials science applications of HREELS in near edgestructure analysis an low-energy loss spectroscopy,* Ultramicroscopy **96**, 535 (2003).

[49] R. Egerton and M. Malac, *Improved background-fitting algorithms for ionization edges in electron energy-loss spectra,* Ultramicroscopy **92**, 47 (2002).

[50] J. T. Held, H. Yun, and K. A. Mkhoyan, *Simultaneous multi-region background subtraction for core-level EEL spectra,* Ultramicroscopy **210**, 112919 (2020).

[51] C. S. Granerød, W. Zhan, and Ø. Prytz, *Automated approaches for band gap mapping in STEM-EELS,* Ultramicroscopy **184**, 39 (2018).

[52] K. L. Y. Fung, M. W. Fay, S. M. Collins, D. M. Kepaptsoglou, S. T. Skowron, Q. M. Ramasse, and A. N. Khlobystov, *Accurate EELS background subtraction – an adaptable method in MATLAB,* Ultramicroscopy **217**, 113052 (2020).

[53] L. I. Roest, S. E. van Heijst, L. Maduro, J. Rojo, and S. Conesa-Boj, *Charting the low-loss region in electron energy loss spectroscopy with machine learning,* Ultramicroscopy **222**, 113202 (2021).

[54] A. Brokkelkamp, J. ter Hoeve, I. Postmes, S. E. van Heijst, L. Maduro, A. V. Davydov, S. Krylyuk, J. Rojo, and S. Conesa-Boj, *Spatially Resolved Band Gap and Dielectric Function in Two-Dimensional Materials from Electron Energy Loss Spectroscopy,* The Journal of Physical Chemistry A **126**, 1255 (2022).

[55] S. van der Lippe, A. Brokkelkamp, J. Rojo, and S. Conesa-Boj, *Localized Exciton Anatomy and BandGap Energy Modulation in 1D MoS_2 Nanostructures,* Advanced Functional Materials **33**, 2307610 (2023).

[56] R. D. Ball, L. Del Debbio, S. Forte, A. Guffanti, J. I. Latorre, A. Piccione, J. Rojo, and M. Ubiali, *A determination of parton distributions with faithful uncertainty estimation,* Nuclear Physics B **809**, 1 (2009).

[57] R. D. Ball, S. Carrazza, J. Cruz-Martinez, L. Del Debbio, S. Forte, T. Giani, S. Iranipour, Z. Kassabov, J. I. Latorre, E. R. Nocera, R. L. Pearson, J. Rojo, R. Stegeman, C. Schwan, M. Ubiali, C. Voisey, and M. Wilson, *The path to proton structure at 1% accuracy,* The European Physical Journal C **82**, 428 (2022).

[58] A. Candido, A. Garcia, G. Magni, T. Rabemananjara, J. Rojo, and R. Stegeman, *Neutrino structure functions from GeV to EeV energies,* Journal of High Energy Physics **2023**, 149 (2023).

[59] G. Lucas, P. Burdet, M. Cantoni, and C. Hébert, *Multivariate statistical analysis as a tool for the segmentation of 3D spectral data,* Micron **52-53**, 49 (2013).

[60] V. Satopaa, J. Albrecht, D. Irwin, and B. Raghavan, *Finding a "Kneedle" in a Haystack: Detecting Knee Points in System Behavior,* in *2011 31st International Conference on Distributed Computing Systems Workshops* (2011) pp. 166–171.

[61] K. Iakoubovskii, K. Mitsuishi, Y. Nakayama, and K. Furuya, *Thickness measurements with electron energy loss spectroscopy,* Microscopy Research and Technique **71**, 626 (2008).

[62] H.-R. Zhang, R. F. Egerton, and M. Malac, *Local thickness measurement through scattering contrast and electron energy-loss spectroscopy,* Micron **43**, 8 (2012).

[63] T. C. Pekin, C. Gammer, J. Ciston, A. M. Minor, and C. Ophus, *Optimizing disk registration algorithms for nanobeam electron diffraction strain mapping,* Ultramicroscopy **176**, 170 (2017).

[64] D. Johnstone, P. Crout, M. Nord, C. Francis, J. Laulainen, S. Høgås, E. Opheim, B. Martineau, T. Bergh, E. Prestat, N. Cautaerts, S. Smeets, H. W. Ånes, A. Ross, J. Broussard, S. Collins, T. Furnival, D. Jannis, I. Hjorth, S. Huang, E. Jacobsen, M. Danaie, A. Herzing, T. Poon, S. Dagenborg, T. Doherty, J. Morzy, A. Iqbal, T. Ostasevicius, T. I. Thorsen, M. von Lany, and R. Tovey, *pyxem/pyxem: pyxem 0.15.1,* (2023).

[65] B. H. Savitzky, S. E. Zeltmann, L. A. Hughes, H. G. Brown, S. Zhao, P. M. Pelz, T. C. Pekin, E. S. Barnard, J. Donohue, L. Rangel DaCosta, E. Kennedy, Y. Xie, M. T. Janish, M. M. Schneider, P. Herring, C. Gopal, A. Anapolsky, R. Dhall, K. C. Bustillo, P. Ercius, M. C. Scott, J. Ciston, A. M. Minor, and C. Ophus, *py4DSTEM: A Software Package for Four-Dimensional Scanning Transmission Electron Microscopy Data Analysis,* Microscopy and Microanalysis **27**, 712–743 (2021).

[66] E. F. Rauch and M. Véron, *Automated crystal orientation and phase mapping in TEM,* Materials Characterization **98**, 1 (2014).

[67] J. Jeong, N. Cautaerts, G. Dehm, and C. H. Liebscher, *Automated Crystal Orientation Mapping by Precession Electron Diffraction-Assisted Four-Dimensional Scanning Transmission Electron Microscopy Using a Scintillator-Based CMOS Detector,* Microscopy and Microanalysis **27**, 1102 (2021).

[68] M. Bolhuis, S. E. van Heijst, J. J. M. Sangers, and S. Conesa-Boj, *4D-STEM Nanoscale Strain Analysis in van der Waals Materials: Advancing beyond Planar Configurations,* Small Science **4**, 2300249 (2024).

[69] S. E. van Heijst, M. Bolhuis, A. Brokkelkamp, J. J. M. Sangers, and S. Conesa-Boj, *Heterostrain-Driven Bandgap Increase in Twisted WS_2: A Nanoscale Study,* Advanced Functional Materials **34**, 2307893 (2024).

[70] D. G. Lowe, *Distinctive Image Features from Scale-Invariant Keypoints,* International Journal of Computer Vision **60**, 91 (2004).

[71] J. L. Rouvière and E. Sarigiannidou, *Theoretical discussions on the geometrical phase analysis,* Ultramicroscopy **106**, 1 (2005).

4

ILLUMINATING THE ELECTRONIC PROPERTIES OF WS_2 POLYTYPISM WITH ELECTRON MICROSCOPY

Tailoring the specific stacking sequence (or polytypes) of layered materials represents a powerful strategy to identify and design novel physical properties. While nanostructures based on transition metal dichalcogenides (TMDs) with either the 2H or 3R crystalline phases have been routinely studied, our understanding of TMD nanomaterials with mixed 2H/3R polytypes remains limited. In this chapter, we examine mixed 2H/3R free-standing tungsten disulfide (WS_2) *nanostructures that exhibit a flower-like configuration, using state-of-the-art transmission electron microscopy (TEM). We correlate the diverse shape-morphology configurations with pertinent local electronic properties, such as edge, surface, and bulk plasmons. Analysis utilizing machine learning reveals that the 2H/3R polytype has an indirect bandgap of* $E_{BG} = 1.6^{+0.3}_{-0.2}$ *eV. Our findings provide significant insights into TMD nanomaterials with mixed crystalline phases, paving the way for a deeper understanding of their properties.*

Parts of this chapter have been published in *Annalen der Physik* **533**, 2000499 (2021) by **S. E. van Heijst**, M. Mukai, E. Okunishi, H. Hashiguchi, L. I. Roest, L. Maduro, J. Rojo, and S. Conesa-Boj.

4.1. INTRODUCTION

Many of the remarkable electronic and optical properties exhibited by transition metal dichalcogenide (TMD) materials can be traced back to the underlying periodic arrangements of their layers, the so-called stacking sequences [1, 2]. Therefore, identifying and controlling these stacking sequences provides a powerful handle in the quest to design novel TMD-based nanostructures with tailored functionalities.

The most common stacking sequences present in TMDs are the 2H and the 3R polytypes [3–5]. The 2H phase belongs to the space group P63/mmc and has a unit cell composed of a bilayer following the AA' stacking sequence, a configuration characterized by an inversion symmetry [6]. The 3R phase belongs instead to the space group R3m and is defined by a bilayer with an AB stacking sequence, which as opposed to the 2H phase does not exhibit inversion symmetry [7]. Both crystalline phases are known to display a semiconducting behavior [8]. While several studies of the structural, optical, and electronic properties of TMDs based on either the 2H or the 3R phases have been reported [9–11], much less is known about how these properties are modified in the presence of a mixed 2H/3R polytypism [12]. Unraveling the implications of such polytypism in TMDs would open new avenues in applications from nanoplasmonics and nanoelectronics to catalysis [13–15].

This chapter reports on the characterization of tungsten disulfide (WS_2) flower-like nanostructures ("nanoflowers") composed of randomly oriented flakes (the "petals") arising from a common point (the "stem"). These WS_2 nanoflowers display a rich variety of shape-morphology configurations, such as lying petals and edge-exposed standing petals. Together with their polytypism, this unique feature makes these nanostructures an ideal laboratory for studying the modifications in the local electronic properties of WS_2.

First, aberration-corrected scanning transmission electron microscopy (AC-STEM) [16] is used to reveal the presence of the 2H/3R polytypism in these nanostructures. Then, the nature of their edge, surface, and bulk plasmonic excitations is fingerprinted by means of spatially-resolved electron energy-loss spectroscopy (EELS) [17, 18]. The origin of relevant features in the EEL spectra is traced back to specific structural characteristics of the nanoflowers, and in particular one can identify contributions associated with the surface and interlayer couplings as well as to the edges of the WS_2 petals. The combination of EELS measurements with machine learning is then exploited to chart the ultra-low-loss region ($\Delta E \leq 5$ eV) and determine that the 2H/3R polytype of bulk WS_2 exhibits a semiconductor behavior with an indirect bandgap with a value of $E_{BG} = 1.6^{+0.3}_{-0.2}$ eV.

4.2. FABRICATION OF WS_2 NANOFLOWERS

The WS_2 nanostructures studied within this chapter were grown by means of chemical vapor deposition (CVD) directly on a transmission electron microscopy (TEM) microchip. This microchip consists of a silicon frame with a window in the center, and a holey silicon nitride (Si_3N_4) film spanned across (Figure 4.1a) [19, 20]. First, tungsten trioxide (WO_3) powder was deposited on this microchip. To this end, WO_3 powder (50 mg) was dispersed in 1 mL of isopropanol (ISO). Subsequently, a few droplets of this mixture were deposited onto the microchip using a pipette. Once the ISO has evaporated, WO_3 powder is left dispersed on the microchip (Figure 4.1b).

Following these preparatory steps, the microchip is loaded into the central zone of the CVD furnace introduced in Section 2.5 of Chapter 2. A crucible holding 400 mg of sulfur was placed upstream. The growth protocol adopted for the subsequent fabrication procedure is also discussed in Section 2.5 of Chapter 2, where the reaction temperature is 750 °C, the reaction flow rate is 150 sccm and the reaction time is 1 hour. Figure 4.1b displays a schematic diagram summarizing the synthesis of the WS_2 nanostructures.

Figure 4.1c displays a low-magnification annular dark-field (ADF) scanning transmission electron microscopy (STEM) image of the as-grown WS_2 nanostructures. It is observed that the nanostructures exhibit flower-like morphologies composed of randomly oriented flakes (the "petals") arising from a common point (the "stem") (Figure 4.1d).

Energy-dispersive X-ray spectroscopy (EDS) measurements were carried out in order to verify the chemical composition of the nanoflowers. The area inspected by EDS mapping is marked by the white square in Figure 4.1c. The resulting EDS maps of tungsten (blue) and sulfur (yellow) are shown in Figure 4.1e. The EDS characterization of the sample demonstrates the presence of both tungsten and sulfur in the nanostructures, thus confirming the composition of the nanoflowers to be WS_2.

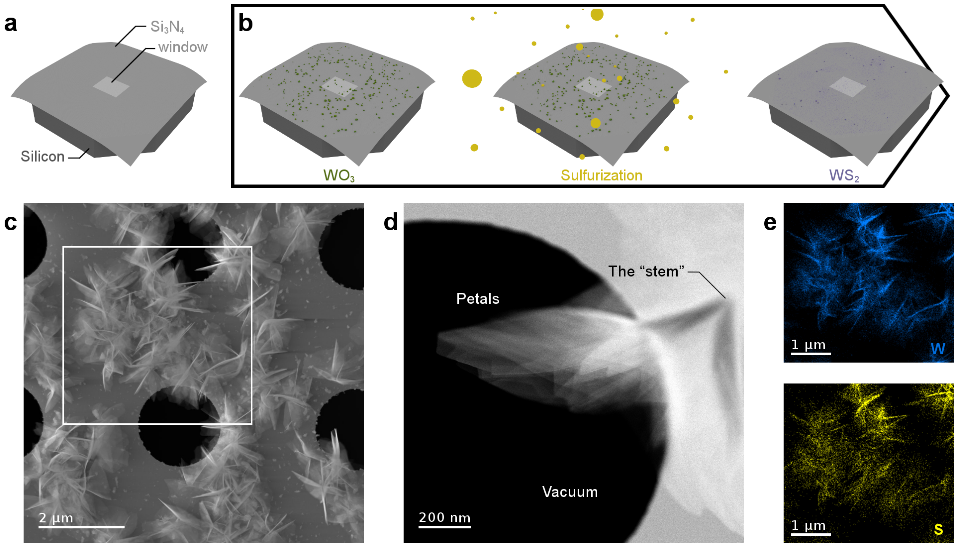

Figure 4.1: Schematic illustration of (a) the TEM microchip and (b) the synthesis procedure for the WS_2 nanoflowers on this microchip. (c) Low-magnification ADF-STEM top-view perspective of the as-grown WS_2 nanostructures illustrating their flower-like morphology. The nanoflowers are grown on top of a holey Si_3N_4 TEM grid. (d) ADF-STEM image of one representative WS_2 nanoflower composed by free-standing, randomly oriented WS_2 flakes (petals) protruding from the stem of the flower. This configuration is especially advantageous to eliminate the contributions related to the nanostructure-support film coupling effects. (e) EDS compositional maps of the region marked by the white square in (c), with the tungsten (W) and sulfur (S) maps represented in blue and yellow, respectively.

4.3. Mixed 2H/3R Polytypism in WS$_2$ Nanoflowers

Figures 4.2a-b display respectively low-magnification ADF- and bright-field (BF-) STEM images of the tip region of one representative WS$_2$ petal. Variations in the image contrast clearly indicate the presence of terraces with varying layer counts, and consequently, different thicknesses ranging from 2 nm up to 30 nm. Figure 4.2c then displays the atomic-resolution ADF-STEM image corresponding to the same petal. The petal has been oriented along the [0001] direction in order to ascertain the underlying crystalline structure. Herein, each bright spot corresponds to an atomic column, composed of alternating tungsten and sulfur atoms.

This atomic-resolution image appears to suggest a 3R phase, characterized by a hexagonal honeycomb structure with an atom at its center. However, the ADF line profile extracted from the atomic resolution image across six lattice points (Figure 4.2d) indicates a threefold periodicity which is inconsistent with the 3R phase.

This observed periodicity instead suggests a layer stacking order of the type BAA', characteristic of a mixture of the 2H (AA') and 3R (AB) phases [21]. As displayed by the characteristic unit cell of polytypic 2H/3R (Figure 4.2e), the stacking sequence exhibits a broken inversion symmetry. Such polytypism has been reported before in related materials like molybdenum disulfide (MoS$_2$) [12]. As mentioned before, the 2H and 3R phases in their bilayer form are characterized by different stacking sequences, namely AA' and AB, which are depicted in Figure A.1 in Appendix A. In the 2H phase, each tungsten atom

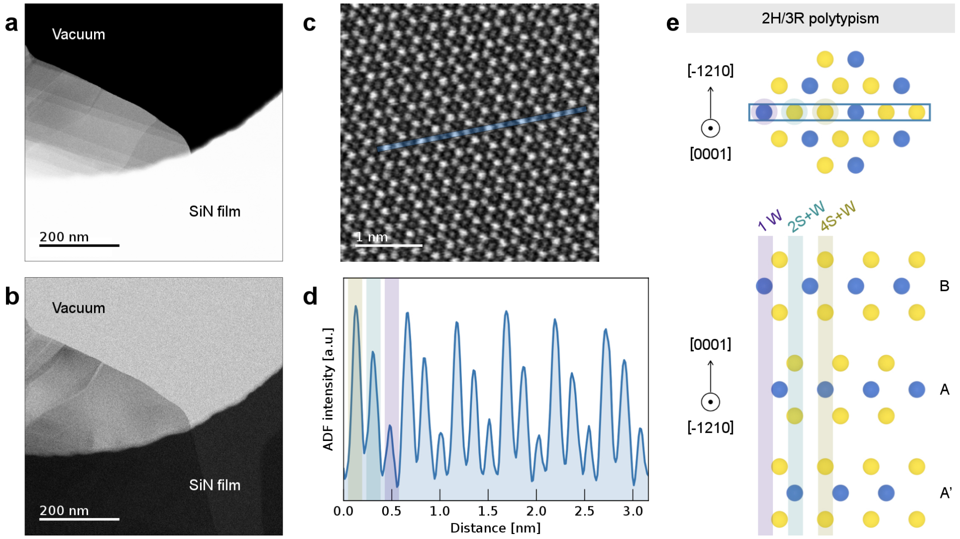

Figure 4.2: (a-b) Low-magnification ADF- and BF-STEM images respectively of a representative WS$_2$ petal, where the vacuum and Si$_3$N$_4$ film regions are also indicated. The difference in contrast observed in the petal of (a) corresponds to terraces of different thicknesses. (c) Atomic resolution image corresponding to the petal tip area. (d) The ADF intensity profile acquired along the blue region in (c). (e) Schematic atomic model of the top-view (upper panel) and side-view (lower) of the crystalline structure associated to the crystallographic unit cell of 2H/3R polytype.

aligns directly with the sulfur atoms, and thus, the two layers exhibit inversion symmetry. In the 3R phase instead, the tungsten atom is staggered over the sulfur atoms, resulting in a stacking sequence lacking inversion symmetry. Therefore, a mixture of the two phases follows the BAA' sequence, where the third layer is staggered with the sulfur atoms over the tungsten atoms of the second layer.

The area measured has a thickness of around 5 nm, which is equivalent to around 5 layers. The smallest thickness of any region in the specimen is found to be around 3 layers. ADF line profiles taken at different locations on other petals, corresponding to both single terraces and their transition region, are discussed in Section A.2 of Appendix A. Consistently, these exhibit the characteristic threefold periodicity of the 2H/3R polytype.

4.4. FINGERPRINTING ELECTRONIC EXCITATIONS WITH SPATIALLY-RESOLVED EELS

The nature of collective electronic excitations such as surface and edge plasmons arising in the 2H/3R polytypism is investigated by means of spatially-resolved EELS. Figures 4.3a-b display BF- and ADF-STEM images of horizontal WS_2 flakes (the nanoflower petals) overlapping among them. Some of these petals are composed of terraces of different thicknesses, as indicated by the contrast variations in the ADF-STEM image in Figure 4.3b. Since these petals are suspended on vacuum, it is possible to characterize their edge, surface, and bulk plasmons while reducing the contribution from coupling effects related to the nanostructure support film. It should be emphasized that, in this specific geometric configuration, the direction of the incident electron beam closely aligns with the c-axis of the WS_2 petals.

Figure 4.3c displays the spatially-resolved EELS map recorded in the region marked with a gray rectangle in Figure 4.3b. Herein, the intensity of each pixel represents an individual EEL spectrum. Figures 4.3d-g display the intensity maps associated with the same EEL signals, now integrated over specific energy-loss windows: [2.5, 4.5], [8, 9], [12.5, 20], and [21.5, 25] eV respectively. In these maps, the brighter regions highlight the dominant features appearing for each specific energy-loss range.

To better isolate the main features displayed by Figures 4.3d-g, representative EEL spectra associated to locations along the horizontal petals indicated in Figure 4.3b are presented in Figures 4.3h-i. A prominent peak around 23 eV is a common feature observed in both sets of spectra. This peak can be associated with the WS_2 bulk plasmon [22]. The intensity of this peak decreases as one moves from thicker towards thinner regions, following the directions of the arrows in Figure 4.3b. This effect is particularly marked in Figure 4.3i, corresponding to a petal composed by terraces of different thicknesses.

From the intensity map corresponding to energy losses integrated between 12.5 and 20 eV (Figure 4.3f), one observes a significant contribution arising from the regions constituted by two different overlapping petals. The individual spectra display indeed a shoulder-like feature located around 17 eV, which becomes more marked in the thinner regions. In this context, the free-electron gas dielectric response theory predicts that the surface plasmon energy (E_s) should relate to that of the bulk one (E_p) by $E_s = E_p/\sqrt{2}$.

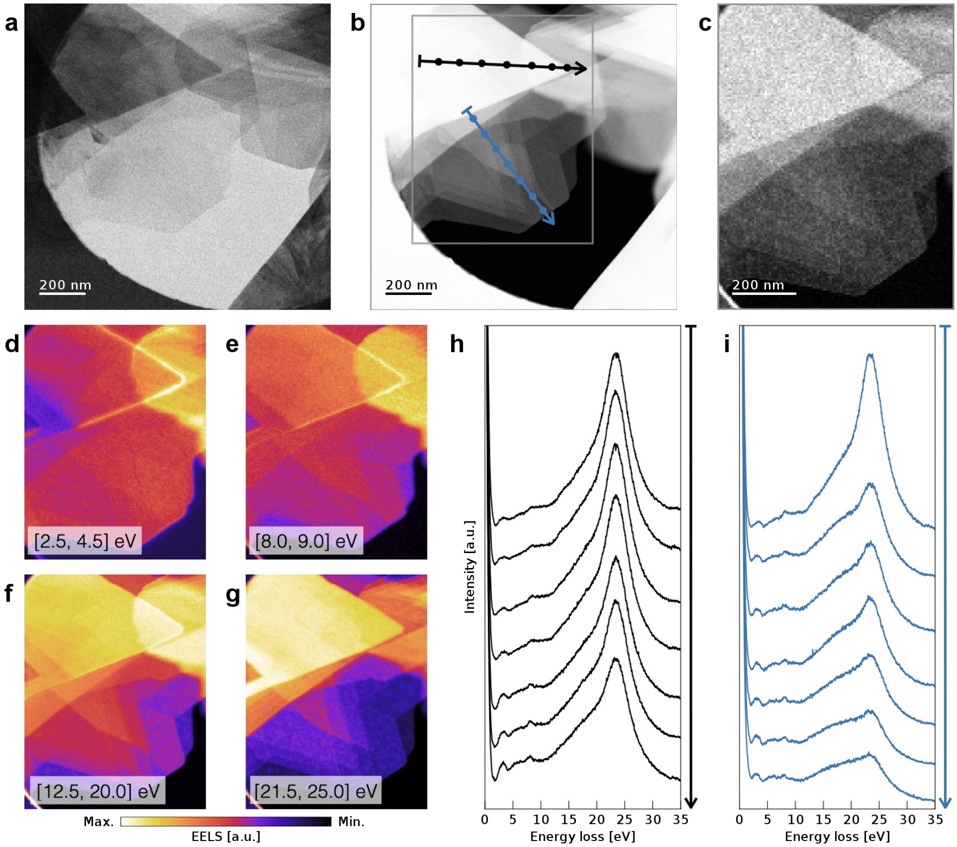

Figure 4.3: (a-b) BF- and ADF-STEM images respectively of horizontal (flat) WS_2 petals. (c) Spatially-resolved EELS map of the area indicated with a gray rectangle in (b). (d-g) Intensity maps of the EEL signals integrated for different energy-loss windows. (h-i) Individual EEL spectra taken at different locations along the horizontal petals as indicated by the black and blue arrows in (b). The spectra displayed in (h) correspond to a region characterized by the overlap of individual petals arising both from the left and the right sides of (a-b). The spectra in (i) corresponds instead to a region displaying a petal composed by different terraces and thus different thicknesses.

In the present case, this prediction corresponds to around $E_s = 16$ eV, consistent with the experimentally observed value and confirming the surface plasmon nature of this shoulder-like feature [9].

The individual spectra in Figures 4.3h-i also display less intense peaks located at energy losses around 3 and 8 eV. From the integrated EELS maps of Figure 4.3d, one observes that the 3 eV peak can be mainly associated to the edges of the WS_2 petals. Indeed, the largest signals in this energy-loss window arise from the tip of the edges and the adjacent regions. Further, it is observed that the peak at 8 eV receives its main contribution associated to the interlayer coupling between petals (Figure 4.3e). Indeed, this peak could be associated to the six π electrons (four of which are from the sulfur atoms) which are responsible for the interlayer interactions [23, 24].

Figures 4.4a-b display the ADF-STEM image and the corresponding spatially-resolved EELS map of another representative WS_2 nanoflower composed now of both flat and tilted WS_2 petals. For the tilted petals, their c-axis is nearly perpendicular to the direction of the electron beam. Figure 4.4c compares the energy-loss functions for the locations indicated in Figure 4.4b and recorded along a series of flat and tilted WS_2 petals respectively. Spectra 6, 9, and 10 in Figure 4.4b are recorded in vacuum but close enough to the petal (aloof configuration), in order to identify possible contributions from its surface plasmons. Observations show that the 3 eV peak is present in both flat and tilted petals, and also in the vacuum location sp9. In the vacuum region near the sample a peak corresponding to energy losses of around 3 eV is observed, whose location shifts rightwards to 3.5 eV when moving from the non-penetrating (vacuum) to the penetrating (WS_2 petal) locations. First-principle density functional theory (DFT) calculations on 2H/3R WS_2 bulk reveal the physical nature of this feature [25]. A comparison of the total density of states (DOS) of 2H/3R WS_2 bulk with that of tungsten and sulfur reveals that the main contribution to the total DOS is attributed to the tungsten atoms. In particular, it suggests that the peak around 3 eV is associated to electronic transitions from d states of tungsten to unoccupied d states of tungsten [25].

Regarding the higher-energy peaks, our observations indicate that the tilted petal configuration induces a strong coupling between the surfaces which results in a split of the 17 eV surface mode into a peak at around 20 eV and a forest of peaks between 5 and 15 eV. In Figure 4.4d, a two-Gaussian model fit has been performed to sp1 (flat) and sp8 (tilted) in the range between 10 and 35 eV. We can associate the two resulting Gaussian distributions with contributions from the bulk and surface plasmons and show how in the latter case the surface contribution at 17 eV blueshifts towards around 20 eV while becoming more marked as compared to the bulk one. Related phenomena have been reported in the case of WS_2 nanotubes with very small radii [22, 26].

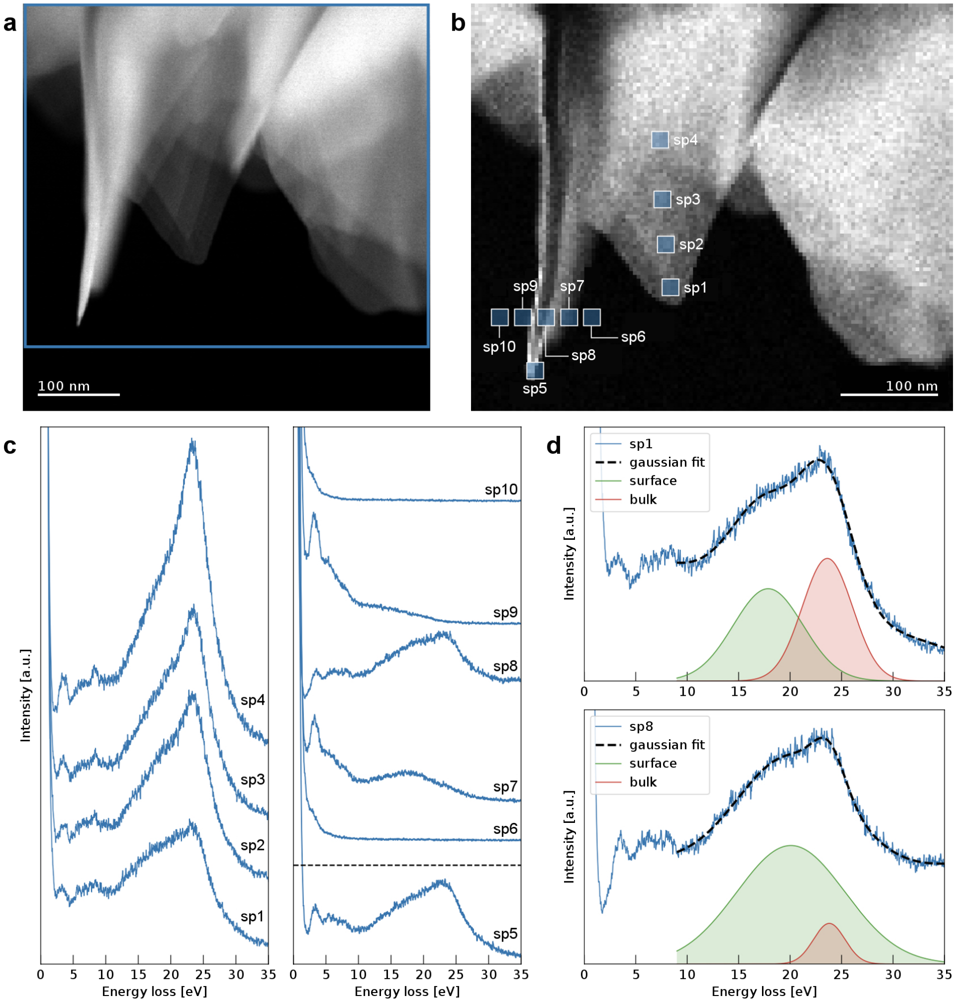

Figure 4.4: (a) ADF-STEM image of another representative WS$_2$ nanostructure composed both by flat and tilted WS$_2$ petals. (b) Spatially-resolved EELS map of the area indicated with a blue rectangle in (a). (c) Individual EEL spectra corresponding to the locations indicated in (b). Spectra 1 to 4 are associated to a flat region of the WS$_2$ petal, while spectra 6 to 10 correspond to locations that cross the tilted WS$_2$ petal, with sp5 recorded at its tip. Note that sp6, 9, and 10 are recorded in vacuum but close enough to the petal to identify possible contributions from its surface plasmons. (d) Spectra 1 and 8 where a two-Gaussian model fit has been performed in the range between 10 and 35 eV. The two resulting Gaussian distributions are also displayed and can be associated to the contributions from the bulk and surface plasmons.

4.5. BANDGAP DETERMINATION OF POLYTYPIC 2H/3R WS_2 USING MACHINE LEARNING

The profile of the low-loss region of EEL spectra contains valuable information concerning the magnitude and type of the bandgap. Exploiting this information requires the subtraction of the zero-loss peak (ZLP) contribution. Here, we investigate the bandgap of polytypic 2H/3R WS_2 nanoflowers using the analysis framework EELSFITTER [27, 28], which was previously discussed in Section 3.2 in Chapter 3.

Figure 4.5a displays a spatially-resolved EELS map taken on a representative petal of a WS_2 nanoflower. This petal corresponds to that depicted in Figures 4.2a-b. An EEL spectrum is extracted at the location marked by the purple square for further evaluation of the low-loss region by use of the EELSFITTER framework. The chosen area corresponds to a relatively thick region of the WS_2 petal, consequently bulk behavior is expected.

Figure 4.5b displays both the original and subtracted inelastic EEL spectra together with the calculated ZLP. The uncertainty bands indicate the 68% confidence level intervals associated to the ZLP prediction and the subtracted EEL spectrum. As noted previously, the profile of the subtracted inelastic EEL spectrum in the onset region reveals details regarding the bandgap energy (E_{BG}) and its nature. We employed polynomial fitting to extract this information. The results of such a fit, together with the corresponding uncertainty bands, are displayed in the inset of Figure 4.5b. In this case, the best-fit model values were found to be $E_{BG} = 1.6^{+0.3}_{-0.2}$ eV for the bandgap energy and $b = 1.3^{+0.3}_{-0.4}$ for the exponent. Given that $b \approx 3/2$ is theoretically expected for an indirect bandgap, this result supports its presence. The determined value and nature of the bandgap align, within uncertainties, with first-principle DFT calculations carried out on 2H/3R WS_2 bulk [25].

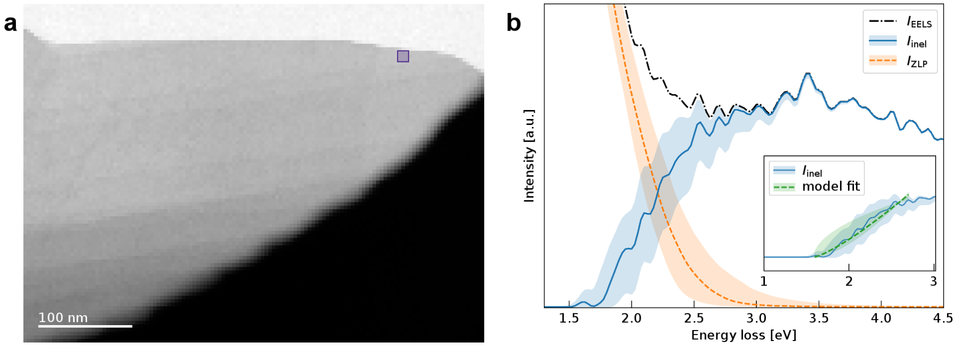

Figure 4.5: (a) Spatially-resolved EELS map of one representative petal of a WS_2 nanoflower. This is the same petal as shown in the STEM images in Figure 4.2. The purple square indicate the location of the EEL spectra used to determine the bandgap by means of machine learning methods. (b) The low-loss region of the original EEL spectrum (I_{EELS}) recorded at the location indicated in (a), together with the resulting subtracted inelastic EEL spectrum (I_{inel}). The ZLP model prediction (I_{ZLP}) used for the subtraction procedure is also displayed. The inset shows the result of the polynomial fit to the onset region of the subtracted EEL spectrum and the bands represent the 68% CL intervals for the model uncertainties.

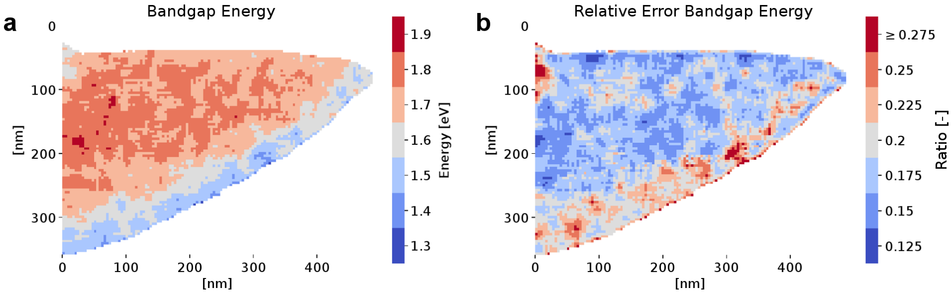

Figure 4.6: (a) Spatially-resolved bandgap energy map corresponding to the WS$_2$ nanoflower petal as shown in Figure 4.5a. (b) The relative uncertainties (68% confidence level intervals) associated to the bandgap energy map in (a). A mask has been applied to exclude pixels containing a contribution from the substrate as well as those related to the vacuum. Adapted from [28]

For a comprehensive understanding of the spatially-resolved bandgap, the EELSFITTER framework can also be used to analyze the entire spectral image as shown in Figure 4.5a, rather than just a single EEL spectrum. The results from the evaluation of an individual EEL spectrum indicated the bandgap to be indirect in nature. Hence, the exponent b is set to a fixed value of $^3/_2$ for the evaluation of the entire WS$_2$ petal.

Figures 4.6a and 4.6b depict the maps for the bandgap energy and its corresponding uncertainty, respectively. Herein a mask has been applied to remove those pixels corresponding to the vacuum and the area in which the Si$_3$N$_4$ film (substrate) is present. As illustrated in Figure 4.6, the bandgap energy ranges from 1.4 to 1.8 eV, with associated uncertainties of 15 to 25%.

4.6. CONCLUSION

The effects of unconventional mixed crystalline phases on the properties of TMD nanomaterials are not yet fully understood. This study offers a comprehensive characterization of WS$_2$ nanoflowers. These structures serve as an ideal laboratory to investigate the modifications of local electronic properties in WS$_2$, thanks to their mixed 2H/3R polytypism and rich variety of shape-morphology configurations.

Using advanced AC-STEM and EELS techniques, we fingerprinted the characteristics of their edge, surface, and bulk plasmonic excitations linking distinctive features in the EEL spectra to the nanoflowers' specific structural attributes. We also determined that the 2H/3R polytype of bulk WS$_2$ exhibits semiconductor behavior with an indirect bandgap of $E_{\mathrm{BG}} = 1.6^{+0.3}_{-0.2}$ eV. In addition, the spatial distribution of the bandgap energy was mapped showing its local variations.

This chapter lays foundational work for a program dedicated to developing systematic strategies for the controlled growth of TMD nanostructures with mixed crystalline phases.

REFERENCES

[1] D. Voiry, A. Mohite, and M. Chhowalla, *Phase engineering of transition metal dichalcogenides,* Chemical Society Reviews **44**, 2702 (2015).

[2] X. Zhang, Z. Lai, Q. Ma, and H. Zhang, *Novel structured transition metal dichalcogenide nanosheets,* Chemical Society Reviews **47**, 3301 (2018).

[3] J. A. Wilson and A. D. Yoffe, *The transition metal dichalcogenides discussion and interpretation of the observed optical, electrical and structural properties,* Advances in Physics **18**, 193 (1969).

[4] J. He, K. Hummer, and C. Franchini, *Stacking effects on the electronic and optical properties of bilayer transition metal dichalcogenides* MoS_2*,* $MoSe_2$*,* WS_2*, and* WS_2*,* Physical Review B **89**, 075409 (2014).

[5] R. Suzuki, M. Sakano, Y. J. Zhang, R. Akashi, D. Morikawa, A. Harasawa, K. Yaji, K. Kuroda, K. Miyamoto, T. Okuda, K. Ishizaka, R. Arita, and Y. Iwasa, *Valley-dependent spin polarization in bulk* MoS_2 *with broken inversion symmetry,* Nature Nanotechnology **9**, 611 (2014).

[6] D. Xiao, G.-B. Liu, W. Feng, X. Xu, and W. Yao, *Coupled Spin and Valley Physics in Monolayers of* MoS_2 *and Other Group-VI Dichalcogenides,* Physical Review Letters **108**, 196802 (2012).

[7] J. Shi, P. Yu, F. Liu, P. He, R. Wang, L. Qin, J. Zhou, X. Li, J. Zhou, X. Sui, S. Zhang, Y. Zhang, Q. Zhang, T. C. Sum, X. Qiu, Z. Liu, and X. Liu, *3R* MoS_2 *with Broken Inversion Symmetry: a Promising Ultrathin Nonlinear Optical Device,* Advanced Materials **29**, 1701486 (2017).

[8] R. Yang, S. Feng, X. Lei, X. Mao, A. Nie, B. Wang, K. Luo, J. Xiang, F. Wen, C. Mu, Z. Zhao, B. Xu, H. Zeng, Y. Tian, and Z. Liu, *Effect of layer and stacking sequence in simultaneously grown 2H and 3R* WS_2 *atomic layers,* Nanotechnology **30**, 345203 (2019).

[9] P. Johari and V. B. Shenoy, *Tunable Dielectric Properties of Transition Metal Dichalcogenides,* ACS Nano **5**, 5903 (2011).

[10] C. Cong, J. Shang, X. Wu, B. Cao, N. Peimyoo, C. Qiu, L. Sun, and T. Yu, *Synthesis and Optical Properties of Large-Area Single-Crystalline 2D Semiconductor* WS_2 *Monolayer from Chemical Vapor Deposition,* Advanced Optical Materials **2**, 131 (2014).

[11] Y.-C. Lin, S. Li, H.-P. Komsa, L.-J. Chang, A. V. Krasheninnikov, G. Eda, and K. Suenaga, *Revealing the Atomic Defects of* WS_2 *Governing its Distinct Optical Emissions,* Advanced Functional Materials **28**, 1704210 (2018).

[12] J.-U. Lee, K. Kim, S. Han, G. H. Ryu, Z. Lee, and H. Cheong, *Raman Signatures of Polytypism in Molybdenum Disulfide,* ACS Nano **10**, 1948 (2016).

[13] R. J. Toh, Z. Sofer, J. Luxa, D. Sedmidubský, and M. Pumera, *3R phase of MoS_2 and WS_2 outperforms the corresponding 2H phase for hydrogen evolution,* Chemical Communications **53**, 3054 (2017).

[14] Z. Zeng, X. Sun, D. Zhang, W. Zheng, X. Fan, M. He, T. Xu, L. Sun, X. Wang, and A. Pan, *Controlled Vapor Growth and Nonlinear Optical Applications of Large-Area 3R Phase WS_2 and WSe_2 Atomic Layers,* Advanced Functional Materials **29**, 1806874 (2019).

[15] D. Tan, M. Willatzen, and Z. L. Wang, *Prediction of strong piezoelectricity in 3R-MoS_2 multilayer structures,* Nano Energy **56**, 512 (2019).

[16] O. L. Krivanek, M. F. Chisholm, V. Nicolosi, T. J. Pennycook, G. J. Corbin, N. Dellby, M. F. Murfitt, C. S. Own, Z. S. Szilagyi, M. P. Oxley, S. T. Pantelides, and S. J. Pennycook, *Atom-by-atom structural and chemical analysis by annular dark-field electron microscopy,* Nature **464**, 571 (2010).

[17] O. L. Krivanek, T. C. Lovejoy, N. Dellby, T. Aoki, R. W. Carpenter, P. Rez, E. Soignard, J. Zhu, P. E. Batson, M. J. Lagos, R. F. Egerton, and P. A. Crozier, *Vibrational spectroscopy in the electron microscope,* Nature **514**, 209 (2014).

[18] J. A. Hunt and D. B. Williams, *Electron energy-loss spectrum-imaging,* Ultramicroscopy **38**, 47 (1991).

[19] M. Bolhuis, J. Hernandez-Rueda, S. E. van Heijst, M. Tinoco Rivas, L. Kuipers, and S. Conesa-Boj, *Vertically-oriented MoS_2 nanosheets for nonlinear optical devices,* Nanoscale **12**, 10491 (2020).

[20] M. O. Cichocka, M. Bolhuis, S. E. van Heijst, and S. Conesa-Boj, *Robust Sample Preparation of Large-Area In- and Out-of-Plane Cross Sections of Layered Materials with Ultramicrotomy,* ACS Applied Materials & Interfaces **12**, 15867 (2020).

[21] A. Yan, W. Chen, C. Ophus, J. Ciston, Y. Lin, K. Persson, and A. Zettl, *Identifying different stacking sequences in few-layer CVD-grown MoS_2 by low-energy atomic-resolution scanning transmission electron microscopy,* Physical Review B **93**, 041420 (2016).

[22] M. Kociak, O. Stéphan, L. Henrard, V. Charbois, A. Rothschild, R. Tenne, and C. Colliex, *Experimental Evidence of Surface-Plasmon Coupling in Anisotropic Hollow Nanoparticles,* Physical Review Letters **87**, 075501 (2001).

[23] W. Y. Liang and S. L. Cundy, *Electron energy loss studies of the transition metal dichalcogenides,* The Philosophical Magazine: A Journal of Theoretical Experimental and Applied Physics **19**, 1031 (1969).

[24] K. Zeppenfeld, *Electron energy losses and optical anisotropy of MoS_2 single crystals,* Optics Communications **1**, 377 (1970).

[25] L. Maduro, S. E. van Heijst, and S. Conesa-Boj, *First-Principles Calculation of Optoelectronic Properties in 2D Materials: The Polytypic WS_2 Case,* ACS Physical Chemistry Au **2**, 191 (2022).

[26] D. Taverna, M. Kociak, V. Charbois, and L. Henrard, *Electron energy-loss spectrum of an electron passing near a locally anisotropic nanotube,* Physical Review B **66**, 235419 (2002).

[27] L. I. Roest, S. E. van Heijst, L. Maduro, J. Rojo, and S. Conesa-Boj, *Charting the low-loss region in electron energy loss spectroscopy with machine learning,* Ultramicroscopy **222**, 113202 (2021).

[28] A. Brokkelkamp, J. ter Hoeve, I. Postmes, S. E. van Heijst, L. Maduro, A. V. Davydov, S. Krylyuk, J. Rojo, and S. Conesa-Boj, *Spatially Resolved Band Gap and Dielectric Function in Two-Dimensional Materials from Electron Energy Loss Spectroscopy,* The Journal of Physical Chemistry A **126**, 1255 (2022).

5

HETEROSTRAIN-DRIVEN BANDGAP INCREASE IN TWISTED WS_2: A NANOSCALE STUDY

Twisted two-dimensional (2D) materials present an enticing platform for exploring diverse electronic properties owing to the tunability of their bandgap energy. However, the intricate relationship between local heterostrain fields, thickness, and bandgap energy remains insufficiently understood, particularly at the nanoscale. Here, we present a comprehensive nanoscale study elucidating the remarkable sensitivity of the bandgap energy to both thickness and heterostrain fields within twisted tungsten disulfide (WS_2) nanostructures. Our approach integrates electron energy-loss spectroscopy (EELS) enhanced by machine learning with four-dimensional (4D) scanning transmission electron microscopy (STEM). Through this synergistic methodology, we unveil enhancements up to 20% in the bandgap energy with respect to the specimen thickness. This phenomenon is traced back to sizable deformation angles present within individual layers, which can be directly linked to distinct variations in local heterostrain fields. Our findings represent a significant advancement in comprehending the electronic behavior of twisted 2D materials and introduce a novel methodological framework with far-reaching implications for twistronics and the investigation of other materials within the nanoscience domain.

Parts of this chapter have been published in *Advanced Functional Materials* **34**, 2307893 (2024) by **S. E. van Heijst**, M. Bolhuis, A. Brokkelkamp, J. J. M. Sangers, and S. Conesa-Boj.

5.1. INTRODUCTION

TWISTED two-dimensional (2D) materials have emerged as promising platforms with tunable electronic properties [1–6], offering exciting prospects in various fields, including field-effect transistors [7, 8], integrated circuits [9], and photodetectors [10, 11]. A key parameter dictating the electronic behavior of 2D materials is the bandgap energy [12–21].

Understanding the influence of factors such as layer count, interlayer distance, twist angle, and local strain fields on the bandgap energy has seen significant progress [22–26]. In particular, the twisted stacking of van der Waals materials with Moiré superlattices has emerged as a novel approach to tailor their physical properties by manipulating the crystal symmetry. Recent studies have also highlighted the interplay between extrinsic nonuniform heterostrain and intrinsic atomic reconstruction in the evolution of Moiré structures in twisted 2D materials [27]. This interplay introduces local inhomogeneous intra-layer strain within the Moiré, leading to intriguing modulations in the electronic properties [28–31]. Notably, heavily deformed Moirés can exhibit significant modulations in the conduction band, resulting in bandgap variations of up to 300 meV [32]. Additionally, Moiré patterns in hexagonal boron nitride (h-BN)-supported monolayer graphene, induced by non-uniform strain fields [23], have been observed to result in bandgap openings [24].

Another aspect that deserves attention is the influence of material thickness on bandgap dynamics. Even slight changes in thickness can lead to significant modifications in the bandgap of these unique 2D materials [12–14, 21, 33]. To achieve a comprehensive understanding of the electronic properties, particularly the dynamics of the bandgap, it's crucial to consider the interplay between material thickness and strain fields.

In this chapter, we present a comprehensive investigation of twisted 2D materials that addresses these challenges. Specifically, naturally twisted tungsten disulfide (WS$_2$) nanostructures of two types are examined: *1)* well-aligned, without Moiré superlattice, and *2)* displaying a spiral-like configuration where each layer is slightly twisted relative to the adjacent ones. This study combines electron energy-loss spectroscopy (EELS) enhanced by machine learning techniques [34, 35] with four-dimensional (4D) scanning transmission electron microscopy (STEM). This multi-pronged methodology enables the accurate evaluation of bandgap energy and local strain fields with nanoscale spatial resolution, facilitating an in-depth exploration of the interplay between bandgap energy, thickness, and strain fields. The findings reveal a pronounced increase in the bandgap energy within the twisted WS$_2$ specimen characterized by a spiral-like configuration, by up to 20%, as a function of its local thickness. This phenomenon is traced back to sizable deformation angles present within individual layers, which are accompanied by noticeable changes in local strain fields. This observation highlights the remarkable sensitivity of bandgap dynamics in twisted 2D materials to local strain fluctuations.

Importantly, while the work presented in this chapter focuses on van der Waals materials, the versatility of the method extends beyond this specific application. It can easily be adapted for strain-field characterization in other low-dimensional nanostructured materials, thereby broadening the spectrum of possible applications [1–6].

Overall, this study offers a comprehensive investigation of the bandgap energy variations in twisted 2D materials, shedding light on the interplay between thickness, strain fields, and electronic properties. The insights gained from this research contribute to the understanding of twistronics and pave the way for future studies exploring the manipulation of local strain for tailored electronic functionalities in various materials.

5.2. SPATIALLY-RESOLVED BANDGAP AND THICKNESS CORRELATION ANALYSIS OF TWISTED WS$_2$

A diverse set of naturally twisted WS$_2$ specimens was grown directly on a transmission electron microscopy (TEM) microchip. The fabrication process that yielded these specimens is identical to that used for the WS$_2$ nanoflowers as discussed in Section 4.2 of Chapter 4. The only difference between the processes is the substrate. Instead of a holey silicon nitride (Si$_3$N$_4$) film, a continuous Si$_3$N$_4$ film spans across the microchip. This change in substrate is suspected to cause the morphology to deviate from the nanoflower morphology to the naturally twisted WS$_2$ specimens discussed in this chapter.

Two distinct twisted structures were inspected using scanning transmission electron microscopy (STEM) imaging, as shown in Figure 5.1. The first specimen, as shown in Figure 5.1a, consists of a large base flake with a smaller flake grown on top that is rotated relative to this base. The noticeable contrast difference in the STEM image indicates a significant variation in thickness between the base and top flakes. The second specimen, illustrated in Figure 5.1b, exhibits a twisted spiral-like structure with multiple layers, each slightly twisted with respect to the one below.

To investigate the local electronic properties of these twisted WS$_2$ specimens, spatially-resolved electron energy-loss spectroscopy (EELS) is employed. The acquired spectral images are analyzed using the EELSFITTER framework [34, 35] as reported on in Section 3.2 of Chapter 3.

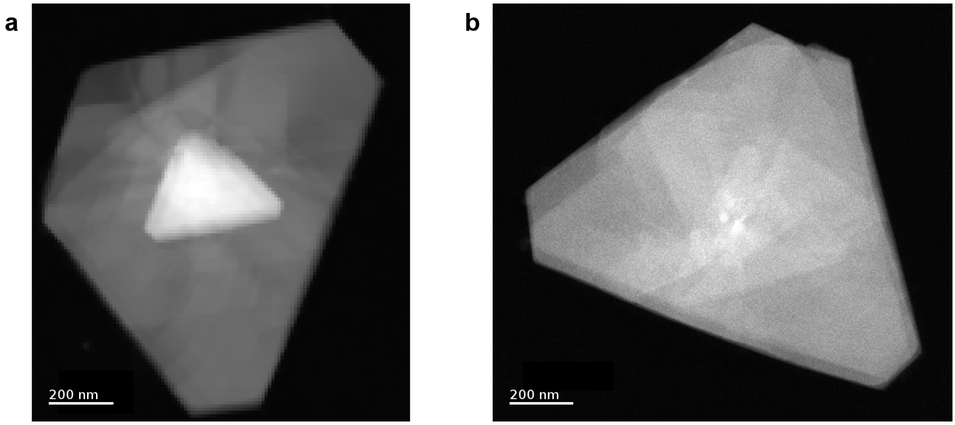

Figure 5.1: Low-magnification STEM images of (a) a WS$_2$ specimen consisting of a stack of two rotated flakes, and (b) a WS$_2$ flake characterized by multiple twisted layers in a spiral-like configuration.

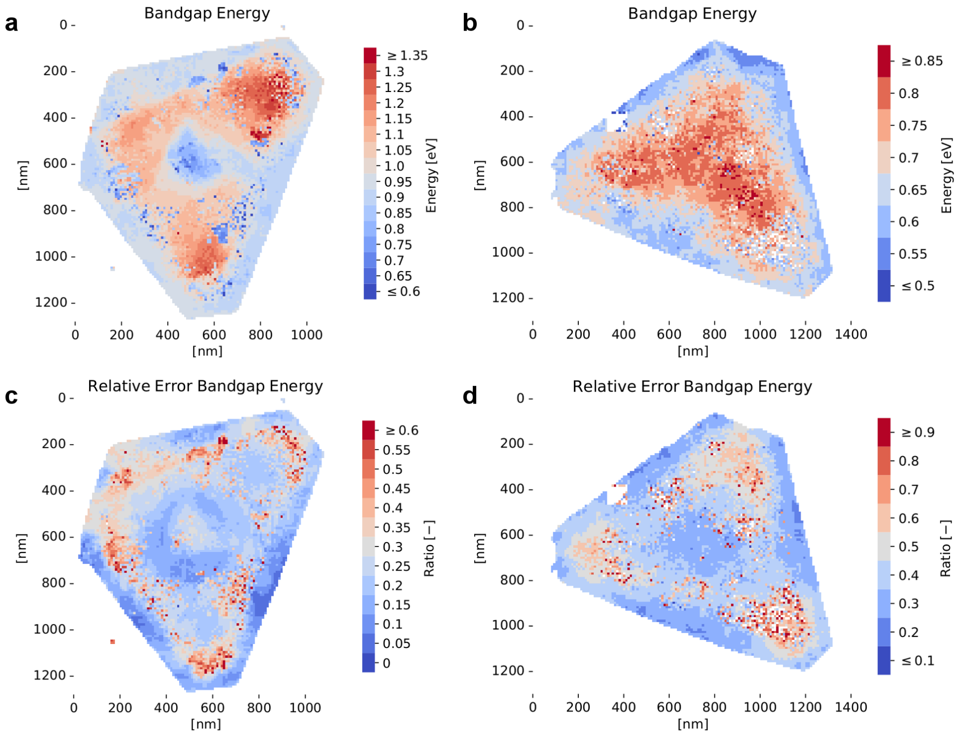

Figure 5.2: (a-b) Spatially-resolved bandgap energy maps corresponding to the specimens in Figures 5.1a and 5.1b, respectively. (c-d) The relative uncertainties (68% confidence level intervals) associated to the bandgap energy maps. A mask has been applied to exclude substrate-only pixels and specimen pixels with a relative uncertainty exceeding 100%.

Figures 5.2a,c and 5.2b,d present the spatially-resolved bandgap energy maps and their corresponding relative uncertainties (68% confidence level intervals) for the specimens shown in Figures 5.1a and 5.1b, respectively. The stacked flakes specimen exhibits an indirect bandgap, with the base flake having a bandgap energy ranging from 0.7 to 1.25 eV (Figure 5.2a) and typical errors varying between 5% and 45% (Figure 5.2c). The bandgap values extracted from the thicker region of the stacked top flake tend to be at the lower end of this range and exhibit lower uncertainties compared to those from the base flake. These bandgap values align with previous reports within the given uncertainties [21, 33].

The bandgap energy in the twisted flake ranges from 0.6 to 0.8 eV (Figure 5.2b), with uncertainties predominantly below 50% (Figure 5.2d), and exhibits a pattern of gradually increasing bandgap values from the outer edges towards the center of the flake. Once again, the bandgap is observed to be indirect.

The relatively large uncertainties in the bandgap energy reported in Figures 5.2c-d in a small subset of pixels, for instance close to the edges, reflect the increased level of fluctuations affecting the subtracted inelastic EEL spectra used for the bandgap fitting, as shown in Section B.1.1 of Appendix B.

To investigate the sensitivity of the bandgap energy to the local thickness of the twisted WS$_2$ specimens depicted in Figure 5.1, we generated the spatially-resolved thickness maps as shown in Figures 5.3a-b using the EELSFITTER framework. These maps offer local insights into the combined thickness of both the specimen and the underlying 5 nm-thick Si$_3$N$_4$ film substrate. The thickness maps for both specimens exhibit negligible uncertainties (at the few-percent level), as shown in Figure B.2 in Appendix B.

To characterize the relationship between specimen thickness and bandgap energy, the mean bandgap energy values are evaluated as a function of the corresponding specimen thickness The results of this evaluation are presented in Figures 5.3c-d. In these graphs, the red dots denote the weighted averages of the mean bandgap values for specific thickness ranges. The 68% confidence level intervals are given in gray and highlight the fluctuations exhibited by the bandgap value at similar thicknesses.

In the stacked flakes specimen these fluctuations are considerable, as seen in Figure 5.3c, suggesting a marked variation in the bandgap energy within the specimen. However, when looking at the weighted averages a well-defined trend emerges. This trend indicates a preference for decreasing bandgap energy with increasing thickness, consistent with previous findings reported in the literature [21, 33].

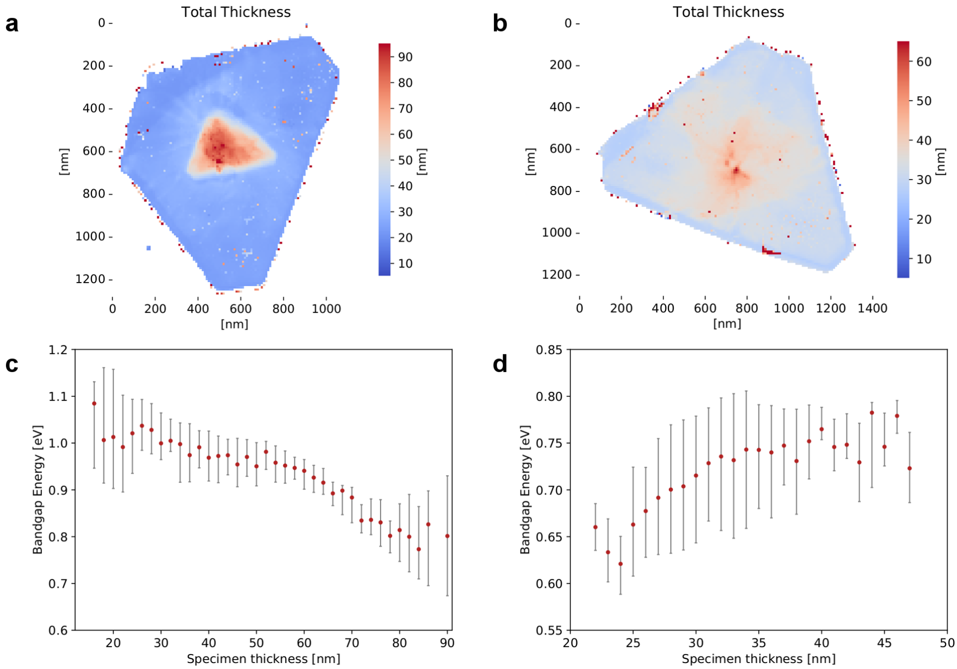

Figure 5.3: (a-b) Spatially-resolved local thickness maps of the specimens depicted in Figures 5.1a and 5.1b, respectively. These maps include the contribution from the underlying 5 nm-thick Si$_3$N$_4$ film substrate. A mask has been applied to exclude substrate-only pixels and specimen pixels with a relative uncertainty exceeding 100%. (c-d) Correlation between specimen thickness and bandgap energy where the data is divided, with regard to the thickness, into bins of (c) 2 nm and (d) 1 nm in size. The red dots represent the weighted averages of the bandgap energy per thickness bin, with 68% confidence level intervals given in gray.

In contrast, the bandgap-thickness correlation analysis of the twisted flake reveals a different trend. Figure 5.3d indicates that the bandgap energy grows from approximately 0.63 eV to around 0.75 eV as the thickness of the specimen increases. Beyond the local thickness, this unanticipated trend hints at other factors influencing the bandgap energy within this twisted flake.

One proposed explanation for this behavior points to the presence of local strain fields in the specimen [17–21, 36–38]. Driven by these findings, we investigate the strain-bandgap relationship by examining the spatially-resolved strain distributions for the specimens depicted in Figure 5.1.

5.3. MAPPING STRAIN DISTRIBUTIONS IN TWISTED WS_2 WITH 4D STEM-EMPAD

The twisted WS_2 specimens studied here exhibit a strain type termed heterostrain. Heterostrain arises when adjacent 2D layers have unequal in-plane strains. In the context of stacking van der Waals materials, heterostrain becomes particularly relevant. A significant challenge in this field is finding a non-invasive method to measure strain in these van der Waals materials quantitatively.

Conventional techniques like geometrical phase analysis (GPA) [39], based on transmission electron microscopy (TEM), have been used to analyze strain in 2D materials [40]. However, they demand atomic-resolution imaging, restricting the field-of-view to mere tens of nanometers. Therefore, using such methods to assess strain fields over an entire micron-sized nanostructure becomes highly challenging.

As discussed in Chapter 3, one can overcome these limitations by leveraging 4D scanning transmission electron microscopy (STEM) paired with an electron microscopy pixel array detector (EMPAD) [41]. Using the acquired 4D nanobeam diffraction datasets, one can extract the relative local intra-layer strain and rigid rotation (or deformation) angles θ through the STRAINMAPPER framework [42], as illustrated in Section 3.3 of Chapter 3.

5.3.1. WS_2 STACKED FLAKES

In Section 3.3.4 of Chapter 3, we illustrated how to extract local strain fields and the rigid rotation from the 4D dataset acquired on a twisted molybdenum-/tungsten diselenide ($MoSe_2$/WSe_2) heterostructure as an example. We now apply this methodology to the stacked flakes specimen shown in Figure 5.1a.

Figure 5.4a depicts the annular dark-field (ADF) STEM image, extracted from the 4D dataset, of the considered area for the analysis. An individual exit-wave power cepstrum (EWPC) pattern corresponding to this specimen is shown in Figure 5.4b. This EWPC pattern was generated by conversion of the nanobeam electron diffraction (NBED) map extracted at the pixel marked by the red dot in Figure 5.4a. In this particular EWPC pattern, six peaks are observed that form a hexagonal arrangement. This hexagonal pattern reflects the characteristic honeycomb lattice structure of WS_2.

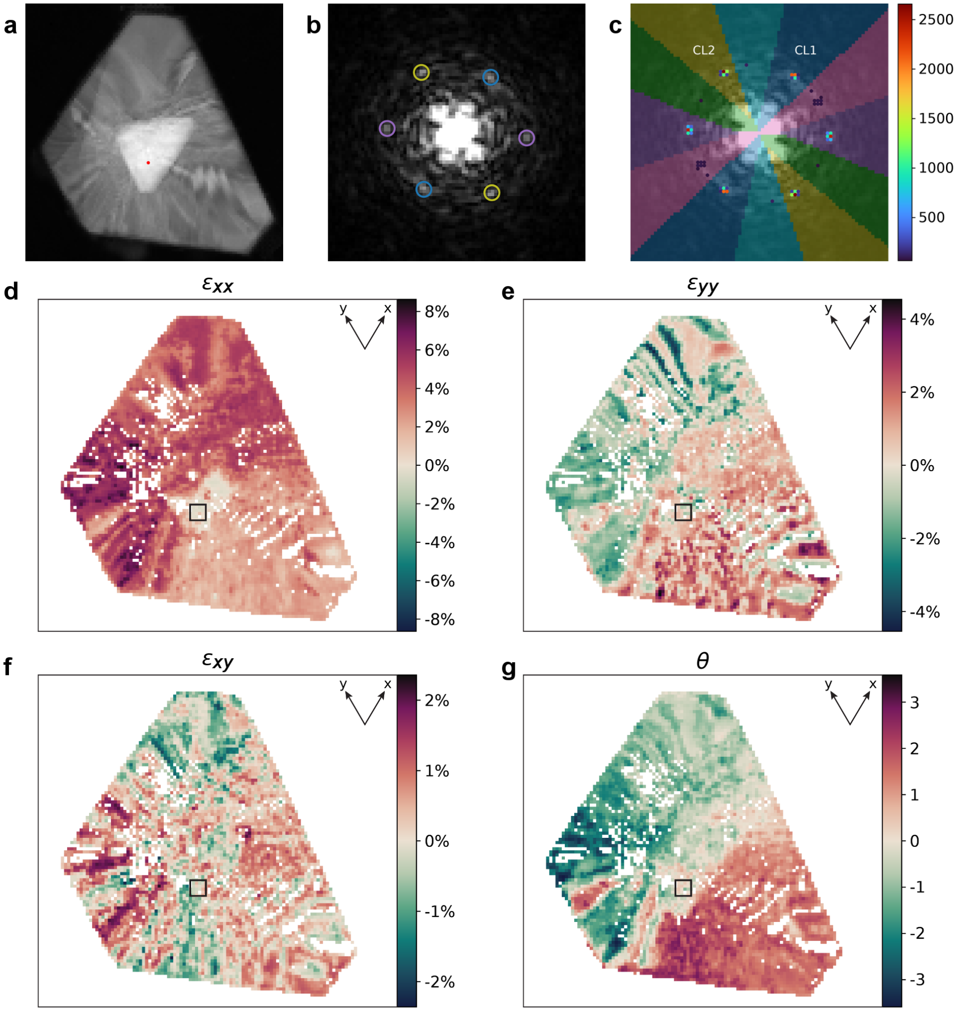

Figure 5.4: (a) ADF-STEM image of the stacked flakes specimen shown in Figure 5.1a as obtained from the 4D STEM-EMPAD dataset. (b) EWPC pattern extracted at the red pixel in (a). A capped linear scale is used to enhance the visualization of the inter-atomic spacing peaks. (c) Weighted point cloud displaying all uniquely tracked peak positions (spots) along with their corresponding weights (color). A threshold was applied to remove all spots found 50 times or less. Colored divisions represent clustering of the point cloud. Spatially-resolved (d-f) strain and (g) deformation angle maps of the specimen obtained using the marked clusters in (c). The strain maps correspond to the ε_{xx}, ε_{yy}, and ε_{xy} components respectively. The reference area is indicated by the black square. The maps were subjected to a Gaussian filter to smooth out outliers.

Tracking the peaks present within the EWPC patterns across the entire specimen yields the weighted point cloud given in Figure 5.4c. In this context, each spot represents a unique peak position, with its color denoting the peak detection frequency. A threshold filter is applied to remove low-frequency spots (≤ 50). As previously touched upon in Section 3.3.4 of Chapter 3, these spots often correspond to erroneously tracked peaks. In this case, those spots include false peaks found within the EWPC patterns corresponding to pixels of the substrate. From Figure 5.4c, we observe that the spots can be grouped into twelve clusters, as indicated by the colored divisions. Of these twelve clusters, six display a much higher population.

To calculate the strain fields and rigid rotation, we must select two clusters. From the previous discussion on the heterostructure (Section 3.3.4 of Chapter 3) it is known that these chosen clusters should be non-parallel and should belong to the same structural element. For this analysis, the selected structural element consists of the dominant set of six peaks arranged in a hexagonal pattern, all corresponding to the same crystal. Thus, we analyze the stacked flakes specimen using the clusters labeled CL1 and CL2 in Figure 5.4c. The vectors associated with the peak positions in these chosen clusters form the basis for the resulting strain fields and deformation angle. Finally, we select the reference area to lie in the region where the second flake overlays the base flake.

The stacked flakes specimen analysis produces the spatially-resolved maps for the strain and deformation angle, shown in Figures 5.4d-g, with the reference area indicated by the black square. The strain maps were decomposed into components along the x- and y-directions, as well as the xy component (shear strain). To improve visualization and reduce pixelation artifacts and outliers, a Gaussian filter was applied to smoothen the maps, with the original maps depicted in Figure B.4 in Appendix B. Occasionally, the strain and deformation angle maps have empty pixels at specific real-space scan positions, signifying that one of the two selected peaks was either untracked or inaccurately tracked.

The maps in Figures 5.4d-f reveal that strain exists across the entire specimen. However, no distinct divisions into specific strain areas can be discerned. On average, the strain seems to distribute relatively uniformly across the specimen. This uniformity is even more apparent when focusing specifically on the shear strain component (ε_{xy}), as illustrated in Figure 5.4f. The relative shear strain values predominantly fall within the approximate range of ± 1.1%.

For a deeper understanding, we conducted a high-angle annular dark-field (HAADF) STEM analysis, showcased in Figures B.7a-c in Appendix B. This analysis confirms that the specimen possesses a pristine crystal structure. For the stacked flakes specimen, as noted earlier, the observed trend in bandgap energy relative to specimen thickness (Figure 5.3c) aligns with prior literature reports [21, 33]. In these documented pristine specimens, thickness is the main influencer of bandgap modification, consistent with our presented findings.

5.3.2. TWISTED WS_2 FLAKE

Subsequently, we performed the same analysis on the twisted flake depicted in Figure 5.1b. Figure 5.5a depicts the ADF-STEM image of the scanned area for this analysis, which is extracted from the 4D dataset. The nanobeam diffraction map obtained at the red dot in Figure 5.5a was transformed into the EWPC pattern shown in Figure 5.5b. Twelve peaks were identified within this specific pattern. Before peak-tracking, the data is masked using the ADF image's contrast to eliminate substrate pixels. Similarly to in Figure 5.4c, a threshold filter is applied to remove low-frequency (≤ 200) spots resulting from any remaining erroneously tracked peaks. The filtered weighted point cloud obtained by tracking the twelve peaks across the specimen is depicted in Figure 5.5c.

In contrast to the stacked flakes specimen, the weighted point cloud clustering of the twisted flake specimen shows a distinct division. A total of twelve distinct clusters were identified, which are visually represented by the colored divisions. Six of these clusters were found to correspond to one region of the flake (A) and the remaining six to the complementary region (B). This division into two distinct regions demands the analysis of the twisted flake specimen to be split. The two regions overlap in a small area, including the pixel selected in Figure 5.5a, which provides a natural choice to define the reference for the strain analysis.

Similar to the analysis conducted for the stacked flakes specimen, for the strain field and rigid rotation calculations two non-parallel clusters have to be selected. Here, the considered clusters are denoted by A.CL1, A.CL2 and B.CL1, B.CL2 in Figure 5.5c for the two regions A and B, respectively. These selected clusters belong to the same set of peaks within the EWPC pattern, ensuring that they provide information about the same structural elements, and each of them represents a complementary region of the specimen. As previously mentioned, the reference area for strain calculation, marked by a black square, was chosen to encompass the region displaying all twelve spots in the EWPC pattern.

Figures 5.5d,f present the spatially-resolved maps for the shear strain (ε_{xy}) and deformation angle (θ) from cluster set A, corresponding to vectors along the x and y directions. While those obtained from cluster set B, corresponding to vectors along the x' and y' directions, are presented in Figures 5.5e,g. The additional strain components (ε_{xx}, ε_{yy}, $\varepsilon_{x'x'}$ and $\varepsilon_{y'y'}$) are provided in Figure B.3 in Appendix B. Similar to the stacked flakes specimen, these maps were subjected to a Gaussian filter for enhanced visualization, with the original maps provided in Figures B.5 and B.6 in Appendix B.

An examination of Figures 5.5d-e indicates a non-uniform strain distribution in this twisted flake, contrasting with the stacked flakes specimen. Regions of both tensile strain, reaching up to 3%, and compressive strain, down to -1.5%, are observed relative to the chosen reference. Notably, abrupt changes in the strain field are found at specific locations, particularly near the three corners of the flake. For example, at the top of the flake, there is a sudden transition to a tensile strain of approximately 1.5% relative to the near-zero strain of the reference area to its right. A similar transition is observed in the right corners, whereas the left corner exhibits a change between low (1.5%) and high (3%) tensile strain values.

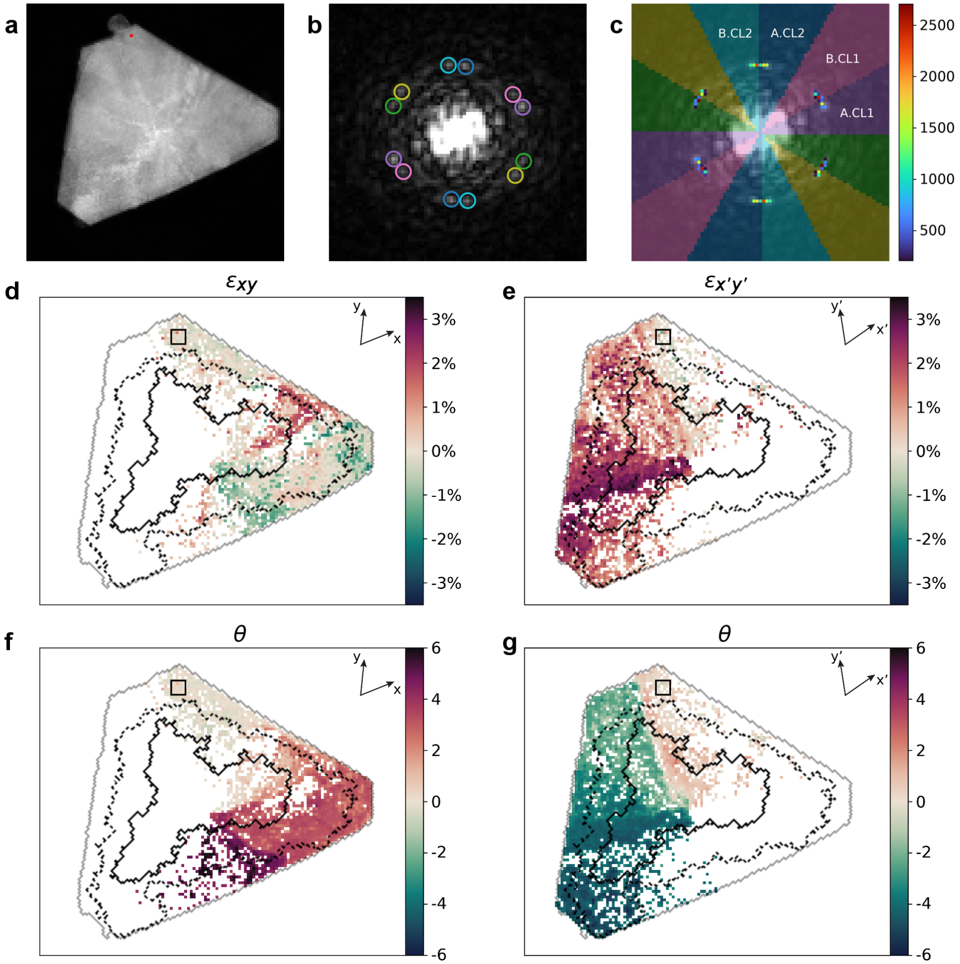

Figure 5.5: (a) ADF-STEM image of the twisted flake shown in Figure 5.1b as obtained from the 4D STEM-EMPAD dataset. (b) EWPC pattern extracted at the red pixel in (a). A capped linear scale is used to enhance the visualization of the inter-atomic spacing peaks. (c) Weighted point cloud displaying all uniquely tracked peak positions (spots) along with their corresponding weights (color). Substrate pixels were excluded from the peak tracking using a mask based on the ADF image's contrast. Additionally, a threshold was applied after peak tracking to remove all spots found 200 times or less. Colored divisions represent clustering of the point cloud. Spatially-resolved (d-e) shear strain and (f-g) deformation angle maps of the specimen obtained using the marked clusters in (c) denoted by (d,f) A and (e,g) B. The reference area is indicated by the black square. The maps were subjected to a Gaussian filter to smooth out the outliers. The overlaid lines outline the contours of the bandgap map of Figure 5.2b, specifically, the crossings at 0.7 eV (dashed black line) and 0.8 eV (solid black line). The outline of the entire flake is represented by the solid gray line.

For the rigid rotation of this twisted flake, we observe a distribution marked by abrupt transitions, as depicted in Figures 5.5f-g. The deformation angles across the twisted flake display a pattern that is characterized by sudden changes, especially near the flake's three corners. At the top of the flake, a transition to roughly −2° is evident when compared to the near-zero rigid rotation in the reference area. In the right corner, we notice a transition in the reverse rotational direction, moving towards approximately 3°. Similarly, at the left corner, there is a transition between low (around −2°) and high (around −5°) rigid rotation values. Overall, the deformation angles mostly fall within the range of ±5°. These results are consistent with previous findings, particularly regarding the non-uniform distribution of strain across bilayer structures and the significant influence of changes in relative rotation angles between layers on these strain fields [22].

5.4. CORRELATION BETWEEN BANDGAP ENERGY AND STRAIN DISTRIBUTION IN TWISTED WS_2 FLAKE

To enhance our understanding of the relationship between bandgap energy and strain distribution in the twisted WS_2 flake, we generated an approximate outline of the constant-energy contours from the bandgap map (Figure 5.2b) and overlaid it on the spatially-resolved maps shown in Figures 5.5d-g. Specifically, the overlay highlights the crossings of the bandgap energy at values of 0.7 eV (dashed black line) and 0.8 eV (solid black line). The outline of the entire flake (solid gray line) is included for reference. This approach highlights the correlation between regions showing abrupt strain variations and deformation angle shifts, and those where the bandgap is intensified. This observation establishes a distinct correlation between the specimen's non-uniform strain distribution and the associated alterations in the bandgap.

Analogous to the stacked flakes specimen, the twisted flake was subjected to a HAADF-STEM analysis presented in Figures B.7d-f in Appendix B. Analyzing the STEM images gave us valuable insights into the crystal structure of the twisted flake. Contrary to pristine ordered planes, the images revealed the presence of Moiré patterns across multiple regions of the specimen. These patterns indicate a deviation from typical crystal characteristics, hinting at potential unconventional behavior within the material.

The detailed analysis of Figure 5.5, together with the bandgap-thickness correlation illustrated in Figure 5.3d, provides compelling evidence establishing the relationship between the local strain field and the bandgap energy in twisted WS_2 flakes. The results suggest that regions within the specimen exhibiting varying local strain fields due to the presence of twisted adjacent layers, demonstrate an enhancement in bandgap energy. This enhancement becomes apparent when compared to a reference specimen of similar thickness but devoid of significant strain field variations. This observed trend is consistent with predicted effects of strain on bandgap energy, where a change of approximately 100 meV per percent of applied strain is anticipated. Further, variations in interlayer coupling due to twist angles and layer separations, as revealed by first-principle density functional theory (DFT) calculations [43], provide additional support for the reported interplay between strain and bandgap modification.

5.5. CONCLUSION

In this comprehensive study, we fingerprinted the interdependent local electronic properties, thickness, and strain fields in twisted and stacked WS_2 flakes, focusing on their cross-correlations, utilizing advanced imaging techniques and computational analysis methods.

In the stacked flakes specimen, we observed a uniform strain distribution across the entire specimen, with a particular emphasis on the shear strain component. This uniformity suggests the preservation of the pristine crystal structure, enabling bandgap energy modification that are primarily driven by local thickness variations. These observations are consistent with the well-established understanding of the relationship between thickness and bandgap modifications in 2D materials.

In stark contrast, the twisted flake showed a non-uniform strain distribution, characterized by localized regions of enhanced strain and abrupt variations. With these strain variations came significant increases in the bandgap energy, dominating the conventional relationship between bandgap and thickness. Remarkably, the bandgap energy in the twisted flake increased by up to 20%. This underlines the significant influence of the deformation angle on the electronic properties. Such unexpected behavior challenges traditional expectations and highlights the immense potential of strain engineering in the emerging field of twistronics.

Furthermore, the presence of Moiré patterns in the twisted flake further emphasized the deviation from the pristine crystal structure. These patterns, which arise from lattice mismatch and rotational misalignment, introduced further complexities. They significantly contribute to the observed unconventional behavior. The intricate relationship between strain variations and Moiré patterns offers a promising direction for investigating novel physical phenomena and designing advanced electronic devices.

This study underscores the importance of non-uniform strain distribution and the pivotal role of deformation angle in modulating the bandgap energy of 2D materials. The capability to precisely control strain fields in twisted flakes paves the way for innovative engineering of their electronic and optical properties. The insights provided in this chapter enrich the growing field of twistronics, shedding light on the complex interplay between strain, bandgap energy, and unconventional behavior in 2D materials.

REFERENCES

[1] Y. Shimazaki, I. Schwartz, K. Watanabe, T. Taniguchi, M. Kroner, and A. Imamoğlu, *Strongly correlated electrons and hybrid excitons in a moiré heterostructure,* Nature **580**, 472 (2020).

[2] W. Yan, L. Meng, Z. Meng, Y. Weng, L. Kang, and X. Li, *Probing Angle-Dependent Interlayer Coupling in Twisted Bilayer WS_2,* The Journal of Physical Chemistry C **123**, 30684 (2019).

[3] F. Wu, T. Lovorn, E. Tutuc, I. Martin, and A. H. MacDonald, *Topological Insulators in Twisted Transition Metal Dichalcogenide Homobilayers,* Physical Review Letters **122**, 086402 (2019).

[4] K. Tran, G. Moody, F. Wu, X. Lu, J. Choi, K. Kim, A. Rai, D. A. Sanchez, J. Quan, A. Singh, J. Embley, A. Zepeda, M. Campbell, T. Autry, T. Taniguchi, K. Watanabe, N. Lu, S. K. Banerjee, K. L. Silverman, S. Kim, E. Tutuc, L. Yang, A. H. MacDonald, and X. Li, *Evidence for moiré excitons in van der Waals heterostructures,* Nature **567**, 71 (2019).

[5] Y. Cao, V. Fatemi, S. Fang, K. Watanabe, T. Taniguchi, E. Kaxiras, and P. Jarillo-Herrero, *Unconventional superconductivity in magic-angle graphene superlattices,* Nature **556**, 43 (2018).

[6] C. R. Dean, L. Wang, P. Maher, C. Forsythe, F. Ghahari, Y. Gao, J. Katoch, M. Ishigami, P. Moon, M. Koshino, T. Taniguchi, K. Watanabe, K. L. Shepard, J. Hone, and P. Kim, *Hofstadter's butterfly and the fractal quantum Hall effect in moiré superlattices,* Nature **497**, 598 (2013).

[7] H. Wang, L. Yu, Y.-H. Lee, Y. Shi, A. Hsu, M. L. Chin, L.-J. Li, M. Dubey, J. Kong, and T. Palacios, *Integrated Circuits Based on Bilayer* MoS_2 *Transistors,* Nano Letters **12**, 4674 (2012).

[8] B. Radisavljevic, A. Radenovic, J. Brivio, V. Giacometti, and A. Kis, *Single-layer* MoS_2 *transistors,* Nature Nanotechnology **6**, 147 (2011).

[9] B. Radisavljevic, M. B. Whitwick, and A. Kis, *Integrated Circuits and Logic Operations Based on Single-Layer* MoS_2*,* ACS Nano **5**, 9934 (2011).

[10] S. R. Tamalampudi, Y.-Y. Lu, R. K. U., R. Sankar, C.-D. Liao, K. M. B., C.-H. Cheng, F. C. Chou, and Y.-T. Chen, *High Performance and Bendable Few-Layered InSe Photodetectors with Broad Spectral Response,* Nano Letters **14**, 2800 (2014).

[11] L. Ye, H. Li, Z. Chen, and J. Xu, *Near-Infrared Photodetector Based on* MoS_2*/Black Phosphorus Heterojunction,* ACS Photonics **3**, 692 (2016).

[12] G. Zhang, S. Huang, A. Chaves, C. Song, V. O. Özçelik, T. Low, and H. Yan, *Infrared fingerprints of few-layer black phosphorus,* Nature Communications **8**, 14071 (2017).

[13] L. Li, J. Kim, C. Jin, G. J. Ye, D. Y. Qiu, F. H. da Jornada, Z. Shi, L. Chen, Z. Zhang, F. Yang, K. Watanabe, T. Taniguchi, W. Ren, S. G. Louie, X. H. Chen, Y. Zhang, and F. Wang, *Direct observation of the layer-dependent electronic structure in phosphorene,* Nature Nanotechnology **12**, 21 (2017).

[14] T. Li and G. Galli, *Electronic Properties of* MoS_2 *Nanoparticles,* The Journal of Physical Chemistry C **111**, 16192 (2007).

[15] S. Zheng, L. Sun, X. Zhou, F. Liu, Z. Liu, Z. Shen, and H. J. Fan, *Coupling and Interlayer Exciton in Twist-Stacked WS_2 Bilayers,* Advanced Optical Materials **3**, 1600 (2015).

[16] K. Liu, L. Zhang, T. Cao, C. Jin, D. Qiu, Q. Zhou, A. Zettl, P. Yang, S. G. Louie, and F. Wang, *Evolution of interlayer coupling in twisted molybdenum disulfide bilayers,* Nature Communications **5**, 4966 (2014).

[17] J. Quereda, P. San-Jose, V. Parente, L. Vaquero-Garzon, A. J. Molina-Mendoza, N. Agraït, G. Rubio-Bollinger, F. Guinea, R. Roldán, and A. Castellanos-Gomez, *Strong Modulation of Optical Properties in Black Phosphorus through Strain-Engineered Rippling,* Nano Letters **16**, 2931 (2016).

[18] Y. Li, T. Wang, M. Wu, T. Cao, Y. Chen, R. Sankar, R. K. Ulaganathan, F. Chou, C. Wetzel, C.-Y. Xu, S. G. Louie, and S.-F. Shi, *Ultrasensitive tunability of the direct bandgap of 2D InSe flakes via strain engineering,* 2D Materials **5**, 021002 (2018).

[19] A. Castellanos-Gomez, R. Roldán, E. Cappelluti, M. Buscema, F. Guinea, H. S. J. van der Zant, and G. A. Steele, *Local Strain Engineering in Atomically Thin MoS_2,* Nano Letters **13**, 5361 (2013).

[20] H. J. Conley, B. Wang, J. I. Ziegler, R. F. Haglund, S. T. Pantelides, and K. I. Bolotin, *Bandgap Engineering of Strained Monolayer and Bilayer MoS_2,* Nano Letters **13**, 3626 (2013).

[21] W. S. Yun, S. W. Han, S. C. Hong, I. G. Kim, and J. D. Lee, *Thickness and strain effects on electronic structures of transition metal dichalcogenides: 2H-MX_2 semiconductors (M = Mo, W; X = S, Se, Te),* Physical Review B **85**, 033305 (2012).

[22] H. Kumar, D. Er, L. Dong, J. Li, and V. B. Shenoy, *Elastic Deformations in 2D van der waals Heterostructures and their Impact on Optoelectronic Properties: Predictions from a Multiscale Computational Approach,* Scientific Reports **5**, 10872 (2015).

[23] C. R. Woods, L. Britnell, A. Eckmann, R. S. Ma, J. C. Lu, H. M. Guo, X. Lin, G. L. Yu, Y. Cao, R. V. Gorbachev, A. V. Kretinin, J. Park, L. A. Ponomarenko, M. I. Katsnelson, Y. N. Gornostyrev, K. Watanabe, T. Taniguchi, C. Casiraghi, H.-J. Gao, A. K. Geim, and K. S. Novoselov, *Commensurate–incommensurate transition in graphene on hexagonal boron nitride,* Nature Physics **10**, 451 (2014).

[24] S. Tang, H. Wang, Y. Zhang, A. Li, H. Xie, X. Liu, L. Liu, T. Li, F. Huang, X. Xie, and M. Jiang, *Precisely aligned graphene grown on hexagonal boron nitride by catalyst free chemical vapor deposition,* Scientific Reports **3**, 2666 (2013).

[25] K. Roy, M. Padmanabhan, S. Goswami, T. P. Sai, G. Ramalingam, S. Raghavan, and A. Ghosh, *Graphene–MoS_2 hybrid structures for multifunctional photoresponsive memory devices,* Nature Nanotechnology **8**, 826 (2013).

[26] H. Fang, C. Battaglia, C. Carraro, S. Nemsak, B. Ozdol, J. S. Kang, H. A. Bechtel, S. B. Desai, F. Kronast, A. A. Unal, G. Conti, C. Conlon, G. K. Palsson, M. C. Martin, A. M. Minor, C. S. Fadley, E. Yablonovitch, R. Maboudian, and A. Javey, *Strong interlayer coupling in van der Waals heterostructures built from single-layer chalcogenides,* Proceedings of the National Academy of Sciences **111**, 6198 (2014).

[27] P. Ci, Y. Zhao, M. Sun, Y. Rho, Y. Chen, C. P. Grigoropoulos, S. Jin, X. Li, and J. Wu, *Breaking Rotational Symmetry in Supertwisted WS_2 Spirals via Moiré Magnification of Intrinsic Heterostrain,* Nano Letters **22** (9027–9035), 10.1021/acs.nanolett.2c03347.

[28] N. C. H. Hesp, I. Torre, D. Rodan-Legrain, P. Novelli, Y. Cao, S. Carr, S. Fang, P. Stepanov, D. Barcons-Ruiz, H. Herzig Sheinfux, K. Watanabe, T. Taniguchi, D. K. Efetov, E. Kaxiras, P. Jarillo-Herrero, M. Polini, and F. H. L. Koppens, *Observation of interband collective excitations in twisted bilayer graphene,* Nature Physics **17**, 1162 (2021).

[29] Y. Jiang, X. Lai, K. Watanabe, T. Taniguchi, K. Haule, J. Mao, and E. Y. Andrei, *Charge order and broken rotational symmetry in magic-angle twisted bilayer graphene,* Nature **573**, 91 (2019).

[30] L. Huder, A. Artaud, T. Le Quang, G. T. de Laissardière, A. G. M. Jansen, G. Lapertot, C. Chapelier, and V. T. Renard, *Electronic Spectrum of Twisted Graphene Layers under Heterostrain,* Physical Review Letters **120**, 156405 (2018).

[31] C. Zhang, M.-Y. Li, J. Tersoff, Y. Han, Y. Su, L.-J. Li, D. A. Muller, and C.-K. Shih, *Strain distributions and their influence on electronic structures of WSe_2–MoS_2 laterally strained heterojunctions,* Nature Nanotechnology **13**, 152 (2018).

[32] K. Li, F. Xiao, W. Guan, Y. Xiao, C. Xu, J. Zhang, C. Lin, D. Li, Q. Tong, S.-Y. Li, and A. Pan, *Morphology Deformation and Giant Electronic Band Modulation in Long-Wavelength WS_2 Moiré Superlattices,* Nano Letters **22**, 5997 (2022).

[33] A. Kuc, N. Zibouche, and T. Heine, *Influence of quantum confinement on the electronic structure of the transition metal sulfide TS_2,* Physical Review B **83**, 245213 (2011).

[34] L. I. Roest, S. E. van Heijst, L. Maduro, J. Rojo, and S. Conesa-Boj, *Charting the low-loss region in electron energy loss spectroscopy with machine learning,* Ultramicroscopy **222**, 113202 (2021).

[35] A. Brokkelkamp, J. ter Hoeve, I. Postmes, S. E. van Heijst, L. Maduro, A. V. Davydov, S. Krylyuk, J. Rojo, and S. Conesa-Boj, *Spatially Resolved Band Gap and Dielectric Function in Two-Dimensional Materials from Electron Energy Loss Spectroscopy,* The Journal of Physical Chemistry A **126**, 1255 (2022).

[36] S. H. Sung, N. Schnitzer, L. Brown, J. Park, and R. Hovden, *Stacking, strain, and twist in 2D materials quantified by 3D electron diffraction,* Physical Review Materials **3**, 064003 (2019).

[37] F. Miao, S.-J. Liang, and B. Cheng, *Straintronics with van der Waals materials,* npj Quantum Materials **6**, 59 (2021).

[38] S. Zhu and H. T. Johnson, *Moiré-templated strain patterning in transition-metal dichalcogenides and application in twisted bilayer* MoS_2*,* Nanoscale **10**, 20689 (2018).

[39] J. L. Rouvière and E. Sarigiannidou, *Theoretical discussions on the geometrical phase analysis,* Ultramicroscopy **106**, 1 (2005).

[40] M. Tinoco, L. Maduro, M. Masaki, E. Okunishi, and S. Conesa-Boj, *Strain-Dependent Edge Structures in* MoS_2 *Layers,* Nano Letters **17**, 7021 (2017).

[41] M. C. Cao, Y. Han, Z. Chen, Y. Jiang, K. X. Nguyen, E. Turgut, G. D. Fuchs, and D. A. Muller, *Theory and practice of electron diffraction from single atoms and extended objects using an EMPAD,* Microscopy **67**, i150 (2017).

[42] M. Bolhuis, S. E. van Heijst, J. J. M. Sangers, and S. Conesa-Boj, *4D-STEM Nanoscale Strain Analysis in van der Waals Materials: Advancing beyond Planar Configurations,* Small Science **4**, 2300249 (2024).

[43] P. Johari and V. B. Shenoy, *Tuning the Electronic Properties of Semiconducting Transition Metal Dichalcogenides by Applying Mechanical Strains,* ACS Nano **6**, 5449 (2012).

6

CONCLUSION AND OUTLOOK

TRANSITION metal dichalcogenides (TMDs) have been and will likely continue to be extensively investigated in the field of materials science. This is due to their remarkable chemical and physical properties and the unique tunability of these properties through their structural arrangement.

Our work, especially Chapters 4 and 5, provides insights into the understanding of the interplay between structural and physical properties in intricate tungsten disulfide (WS_2) nanostructures obtained via characterization with complementary transmission electron microscopy (TEM) techniques. The bottom-up fabrication method of chemical vapor deposition (CVD) allowed for the creation of these nanostructures with unique structural properties, including exposed edges and intriguing lateral arrangements in the form of polytypism and twisted layers. With the work presented in this thesis, we lay the foundational work in the quest to design novel nanostructures with tailored functionalities. However, some questions remain. In the following sections, we address some of these remaining open questions and provide perspectives on further research opportunities for these intricate nanostructures, both in this work and beyond.

First, we will focus on the WS_2 flower-like nanostructures exhibiting a mixed 2H/3R polytypism. We presented an extensive study of the structural and local electronic properties of these polytypic WS_2 nanoflowers (Chapter 4). In addition to the electronic properties explored in this thesis, the linear optical response of these polytypic WS_2 nanoflowers was investigated also [1]. The observed reduced photoluminescence proved ideal for studying the intricacies of the Raman signal. On the other hand, the nonlinear optical response remains to be explored. It has been reported that crystal structures possessing a broken inversion symmetry exhibit enhanced nonlinear behavior [2, 3]. Hence, the mixed 2H/3R polytype could be especially interesting for nonlinear optics.

Another potential avenue to explore for these polytypic WS_2 nanoflower structures is their performance as catalyst towards the hydrogen evolution reaction (HER). The interest in this specific chemical process is twofold. Firstly, the nanoflowers possess a vast amount of exposed edges. As mentioned previously, these edges have been shown to act as active sites for HER and other chemical reactions [4–8]. Structures with a high ratio of edges have been observed to exhibit enhanced catalytic performance as a result [6, 7, 9]. Hence, the WS_2 nanoflowers are promising candidates for improved catalytic performance based on their edge-richness. Secondly, the nanoflowers were revealed to possess a 2H/3R phase. Previous work by Toh *et al.* [10] reported on the relation between the HER catalytic properties of molybdenum disulfide (MoS_2) and WS_2 and their polytypes. Indeed, they discovered that the 3R phase outperformed the 2H phase. This raises the question of what a mixed polytypism would contribute to the HER performance of nanostructures.

Similarly, the application of polytypic WS_2 nanoflowers for gas sensing purposes or as a catalyst towards carbon dioxide reduction could be investigated. Both of these applications have been shown to benefit from an increased number of exposed edges [7–9]. Improved carbon dioxide reduction has even been observed for the nanoflower morphology in particular [9]. Herein, a sensitivity of the catalytic behavior to the possessed polytype was also hinted at.

Lastly, one could investigate the field-emission properties of the polytypic WS_2 nanoflowers. Previous work has shown that MoS_2 and WS_2 possessing a nanoflower morphology are well-suited for field emitter applications [11–13]. However, to the best of our knowledge, the influence of the stacking sequence on the field-emission properties in these TMDs has yet to be explored.

Likewise, the structural properties of twisted WS_2 specimens also open up interesting research opportunities. In Chapter 5, we conducted a comprehensive investigation into the relationship between local thickness, electronic properties, and strain within various twisted WS_2 specimens. Specifically, two types of structures were examined: *1)* a well-aligned structure composed of two multilayer flakes, and *2)* a structure displaying a spiral-like configuration where each layer is slightly twisted relative to the adjacent ones.

In the well-aligned stacked flakes specimen, we observed conventional behavior regarding the bandgap energy as a function of local thickness. Additionally, uniform strain fields were observed, suggesting the preservation of a pristine crystal structure in this stacked specimen. It is important to note that these observations are likely to change if this structure was instead composed of two flakes of different TMD materials. Such a structure is known as a heterostructure, and they have been shown to possess unique optoelectronic properties beyond those of the individual TMD materials from which they are composed [14–19]. In addition, due to the vast variety of different TMDs, these properties can be further tuned by selecting the materials that compose the heterostructure. Hence, TMD heterostructures provide a powerful method by which to design novel structures with tailored functionalities.

Heterostructures can be fabricated in various ways. The most well-known method is the manual stacking of the layers using mechanical transfer techniques [14, 20, 21]. However, despite the lattice mismatch between different TMD materials, it has been discovered that TMD heterostructures can also be epitaxially grown using CVD [16–19, 22] due to the weak van der Waals interactions between the layers and/or flakes. It is important to emphasize here that the lattice mismatch within CVD-grown TMD heterostructures can cause strain [22], which in turn may further affect the properties of these heterostructures. This latter fact also makes these heterostructures uniquely interesting to investigate using the synergistic methodology discussed in Chapter 5.

The second type of structure studied in Chapter 5 had a spiral-like configuration. This structure exhibit an unconventional relationship between thickness and bandgap due to non-uniform strain present within it. In addition to the study of structural and local electronic properties in the presence of strain, these twisted spiral-like WS_2 structures might also prove interesting for applications in nonlinear optics. As discussed previously for the WS_2 nanoflowers, an absence of inversion symmetry can lead to enhanced nonlinear optical response. This broken inversion symmetry and corresponding enhanced nonlinear optical response have also been reported in twisted spiral-like TMD morphologies [23]. Investigating whether our structures also possess this broken inversion symmetry and thus an enhanced nonlinear optical response could open doors for various applications.

Another potential application for the twisted spiral-like WS_2 structures lies in field-effect transistors (FETs). Research by Chen *et al.* [24] revealed that spiraling pyramid-like tungsten diselenide (WSe_2) structures could be used to fabricated FETs. The device performance of these FETs was favorably comparable with FETs created from few-layer WSe_2. It is important to emphasize that these WSe_2 structures were composed of aligned layers. In contrast, our structures exhibit natural twisting of the adjacent layers. This twist angle provides an additional degree of tunability of the electron mobility [24, 25], as mentioned earlier. Hence, the combination of the spiral-like configuration and the natural twist makes these twisted spiral-like WS_2 structures ideal candidates for investigating FET performance.

As seen from the above discussion and the work presented in the thesis, the fabrication of novel nanostructures with unique structural properties yields various new insights and opens the door to even more science. However, the bottom-up CVD fabrication of these types of nanostructures possessing a mixed polytype or twisted layers is relatively challenging. Specifically, the precise control of these unique lateral arrangements is difficult to achieved. A good example of this has already been shown within this work, as the experiment yielding twisted WS_2 nanostructures provided us with a variety of different morphologies within these twisted structures. Hence, highlighting the importance for future research to strive for improved control. In closing, we would like to provide some perspectives on ways to achieve this goal.

The first method is specifically applicable to the fabrication of the twisted WS_2 specimens. As stated prior, the same experimental conditions led to the synthesis of a variety of different twisted morphologies. It is important to recall that as a first step in the fabrication of these structure, we deposited tungsten trioxide (WO_3) powder on our substrate. To do this, we suspended the WO_3 powder in isopropanol (ISO) and subsequently deposited a few droplets of this mixture on our substrate, where it was left to dry. One drawback of this method is that it is unlikely to result in a fully uniform coating of the WO_3 precursor. Importantly, literature reports on the precursor concentration being key in determining the growth mechanism by which few-layer pyramid-like morphologies grow [26, 27]. Hence, it can be hypothesized that our method of WO_3 deposition results in local variations in precursor concentration, consequently yielding the various structures observed within this experiment. In order to gain control over the type of morphology grown during the experiment, one should thus explore different methods to coat the substrate with WO_3. This method should provide better uniformity of the precursor, but care must also be taken that the desired structures are still obtained. For instance, the sulfurization of a WO_3 thin film is more likely to yield WS_2 monolayers instead.

Beyond determining the type of twisted WS_2 nanostructures to be grown, one can also propose methods by which the twist angle could be controlled. Zhao *et al.* [28] suggested that the twist in such structures occurs due to protrusions on the substrate. Hence, twist angle manipulation might be attainable through controlled manipulation, for example via nanofabrication, of the substrate morphology.

If we instead take a step back from these specific structures and look at methods by which control of twist and stacking can be achieved in general, various more routes could be proposed. Beyond the further optimization of the parameters involved in CVD, one could look to combine CVD with other techniques. One of which that has been mentioned before is the manual stacking of the layers using mechanical transfer techniques such as stamping. Manual stacking of CVD-grown nanosheets by stamping allows for the precise control of both twist angle and position of these nanosheets. As a result, homo- and heterostructure can be created with a higher degree of control than is currently possible with CVD. However, stamping still also comes with challenges. Despite the control offered, predetermined stacking sequences might still be difficult to obtain as the atomic scale arrangement of the nanosheets to be stacked cannot be known fully. Commonly, assumptions are made based on the most stable configuration.

Alternatively, Carr *et al.* [29] proposes the use of intercalants, in this specific case, lithium (Li) ions, to controllably induce a relative twist between two layer of graphene. They revealed through theoretical calculations that in a fully lithiated structure of bilayer graphene, the relative stability of the stacking sequences (AA and AB) were inverted. It would be interesting to see if this could be exploited experimentally in fabrication processes to facilitate the growth of predetermined stacking sequences.

By achieving the desired improved control over the unique structural properties of polytypism and twist in TMDs, we believe nanostructure exhibiting these properties could reach their full potential. Unlocking this potential will facilitate their application in efficient and high performance devices in the fields of optics, electronics and renewability, playing their part in revolutionizing the world of nanodevices.

REFERENCES

[1] I. Komen, S. E. van Heijst, M. Caldarola, S. Conesa-Boj, and L. Kuipers, *Revealing the nanogeometry of WS_2 nanoflowers by polarization-resolved Raman spectroscopy,* Journal of Applied Physics **132**, 173103 (2022).

[2] J. Shi, P. Yu, F. Liu, P. He, R. Wang, L. Qin, J. Zhou, X. Li, J. Zhou, X. Sui, S. Zhang, Y. Zhang, Q. Zhang, T. C. Sum, X. Qiu, Z. Liu, and X. Liu, *3R MoS_2 with Broken Inversion Symmetry: a Promising Ultrathin Nonlinear Optical Device,* Advanced Materials **29**, 1701486 (2017).

[3] Z. Zeng, X. Sun, D. Zhang, W. Zheng, X. Fan, M. He, T. Xu, L. Sun, X. Wang, and A. Pan, *Controlled Vapor Growth and Nonlinear Optical Applications of Large-Area 3R Phase WS_2 and WSe_2 Atomic Layers,* Advanced Functional Materials **29**, 1806874 (2019).

[4] T. F. Jaramillo, K. P. Jorgensen, J. Bonde, J. H. Nielsen, S. Horch, and I. Chorkendorff, *Identification of Active Edge Sites for Electrochemical H_2 Evolution from MoS_2 Nanocatalysts,* Science **317**, 100 (2007).

[5] J. Kibsgaard, Z. Chen, B. N. Reinecke, and T. F. Jaramillo, *Engineering the surface structure of MoS_2 to preferentially expose active edge sites for electrocatalysis,* Nature Materials **11**, 963 (2012).

[6] H. Wang, Q. Zhang, H. Yao, Z. Liang, H.-W. Lee, P.-C. Hsu, G. Zheng, and Y. Cui, *High Electrochemical Selectivity of Edge versus Terrace Sites in Two-Dimensional Layered* MoS_2 *Materials,* Nano Letters **14**, 7138 (2014).

[7] S.-Y. Cho, S. J. Kim, Y. Lee, J.-S. Kim, W.-B. Jung, H.-W. Yoo, J. Kim, and H.-T. Jung, *Highly Enhanced Gas Adsorption Properties in Vertically Aligned* MoS_2 *Layers,* ACS Nano **9**, 9314 (2015).

[8] M. Asadi, B. Kumar, A. Behranginia, B. A. Rosen, A. Baskin, N. Repnin, D. Pisasale, P. Phillips, W. Zhu, R. Haasch, R. F. Klie, P. Král, J. Abiade, and A. Salehi-Khojin, *Robust carbon dioxide reduction on molybdenum disulphide edges,* Nature Communications **5**, 4470 (2014).

[9] A. J. Meier, A. Garg, B. Sutter, J. N. Kuhn, and V. R. Bhethanabotla, MoS_2 *Nanoflowers as a Gateway for Solar-Driven* CO_2 *Photoreduction,* ACS Sustainable Chemistry & Engineering **7**, 265 (2019).

[10] R. J. Toh, Z. Sofer, J. Luxa, D. Sedmidubský, and M. Pumera, *3R phase of* MoS_2 *and* WS_2 *outperforms the corresponding 2H phase for hydrogen evolution,* Chemical Communications **53**, 3054 (2017).

[11] X. Li, J. Ge, and Y. Li, *Atmospheric Pressure Chemical Vapor Deposition: An Alternative Route to Large-Scale* MoS_2 *and* WS_2 *Inorganic Fullerene-like Nanostructures and Nanoflowers,* Chemistry – A European Journal **10**, 6163 (2004).

[12] Y. B. Li, Y. Bando, and D. Golberg, MoS_2 *nanoflowers and their field-emission properties,* Applied Physics Letters **82**, 1962 (2003).

[13] F. Giubileo, A. Grillo, M. Passacantando, F. Urban, L. Iemmo, G. Luongo, A. Pelella, M. Loveridge, L. Lozzi, and A. Di Bartolomeo, *Field Emission Characterization of* MoS_2 *Nanoflowers,* Nanomaterials **9**, 717 (2019).

[14] S. Tongay, W. Fan, J. Kang, J. Park, U. Koldemir, J. Suh, D. S. Narang, K. Liu, J. Ji, J. Li, R. Sinclair, and J. Wu, *Tuning Interlayer Coupling in Large-Area Heterostructures with CVD-Grown* MoS_2 *and* WS_2 *Monolayers,* Nano Letters **14**, 3185 (2014).

[15] H. Terrones, F. López-Urías, and M. Terrones, *Novel hetero-layered materials with tunable direct band gaps by sandwiching different metal disulfides and diselenides,* Scientific Reports **3**, 1549 (2013).

[16] Z. Cai, B. Liu, X. Zou, and H.-M. Cheng, *Chemical Vapor Deposition Growth and Applications of Two-Dimensional Materials and Their Heterostructures,* Chemical Reviews **118**, 6091 (2018).

[17] J. Zhang, J. Wang, P. Chen, Y. Sun, S. Wu, Z. Jia, X. Lu, H. Yu, W. Chen, J. Zhu, G. Xie, R. Yang, D. Shi, X. Xu, J. Xiang, K. Liu, and G. Zhang, *Observation of Strong Interlayer Coupling in* MoS_2/WS_2 *Heterostructures,* Advanced Materials **28**, 1950 (2016).

[18] Y. Gong, J. Lin, X. Wang, G. Shi, S. Lei, Z. Lin, X. Zou, G. Ye, R. Vajtai, B. I. Yakobson, H. Terrones, M. Terrones, B. K. Tay, J. Lou, S. T. Pantelides, Z. Liu, W. Zhou, and P. M. Ajayan, *Vertical and in-plane heterostructures from WS_2/MoS_2 monolayers,* Nature Materials **13**, 1135 (2014).

[19] Y. Yu, S. Hu, L. Su, L. Huang, Y. Liu, Z. Jin, A. A. Purezky, D. B. Geohegan, K. W. Kim, Y. Zhang, and L. Cao, *Equally Efficient Interlayer Exciton Relaxation and Improved Absorption in Epitaxial and Nonepitaxial MoS_2/WS_2 Heterostructures,* Nano Letters **15**, 486 (2015).

[20] S. Fan, Q. A. Vu, M. D. Tran, S. Adhikari, and Y. H. Lee, *Transfer assembly for two-dimensional van der Waals heterostructures,* 2D Materials **7**, 022005 (2020).

[21] A. Castellanos-Gomez, M. Buscema, R. Molenaar, V. Singh, L. Janssen, H. S. Van Der Zant, and G. A. Steele, *Deterministic transfer of two-dimensional materials by all-dry viscoelastic stamping,* 2D Materials **1**, 011002 (2014).

[22] J. M. Woods, Y. Jung, Y. Xie, W. Liu, Y. Liu, H. Wang, and J. J. Cha, *One-Step Synthesis of MoS_2/WS_2 Layered Heterostructures and Catalytic Activity of Defective Transition Metal Dichalcogenide Films,* ACS Nano **10**, 2004 (2016).

[23] X. Fan, Y. Jiang, X. Zhuang, H. Liu, T. Xu, W. Zheng, P. Fan, H. Li, X. Wu, X. Zhu, Q. Zhang, H. Zhou, W. Hu, X. Wang, L. Sun, X. Duan, and A. Pan, *Broken Symmetry Induced Strong Nonlinear Optical Effects in Spiral WS_2 Nanosheets,* ACS Nano **11**, 4892 (2017).

[24] L. Chen, B. Liu, A. N. Abbas, Y. Ma, X. Fang, Y. Liu, and C. Zhou, *Screw-Dislocation-Driven Growth of Two-Dimensional Few-Layer and Pyramid-like WSe_2 by Sulfur-Assisted Chemical Vapor Deposition,* ACS Nano **8**, 11543 (2014).

[25] M. Liao, Z. Wei, L. Du, Q. Wang, J. Tang, H. Yu, F. Wu, J. Zhao, X. Xu, B. Han, K. Liu, P. Gao, T. Polcar, Z. Sun, D. Shi, R. Yang, and G. Zhang, *Precise control of the interlayer twist angle in large scale MoS_2 homostructures,* Nature Communications **11**, 2153 (2020).

[26] P. V. Sarma, P. D. Patil, P. K. Barman, R. N. Kini, and M. M. Shaijumon, *Controllable growth of few-layer spiral WS_2,* RSC Advances **6**, 376 (2016).

[27] X. Fan, Y. Zhao, W. Zheng, H. Li, X. Wu, X. Hu, X. Zhang, X. Zhu, Q. Zhang, X. Wang, B. Yang, J. Chen, S. Jin, and A. Pan, *Controllable Growth and Formation Mechanisms of Dislocated WS_2 Spirals,* Nano Letters **18**, 3885 (2018).

[28] Y. Zhao, C. Zhang, D. D. Kohler, J. M. Scheeler, J. C. Wright, P. M. Voyles, and S. Jin, *Supertwisted spirals of layered materials enabled by growth on non-Euclidean surfaces,* Science **370**, 442 (2020).

[29] S. Carr, D. Massatt, S. Fang, P. Cazeaux, M. Luskin, and E. Kaxiras, *Twistronics: Manipulating the electronic properties of two-dimensional layered structures through their twist angle,* Physical Review B **95**, 075420 (2017).

A

SUPPLEMENTARY MATERIALS TO CHAPTER 4

Parts of this chapter have been published as the supplementary information of *Annalen der Physik* **533**, 2000499 (2021) by **S. E. van Heijst**, M. Mukai, E. Okunishi, H. Hashiguchi, L. I. Roest, L. Maduro, J. Rojo, and S. Conesa-Boj.

A.1. STACKING SEQUENCES IN TMD MATERIALS

Transition metal dichalcogenide (TMD) materials exist in multiple polytypes, each of which is characterized by a unique stacking sequence. Two of these polytypes are 2H and 3R, using a convention where the number denotes the number of layers in the unit cell and the letter describes the crystallographic structure. In the monolayer limit, no difference can be observed between the hexagonal (2H) and rhombohedral (3R) crystal structures. The reason is that for both polytypes the monolayer is composed of a transition metal atomic layer sandwiched between two chalcogen atomic layers.

The differences between the two polytypes become apparent for bilayer stacking (Figure A.1). For the 2H polytype, the second layer is rotated 60° along the *c*-axis relative to the first layer, and shifted so the transition metal (chalcogen) atoms of the second layer are positioned above the chalcogen (transition metal) atoms of the first layer. This stacking sequence, AA', is depicted in Figure A.1a and possesses inversion symmetry. For the case of the 3R bilayer stacking, the second layer is not rotated but there is a shift in the position which places the chalcogen atoms of the second layer above the transition metal atoms of the first layer such that the resulting stacking sequence becomes AB. The 3R bilayer stacking is shown in Figure A.1b and one observes how here the inversion symmetry, which characterized the 2H phase, is now broken.

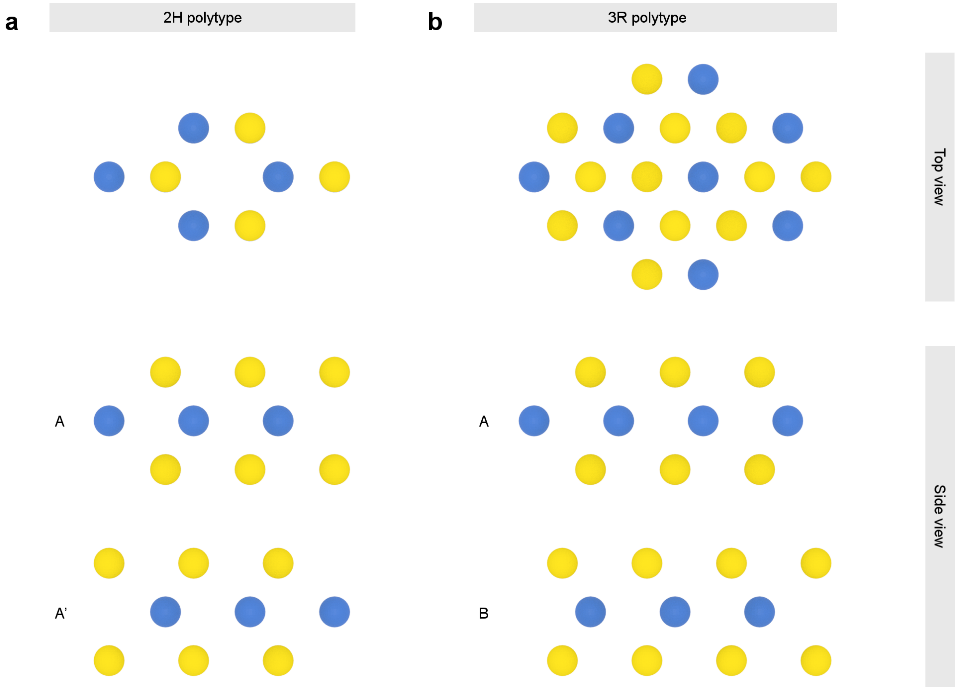

Figure A.1: Schematic atomic model of the top-view (upper panels) and side-view (lower panels) of the bilayer crystalline structure associated to the (a) 2H and (b) 3R polytypes. Here the tungsten atoms are indicated in blue and the sulfur atoms in yellow.

A.2. CRYSTALLINE STRUCTURE OF THE WS_2 NANOFLOWERS

Figure A.2a displays a low-magnification annular dark-field (ADF) scanning transmission electron microscopy (STEM) image of one representative tungsten disulfide (WS_2) petal. The difference in contrast indicates the difference terraces. Figures A.2b-d show the corresponding high-resolution ADF-STEM images taken at different regions of this WS_2 petal. As can be seen from Figures A.2c-d, the transition region between terraces exhibits the same atomic arrangement as the terraces themselves, namely a hexagonal honeycomb with an atom in its center. To further confirm the specific crystallographic structure of the various regions studied for this petal, ADF line profiles have been taken at the different locations marked in Figure A.3a. Note that these profiles cover both single terraces and the interface region between different terraces. In all cases, the characteristic three-fold periodicity is clearly observed from them (Figures A.3b-d), highlighting the presence of the 2H/3R polytype.

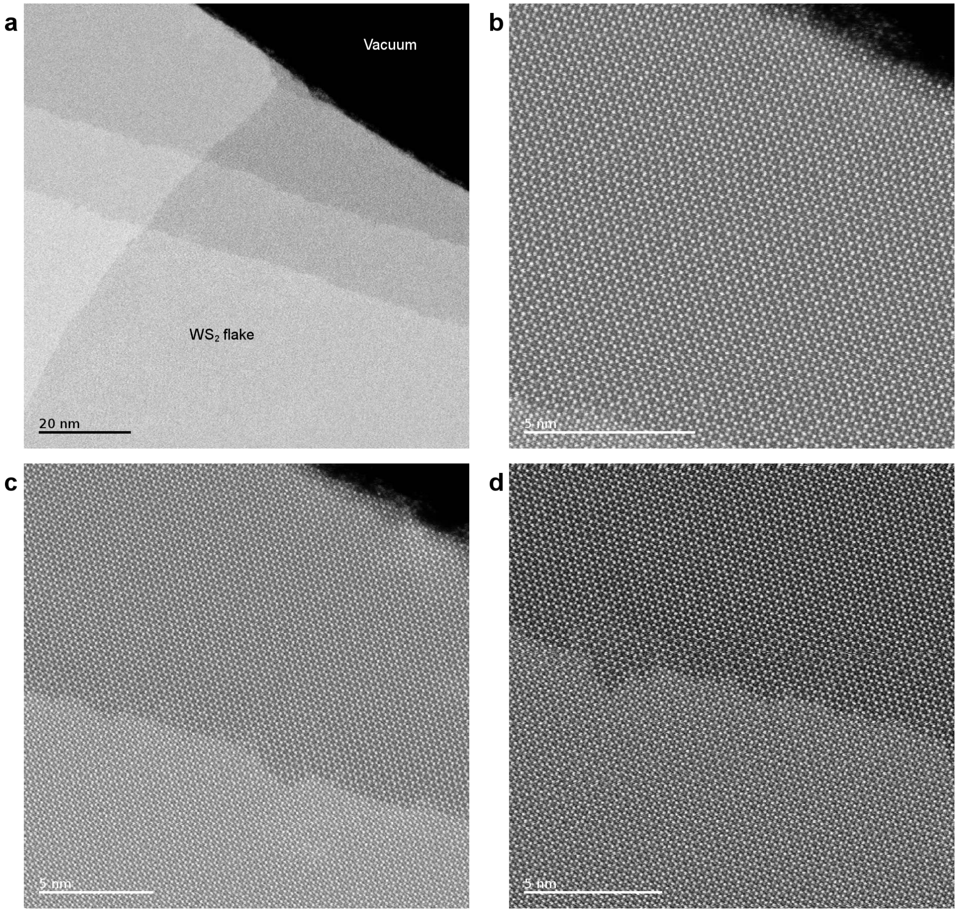

Figure A.2: (a) Low-magnification ADF-STEM image of a representative WS_2 petal. The difference in contrast indicates terraces of different thicknesses. (b-d) The corresponding high-resolution ADF-STEM measurements acquired at different areas of this flake.

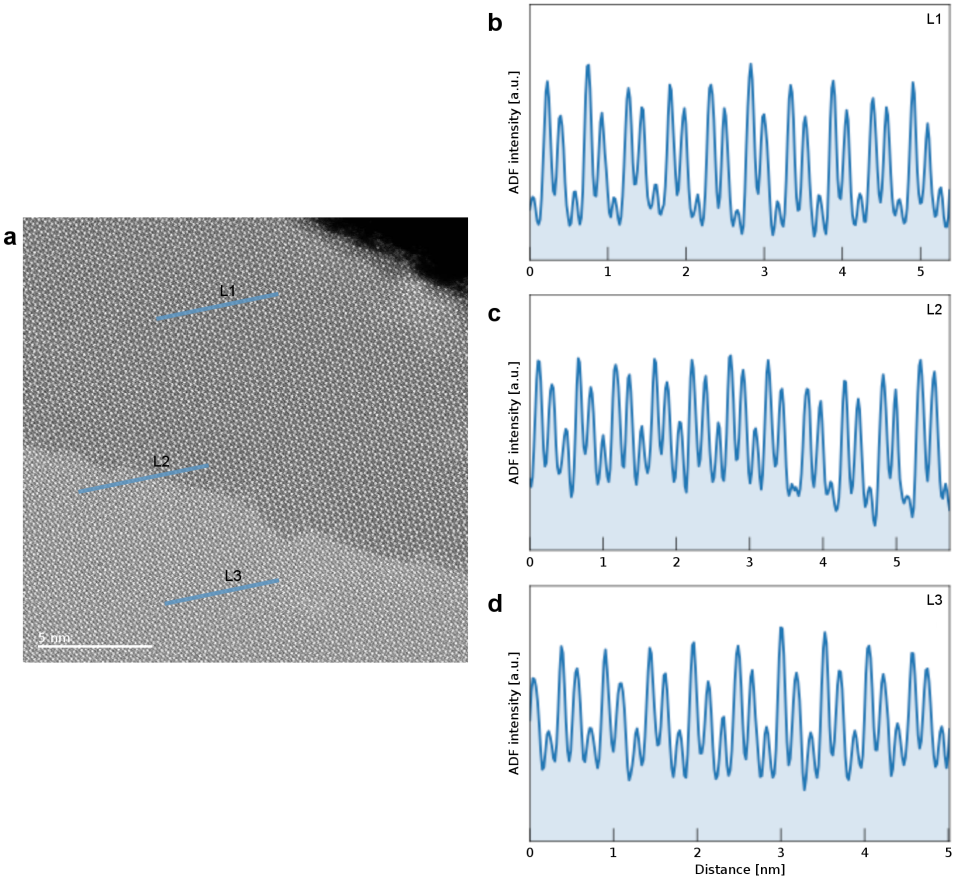

Figure A.3: (a) Atomic resolution STEM image corresponding to a representative WS_2 petal, specifically the region shown in Figure A.2c. (b-d) ADF intensity profiles acquired along the blue lines indicated in (a). The three profiles display the same three-fold periodicity, further confirming the underlying 2H/3R crystallographic nature of the WS_2 flake.

B

SUPPLEMENTARY MATERIALS TO CHAPTER 5

Parts of this chapter have been published as the supplementary information of *Advanced Functional Materials* **34**, 2307893 (2024) by **S. E. van Heijst**, M. Bolhuis, A. Brokkelkamp, J. J. M. Sangers, and S. Conesa-Boj.

B.1. DATA PROCESSING OF EELS SPECTRAL IMAGES

B.1.1. BANDGAP ENERGY UNCERTAINTY ESTIMATION IN TWISTED WS_2

As discussed in Section 3.2.2 of Chapter 3 the Monte Carlo replica method is used in order to obtain a faithful estimate of the uncertainties associated to the modeling and subtraction of the zero-loss peak (ZLP). Figures 5.2c-d in Chapter 5 depict the local relative uncertainty of the bandgap energy in the twisted tungsten disulfide (WS_2) specimens yielding from the analysis of their electron energy-loss spectroscopy (EELS) spectral images via this method. For both these twisted WS_2 specimens, a subset of pixels are observed with relatively high uncertainties when comparison to the rest of the specimen.

To investigate the origin of these, and demonstrate their validity within the error estimation approach, three individual subtracted inelastic EEL spectra and their bandgap fitting are inspected. These spectra are extracted from specific regions of the stacked flakes specimen, as marked in Figure B.1a. More specifically, these regions are located at the edge (marked by a circle), near the edge (marked by a square), and in the center (marked by a diamond) of the specimen. While the relative uncertainty near the edge is relatively large, the other regions present with a smaller relative uncertainty. Figures B.1b-d display the individual subtracted inelastic EEL spectra (I_{inel}) within the aforementioned locations, together with the best-fit and associated uncertainty used to extract the bandgap energy.

This analysis indicates that higher relative uncertainties in the determination of the bandgap energy observed in some of the pixels in the region near the edge are associated to the presence of additional structures in the subtracted inelastic EEL spectrum which affect the fitting. These could be related to specific electronic transitions or also be explained to increased levels of stochastic noise. Nevertheless, one concludes that the somewhat larger uncertainties affecting the determination of the bandgap energy in this region are genuine and faithfully estimated within our approach, and reflect the large fluctuations in the subtracted inelastic EEL spectra used for the bandgap fitting.

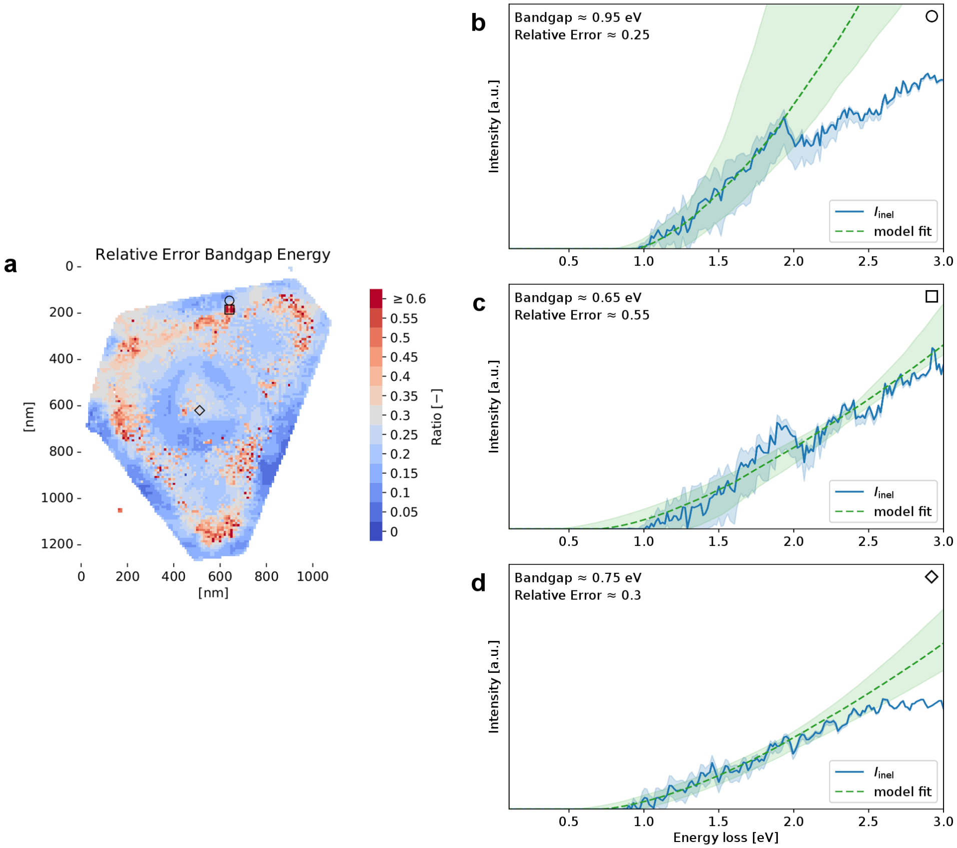

Figure B.1: The subtracted inelastic EEL spectra I_{inel} in three different regions (indicated in (a)) in the stacked flakes specimen: (b) at the edge (circle), (c) near the edge (square), and (d) in the center (diamond). The best-fit and uncertainty for the model of I_{inel} in the onset region, which are used to extract the bandgap energy, are also given. Note that some pixels near the edge regions exhibit additional structures in this onset region, which results in larger uncertainties in the bandgap energy determination.

B.1.2. LOCAL THICKNESS MAPPING OF TWISTED WS_2

In addition to the bandgap energy, the EELSFITTER framework also allows for the extraction of local thickness information from EELS spectral images (Section 3.2.4 of Chapter 3). The spatially-resolved thickness maps of the twisted WS_2 specimens discussed in Chapter 5 are presented in Figures B.2a-b. These maps also include the contribution from the underlying substrate composed of the 5 nm-thick silicon nitride (Si_3N_4) film of the transmission electron microscopy (TEM) microchip.

Figure B.2a displays the thickness map of the stacked flakes specimen shown in Figure 5.1a in Chapter 5, revealing its layered structure. The base flake exhibits a maximum thickness of approximately 29 nm. When the smaller flake is stacked on top, the specimen reaches a maximum thickness of 91 nm. The corresponding map of relative uncertainty is displayed in Figure B.2c, indicating that these are very small except for pixels at the very edge of the specimen.

Figure B.2b showcases the thickness map of the twisted flake depicted in Figure 5.1b in Chapter 5, highlighting its spiraling nature. The map indicates a maximum height of 60 nm at the center of the flake. Also here, uncertainties associated to the thickness determination (Figure B.2d) are essentially negligible.

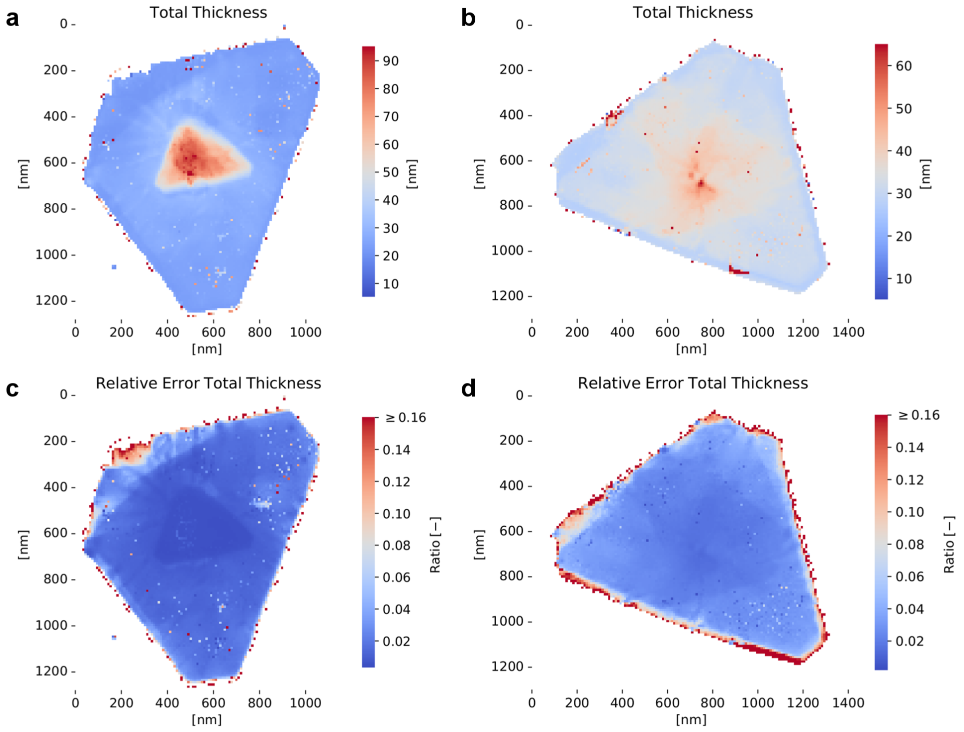

Figure B.2: (a-b) Spatially-resolved maps showing the combined thickness of the twisted WS_2 specimens (Figure 5.1 in Chapter 5) and the underlying 5 nm Si_3N_4 film substrate. (c-d) Relative errors of the thickness maps from (a-b). A mask is applied to exclude pixels corresponding to the substrate.

B.2. MAPPING STRAIN DISTRIBUTIONS IN TWISTED WS$_2$ WITH 4D STEM-EMPAD

B.2.1. ADDITIONAL SPATIALLY-RESOLVED STRAIN MAPS OF A TWISTED WS$_2$ FLAKE

In Section 5.3.2 of Chapter 5 we discuss the details regarding the extraction of information on the strain fields and deformation angle of the twisted flake from its four-dimensional (4D) dataset acquired by employing 4D scanning transmission electron microscopy (STEM) coupled with an electron microscope pixel array detector (EMPAD). The resulting spatially-resolved maps for the shear strain (ε_{xy} and $\varepsilon_{x'y'}$) and deformation angle (θ) are presented in Figures 5.5d-g in Chapter 5. Furthermore, the analysis provides insights into the strain fields along the x-/x'- and y-/y'-directions, which are depicted in Figures B.3a-b and B.3c-d, respectively.

Remarkably, these spatially-resolved maps exhibit a consistent strain distribution characterized by abrupt transitions near the three corners of the flake, as described in Section 5.3.2 of Chapter 5 in the context of the shear strain.

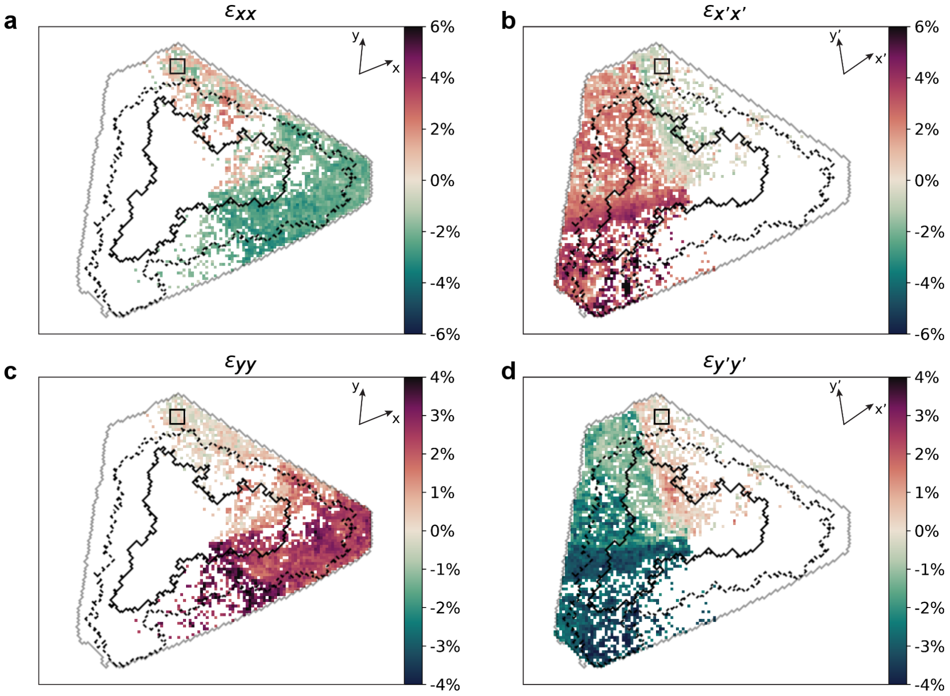

Figure B.3: Spatially-resolved strain maps for the (a-b) ε_{xx} and (c-d) ε_{yy} strain components obtained using the clusters denoted as (a,c) A and (b,d) B in Figure 5.5c in Chapter 5. The black square indicates the reference area. A slight Gaussian filter was applied to the maps to reduce outliers and enhance visualization. The overlaid lines represents a rough outline of the bandgap map shown in Figure 5.2b in Chapter 5, specifically indicating the crossing at 0.7 eV (dashed black line) and 0.8 eV (solid black line). The entire flake is outlined by the solid gray line.

B.2.2. Application of Gaussian Filter to Spatially-Resolved Strain and Deformation Angle Maps

The spatially-resolved strain and deformation angle maps, as shown in Chapter 5, were subjected to a Gaussian filter. This process results in more realistic maps by eliminating point outliers and smoothing the pixelated nature of the unfiltered maps. To highlight this functionality, Figures B.4, B.5, and B.6 depict the strain and deformation angle maps before the Gaussian filtering was applied. These unfiltered maps were obtained using the same method as their filtered counterparts.

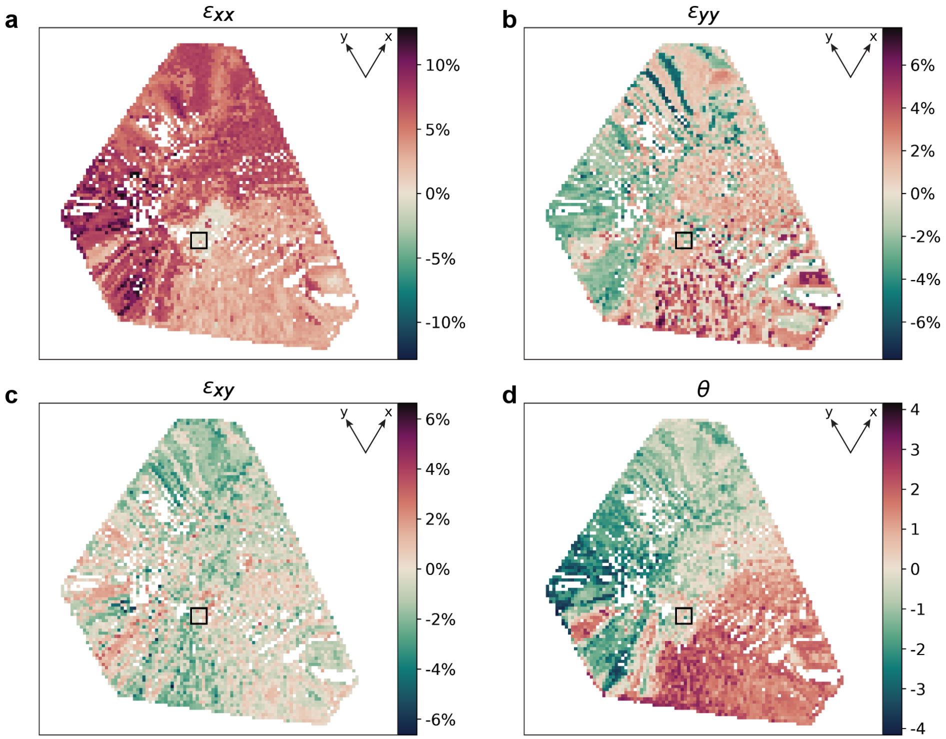

Figure B.4: Spatially-resolved strain and deformation angle maps of the stacked flakes specimen (Figure 5.1a in Chapter 5), as shown in Figures 5.4d-g in Chapter 5, before the application of a Gaussian filter. The strain maps are divided into ε_{xx}, ε_{yy}, and ε_{xy} components. Here, ε_{xx} and ε_{yy} represent strain in the x and y directions respectively, indicating how much the material has been stretched or compressed along these axes, while ε_{xy} represents shear strain. The black square indicates the reference area.

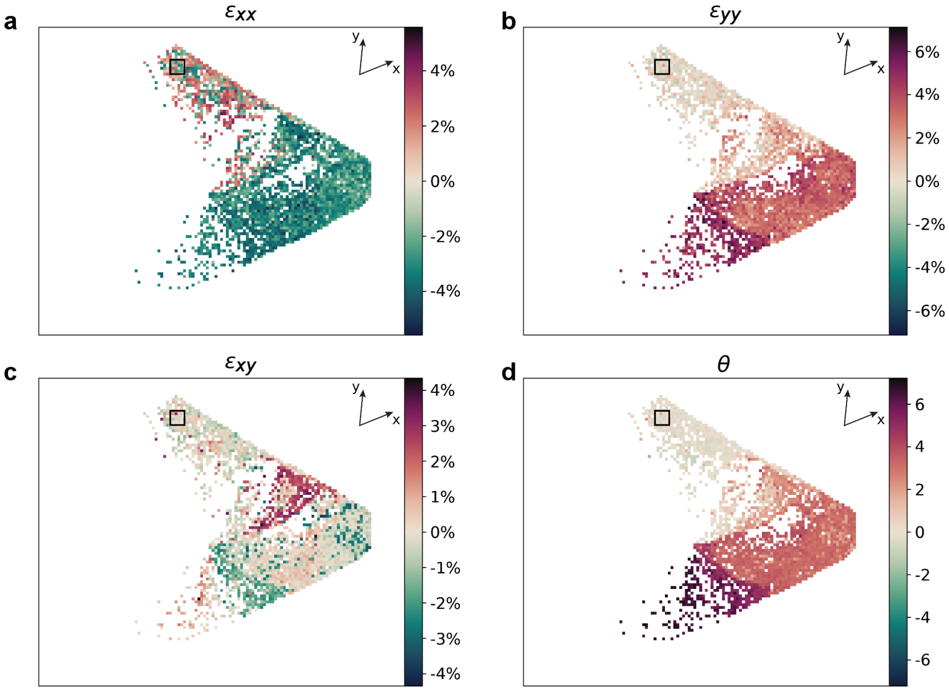

Figure B.5: Spatially-resolved strain and deformation angle maps for the twisted flake (Figure 5.1b in Chapter 5), as shown in Figures 5.5d,f in Chapter 5 and Figures B.3a,c, before the application of a Gaussian filter. The strain maps are divided into ε_{xx}, ε_{yy}, and ε_{xy} components. Here, ε_{xx} and ε_{yy} represent strain in the x and y directions respectively, indicating how much the material has been stretched or compressed along these axes, while ε_{xy} represents shear strain. The black square indicates the reference area.

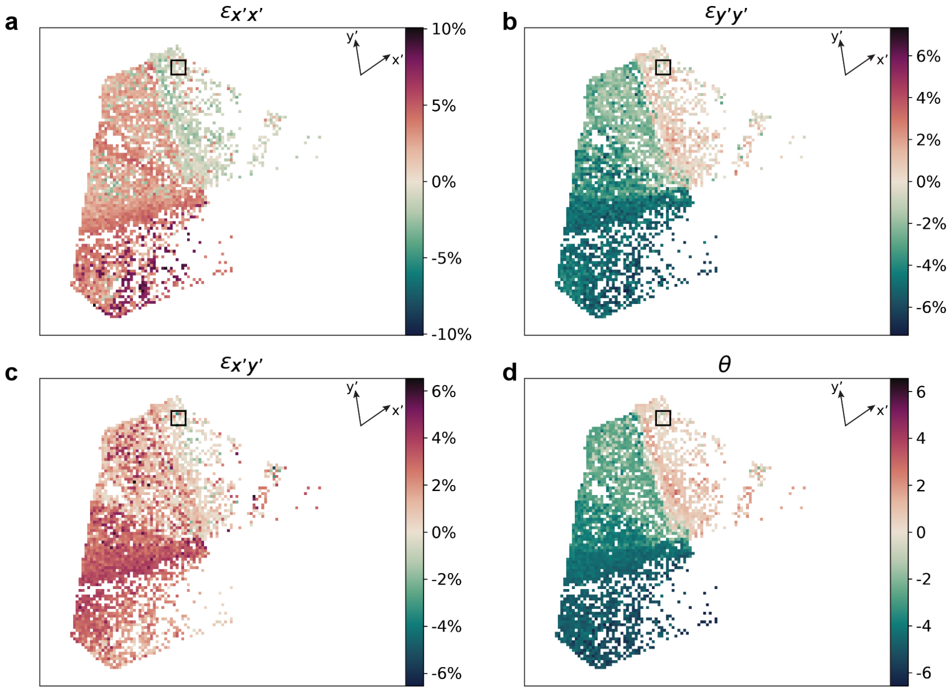

Figure B.6: Spatially-resolved strain and deformation angle maps for the twisted flake (Figure 5.1b in Chapter 5), as shown in Figures 5.5e,g in Chapter 5 and Figures B.3b,d, before the application of a Gaussian filter. The strain maps are divided into $\varepsilon_{x'x'}$, $\varepsilon_{y'y'}$, and $\varepsilon_{x'y'}$ components. Here, $\varepsilon_{x'x'}$ and $\varepsilon_{y'y'}$ represent strain in the x' and y' directions respectively, indicating how much the material has been stretched or compressed along these axes, while $\varepsilon_{x'y'}$ represents shear strain. The black square indicates the reference area.

B.3. HAADF-STEM ANALYSIS OF TWISTED WS_2: REVEALING ATOMIC-SCALE STRUCTURE

Various observations related to the correlation between bandgap energy, thickness and strain were made during the analysis of the twisted WS_2 morphologies presented in Figure 5.1 in Chapter 5. To further investigate these observations, a high-angle annular dark-field (HAADF) STEM analysis was conducted on both specimens.

First, the stacked flakes specimen is examined. Figures B.7b-c show the resulting HAADF-STEM images at two distinct regions on the base flake, marked by the white diamond and circle in the low-magnification STEM image in Figure B.7a, respectively. Both regions exhibit a well-ordered atomic-scale structure, as clearly seen in the HAADF-STEM images. The corresponding fast Fourier transforms (FFTs), as shown in the insets, also display a distinctly singular hexagonal diffraction pattern, which is a characteristic feature of the ordered WS_2 structure.

Next, the twisted flake was investigated. HAADF-STEM images were obtained at two positions marked in the low-magnification STEM image shown in Figure B.7d. These HAADF-STEM images (Figures B.7e-f) reveal the presence of Moiré patterns within the studied areas. The multiplicity in the FFTs (insets) corresponding to these HAADF-STEM images further confirms the existence of these Moiré patterns.

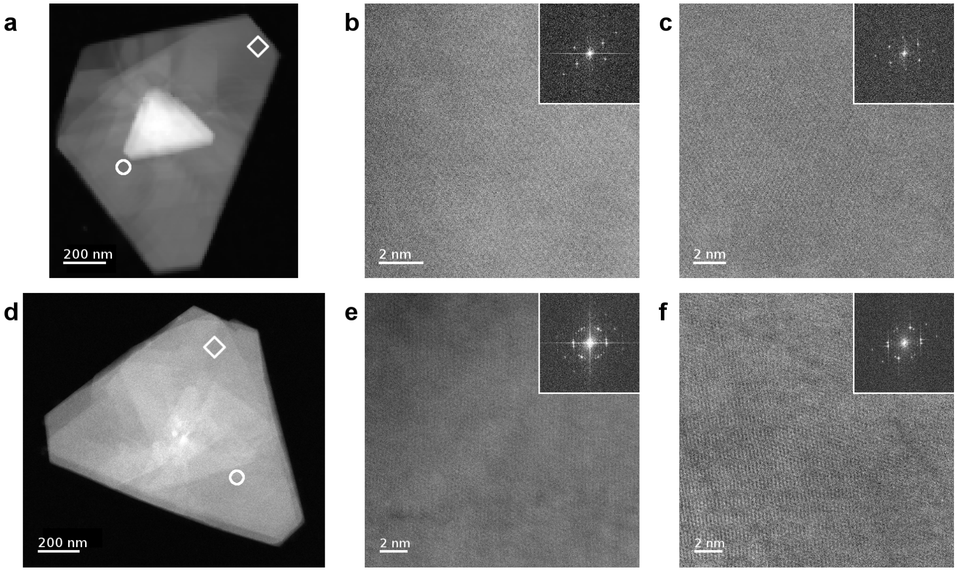

Figure B.7: Low-magnification STEM image of (a) the stacked flakes specimen, and (d) the twisted flake. HAADF-STEM image and corresponding FFT (insets) of the areas marked in (a) at (b) one of the tips of the base flake (white diamond), and (c) close to a tip of the smaller flake (white circle), as well as those of the areas marked in (d) by (e) a white diamond, and (f) a white circle.

C

TRANSMISSION ELECTRON MICROSCOPY ACQUISITION DETAILS

C.1. ACQUISITION DETAILS OF CHAPTER 3

The annular dark-field (ADF) scanning transmission electron microscopy (STEM) imaging and electron energy-loss spectroscopy (EELS) measurements, displayed in Figure 3.2, were performed on an ARM200F Mono-JEOL microscope. The microscope was operated at 200 kV with the monochromator ON and a slit of 1.3 µm inserted. A Gatan GIF Quantum ERS system (model 966) was used for the EELS analyses. The convergence and collection semi-angles were 19.96 and 14.5 mrad, respectively. The spectral resolution, defined by the full width at half maximum (FWHM) of the zero-loss peak (ZLP), achieved under these conditions is around 120 meV. EEL spectra were acquired with an entrance aperture diameter of 5 mm, energy dispersion of 0.015 eV/channel, and pixel time of 0.5 s. The camera length used for both the EELS analysis and STEM imaging was 12 cm. Following acquisition, the data was analyzed using the open-source analysis framework EELSFITTER, yielding the maps shown in Figures 3.3 through 3.5.

The acquisition of the four-dimensional (4D) STEM datasets, as depicted in Figures 3.6 and 3.8, was done using a Titan Cube microscope equipped with an electron microscope pixel array detector (EMPAD) optimized for 4D-STEM. The microscope was operated at 300 kV in STEM nanoprobe mode. Figure 3.6 displays a dataset acquired on a twisted tungsten disulfide (WS_2) specimen. In this case, the convergence semi-angle was reduced to 2.63 mrad using a 50 µm condenser (C2) aperture and a camera length of 285 mm. Acquisitions were carried out at 1 ms exposure time for 128 × 128 real-space pixels (scan positions). For each of these pixels, the EMPAD detector records a nanobeam diffraction pattern of 128 x 128 pixels. Similarly, for the twisted molybdenum-/tungsten diselenide ($MoSe_2$/WSe_2) heterostructure (Figure 3.8a), the convergence semi-angle was reduced to 0.53 mrad using a 10 µm condenser (C2) aperture and a camera length of 285 mm. Acquisitions were carried out at 5 ms exposure time. Analysis of the datasets was performed using the open-source analysis framework STRAINMAPPER, producing the results reported in Figures 3.6, and 3.9 through 3.11.

The Titan Cube microscope was also used to collect the high-resolution STEM images shown in Figure 3.8b-c. Again the microscope was operated at 300 kV.

C.2. ACQUISITION DETAILS OF CHAPTER 4 AND APPENDIX A

The low magnification ADF-STEM imaging and energy-dispersive X-ray spectroscopy (EDS) measurements, presented in Figures 4.1c and 4.1e respectively, were performed using a Titan Cube microscope operated at 300 kV.

The ADF- and bright-field (BF-) STEM images and the EELS measurements displayed in Figures 4.1d, 4.2 through 4.5, A.2, and A.3 were instead taken using a JEOL ARM200F microscope with a cold field-emission gun operated at 60 kV. This microscope is equipped with an aberration probe corrector and a Gatan GIF Quantum spectrometer. The convergence and collection semi-angles were set to 30.0 and 66.7 mrad, respectively. The spectral resolution (FWHM of the ZLP) achieved under these conditions is around 450 meV. The EEL spectra of Figure 4.5a were acquired with an entrance aperture diameter of 5 mm, energy dispersion of 0.025 eV/channel, and exposure time of 0.001 s. The camera length used was 12 cm. Following acquisition, this data was analyzed using the open-source analysis framework EELSFITTER, giving the results shown in Figures 4.5b and 4.6.

C.3. ACQUISITION DETAILS OF CHAPTER 5 AND APPENDIX B

The ADF-STEM imaging and EELS measurements of the specimens as displayed in Figure 5.1, were performed on an ARM200F Mono-JEOL microscope. The microscope was operated at 200 kV with the monochromator ON and a slit of 1.3 µm inserted. A Gatan GIF Quantum ERS system (model 966) was used for the EELS analyses. The convergence and collection semi-angles were 19.96 and 14.5 mrad, respectively. The spectral resolution (FWHM of the ZLP) achieved under these conditions is around 120 meV. EEL spectra were acquired with an entrance aperture diameter of 5 mm, energy dispersion of 0.015 eV/channel, and pixel time of 0.5 s. For both the EELS analyses and STEM imaging a camera length of 12 cm was used. Following acquisition, the data was analyzed using the open-source analysis framework EELSFITTER, providing the results as shown in Figures 5.2, 5.3, B.1, and B.2.

The high-resolution STEM images in Figure B.7 were also collected using the ARM200F Mono-JEOL microscope. During imaging the microscope was operated at 200 kV. The convergence semi-angle and camera length were 19.82 mrad and 8 cm, respectively.

The 4D STEM measurements, as reported on in Figures 5.4 and 5.5, were conducted using a Titan Cube microscope equipped with an EMPAD optimized for 4D-STEM. The microscope was operated at 300 kV in STEM nanoprobe mode. The convergence semi-angle was reduced to 2.63 mrad using a 50 µm condenser (C2) aperture and a camera length of 285 mm. Acquisitions were carried out at 1 ms exposure time for 128 × 128 real-space pixels (scan positions). For each of these pixels, the EMPAD detector records a nanobeam diffraction pattern of 128 x 128 pixels. Analysis of the datasets was performed using the recently developed STRAINMAPPER framework, producing the results reported in Figures 5.4, 5.5, and B.3 through B.6.

CURRICULUM VITÆ

Sabrya Esther VAN HEIJST

23-01-1996 Born in Rotterdam, The Netherlands

EDUCATION

2008–2014 **Voortgezet Wetenschappelijk Onderwijs** (*cum laude*)
Gemini College Ridderkerk, Ridderkerk, The Netherlands

2014–2017 **Bachelor of Science in Applied Physics**
Delft University of Technology, Delft, The Netherlands
Thesis: The effect of Al_2O_3 coating on the dewetting of thin gold films
Supervisor: Prof. dr. H. W. Zandbergen

2017–2019 **Master of Science in Applied Physics**
Delft University of Technology, Delft, The Netherlands
Thesis: Synthesis of tungsten disulphide using atmospheric pressure chemical vapour deposition
Supervisor: Dr. S. Conesa-Boj

2019–2024 **PhD in Physics**
Delft University of Technology, Delft, The Netherlands
Thesis: Fingerprinting the Properties of WS_2 Nanostructures using Advanced Transmission Electron Microscopy Techniques: From Growth to Characterization
Promotors: Dr. S. Conesa-Boj and Prof. dr. L. Kuipers

LIST OF PUBLICATIONS

10. M. Bolhuis, **S. E. van Heijst**, J. J. M. Sangers, and S. Conesa-Boj., *4D-STEM Nanoscale Strain Analysis in van der Waals Materials: Advancing beyond Planar Configurations*, Small Science **4**, 2300249 (2024)
9. **S. E. van Heijst**, M. Bolhuis, A. Brokkelkamp, J. J. M. Sangers, and S. Conesa-Boj., *Heterostrain-Driven Bandgap Increase in Twisted WS_2: A Nanoscale Study*, Advanced Functional Materials **34**, 2307893 (2024)
8. I. Komen, **S. E. van Heijst**, M. Caldarola, S. Conesa-Boj, and L. Kuipers, *Revealing the nanogeometry of WS_2 nanoflowers by polarization-resolved Raman spectroscopy*, Journal of Applied Physics **132**, 173103 (2022)
7. A. Brokkelkamp, J. ter Hoeve, I. Postmes, **S. E. van Heijst**, L. Maduro, A. V. Davydov, S. Krylyuk, J. Rojo, and S. Conesa-Boj, *Spatially Resolved Band Gap and Dielectric Function in Two-Dimensional Materials from Electron Energy Loss Spectroscopy*, The Journal of Physical Chemistry A **126**, 1255 (2022).
6. L. Maduro, **S. E. van Heijst**, and S. Conesa-Boj, *First-Principles Calculation of Optoelectronic Properties in 2D Materials: The Polytypic WS_2 Case*, ACS Physical Chemistry Au **2**, 191 (2022).
5. I. Komen, **S. E. van Heijst**, S. Conesa-Boj, and L. Kuipers, *Morphology-induced spectral modification of self-assembled WS_2 pyramids*, Nanoscale Advances **3**, 6427 (2021).
4. **S. E. van Heijst**, M. Mukai, E. Okunishi, H. Hashiguchi, L. I. Roest, L. Maduro, J. Rojo, and S. Conesa-Boj, *Illuminating the Electronic Properties of WS_2 Polytypism with Electron Microscopy*, Annalen der Physik **533**, 2000499 (2021).
3. L. I. Roest, **S. E. van Heijst**, L. Maduro, J. Rojo, and S. Conesa-Boj, *Charting the low-loss region in electron energy loss spectroscopy with machine learning*, Ultramicroscopy **222**, 113202 (2021).
2. M. Bolhuis, J. Hernandez-Rueda, **S. E. van Heijst**, M. Tinoco Rivas, L. Kuipers, and S. Conesa-Boj, *Vertically-oriented MoS_2 nanosheets for nonlinear optical devices*, Nanoscale **12**, 10491 (2020).
1. M. O. Cichocka, M. Bolhuis, **S. E. van Heijst**, and S. Conesa-Boj, *Robust Sample Preparation of Large-Area In- and Out-of-Plane Cross Sections of Layered Materials with Ultramicrotomy*. ACS Applied Materials & Interfaces **12**, 15867 (2020)

ACKNOWLEDGEMENTS

How lucky I am to have something that makes saying goodbye so hard

- Author disputed

Now, here we are, at the end of my thesis and at the end of my journey at the TU Delft. This university has been my second home ever since I started my bachelor in 2014. During my time here I have met a lot of amazing people. Not only during my student days, but also within my time as a PhD candidate. Without them my time here would not have been the same. I feel blessed to have been part of the environment that was created though their presence, support and laughter. In this final section of my thesis, I hope to convey my appreciation for all of these individuals.

The first person I want to express my gratitude to is my supervisor and promotor, **Sonia**. I have a picture saved on my phone from the first time we met. I had just started my master's, and signed up for the Quantum Nanoscience (QN) lab tours. Your lab was one of those we visited that day. I have a vague recollection of all of us trying to sit on the couch in your office for a presentation. Your enthusiasm and, of course, also the cool science you guys were doing made me take a picture of your TU badge, just so I could look into your lab some more later. At that moment I didn't know it yet, but a year later I would be part of your group as a MEP student and another year after that I would join as a PhD student. I'm grateful to have been part of your group. In my eyes you have created a beautiful space where people can grow and blossom. Thanks for all the help you provided to me over the years, pushing my boundaries, and believing in me. You helped me grow into the researcher and person I am today. I would also like to thank my second promotor, **Kobus**. Our meetings might not have been that frequent, but whenever we did meet you always showed trust in my progress and encouraged me to push for everything I wanted to learn. As someone slightly more removed from my research, your insights always gave me food for thought. I appreciate all of those moments, and enjoyed working together.

Next I would like to thank all of the wonderful people I had the pleasure of working alongside of in the **ConesaBoj Lab**. I would like to start this long list with the people I started with as a master student, the original core of our lab. **Miguel**, despite our limited time working together, you taught me a lot. Most importantly, you mentored me on the CVD, a device I would keep on using until the very last day of my PhD. But I also look back fondly on our other training sessions. The random conversations we would have during those always managed to calm my nerves. It was a pleasure to work with you at the start of my journey, and it is amazing to have you here at the end as part of my committee.

Luigi, you were my (and most of QNs) mentor in all things cleanroom. Thank you for taking me under your wing, and teaching me almost everything I know about nanofabrication and working in a cleanroom. Your knowledge, patience and humor made each moment working together a joy. I learned a lot from you, on various fronts, and have tried to apply all this knowledge and wisdom in guiding and training the "next generation" of people in our lab. **Maarten**, my partner in crime from the very start of my journey in this group. As master students we started only a few months apart and with similar projects. Yet, to me, you were always the person with all the experience; someone I looked up to. When you decided to join for a PhD too, I was really happy. You have made me feel at home in this group, and in my projects. I could always come to you with any of my questions and dilemmas. You were ready to answer or spar about them all, and did so without ever making me feel insecure about asking. Your readiness to help and guide is admirable. Thanks for all the great times and amazing memories.

Since then the group has grown and many new people have joined. **Abel**, you started your master project when all the chaos of COVID was just starting. Your project got changed from experimental to theoretical halfway through, but this didn't seem to faze you. I applaud the flexibility and calmness you showed then, and have continued to show during your time as a PhD candidate. Working with you was a blast, and I'm grateful for all the help you offered me with all things Python and EELSFITTER. Despite all the trouble these sometimes caused me, with your tireless help my codes would always start running again, allowing some of the beautiful results that are part of this thesis. **Chris**, it is a good thing I didn't scare you off the first time you visited during your application process, because you are an asset to our lab. Your enthusiasm on every project you are part of is contagious. You are full of ideas and I hope you get to try it all. I want to thank you for your patience with me. Not only did you have to wait on me before starting your training, but you also had to deal with me having a hard time letting go of some unfinished projects. But, through it all, we still had some really fun times. I really enjoyed working with you, and wish you the best of luck on the rest of your PhD. **Jeroen**, the latest to join us as a PhD candidate, but not a stranger to our lab. I hope you continue to make everyone laugh through your ability to see animals in the flakes you exfoliate. The farm is getting a bit full, but with your latest discovery (a penguin) maybe a zoo can be next. After I am gone, you will be moving to my desk. I hope you will have as many good memories behind it as I have. And finally, our current master students **Steven**, **Christina** and **Philip**. You guys are doing some amazing science, keep it up and be not afraid to follow your curiosity down new paths.

In addition, our lab has an extensive list of alumni who I had the pleasure of working with. First our mostly experimental members: **Magdalena**, **Stef**, **Assunta**, **Rose**, **Yashoda**, and **Jorien**. I worked with you all to varying extents, and enjoyed seeing what unique qualities each of you brought to our team. From postdoc to BEP student, you all did amazing work and brought new insights to our lab. I learned a lot from all of you during the time we spend together, and I hope to also have instilled some wisdom onto you all in return. And of course we can't forget about all our mostly theoreticians: **Helena**, **Laurien**, **Isabel**, **Ruben**, **Boran**, **Stijn**, **Olivier**, **Martijn**, **James**, and **Patricia**. Even though your projects were often beyond my comprehension, I enjoyed hearing about it all in conversation and our group meetings. A lot of work you guys did, ended up being the foundation of the tools I have used throughout my PhD. I have the highest respect for you all. In terms of theory we also got some help from outside of our lab. Thank you **Juan** and **Jaco** for all your input. A little birdie also told me I have **Juan** to thank for all the baked goods (chocolate cake) supplied for successful CVD experiments, so thank you.

Another group of people that I could always fall back on were my office mates, in particular **Irina** and **Rasa**. **Irina**, we were not only office mates, but also collaborators. I'm happy I could provide you with some nice samples, and loved to see the amazing work you did with them. In our office you were a force to be reckoned with. Your hard work not only inspired me to do the same, but also always helped me find my motivation on days that I felt none. But of course we didn't just work in our office, there was also more than enough time reserved for fun. Over the years, you, me and **Rasa** would share a lot of conversations and (mostly your guys') baked goods, and I enjoyed every moment. **Rasa**, with your positive and cheerful personality you always managed to put me in a good mood. I found a confidant in you with whom I could share both the good and bad. Thank you for being so welcoming to me, and for all the moments we shared together. Also a shout-out to the office mates that join me in D114 more towards the end of my PhD journey. Thank you **Daniël** and **Sercan** for your understanding and patience during this time, especially while I was writing my thesis.

In addition to all the amazing people I have already mentioned, I would meet many more that would shape my time in the QN department. Firstly, a constant throughout my time here were the members of the **NanoOptics group**, especially **Irina**, **Marc**, **Sonakshi**, **Thijs**, **Daniël**, and **Onima**. Not only did I have the pleasure of having some of you as my office mates, and collaborators. But you guys would also always be there at the lunch table, and even once joined our lab at a group outing. Thanks for all the moments we shared. Next, some honorable mentions for my office mates. As master students, Maarten and I spend some time in F190. **Dima** and **Jorrit**, thanks for putting up with us master students and making us feel welcome in your office. I really enjoyed your company for those first months. Of course I should also not forget to mention the reasons why we had to move to a master room in the end. **Brecht** and **Joris**, don't worry I never held it against you. You guys were an amazingly fun addition to our department. I would also like to give a special thanks to **Jana**. I have enjoyed all our conversations over lunch. But when we had barely met, you also saved me for having a very lonely breakfast during my last NWO Physics (Physics@Veldhoven). I wish we would have gotten to know each other just a bit earlier so we could have been roommates too. Next, I want to thank **Alex**, who I got to work alongside of as a teaching assistant when he replaced **Sonia** in the minor course Mathematics for Quantum Physics. I had a good time working with you. Also, I'm grateful for the time you took to talk to me about your teaching position when I was interested in maybe applying for such a position too. Though it ended up not being for me, I can see it fits you perfectly and wish you luck on this beautiful career path. Finally, also many thanks to **Thierry**, **Mattias**, **Nicco**, **Lorenzo**, **Parsa**, **Nina**, **Laëtitia**, **Lukas**, **Evert**, **Iacopo**, **Gesa**, **Michael**, and everyone else I had the pleasure of interacting with over the years. You guys have made my time in the QN department incredibly memorable.

During both my master and PhD projects I had the pleasure of working in various lab settings and with a lot of different devices. This is an aspect of my job as an experimental physicist that I really enjoyed. However, none of it would be possible without the tireless efforts of the next group of people I want to express my thanks to. Firstly, the entirety of the **Kavli Nanolab staff**. It is your expertise, willingness to help, and careful maintenance of the cleanroom and associated equipment that allows people like me to work with such pleasure in this space. In particular I want to thank, **Roald**, **Hozanna**, **Charles**, **Eugene**, and **Pauline** for all the help and expertise you offered me over the years on your respective fields and setups. Additionally, I want to express my gratitude to the (research) technicians within our own department and beyond: **Tino**, **Tom**, **Dustin**, **Allard**, and **Frans**.

The last group within the QN department that should not be forgotten within my acknowledgements is our amazing non-technical support staff, including **Etty**, **Lidewij**, **Heleen**, **Anita**, **Karin**, and **Erika**. Thank you for all you do for our department.

Last but certainly not least I want to thank my support system outside of the TU Delft, both **friends and family**. Laat ik beginnen bij mijn geweldige vriendengroepen: mijn oudste vriendin vanuit de basisschool nog, **Mariska**, en mijn vriendinnen die ik heb ontmoet op de TU Delft, **Elise**, **Amber** en **Joanne**. Ondanks dat we elkaar misschien niet meer zoveel zien of spreken als voorheen, voelt het elke keer als we dat wel doen weer alsof het gisteren was. Ik kan altijd enorm genieten van elke verjaardag, spelletjes-dag of bijklets-moment waarop ik jullie weer zie. Heerlijk kunnen we dan kletsen niet alleen over serieuzere dingen, maar ook juist over koetjes en kalfjes. En dat laatste was op sommige momenten in deze afgelopen jaren precies wat ik nodig had. Bedankt dat jullie zijn wie je bent, en dat ik jullie vriendinnen mag noemen.

En tot slot, wil ik mijn gezin bedanken. Jullie weten als geen ander dat ik niet altijd goed ben in het omschrijven, laat staan opschrijven, van mijn emoties en gevoelens. Gelukkig kennen jullie me ook goed genoeg, dat die woorden niet altijd nodig zijn. Toch heb ik wat woorden voor jullie om mijn dankbaarheid te uiten. Jullie hebben mij altijd het gevoel gegeven van vertrouwen en geloof in mijn kunnen. Ik denk dat jullie op sommige momenten mogelijk meer in mij geloofden dan ik in mezelf, en dat waardeer ik enorm. Daarbij kwam jullie continue belangstelling voor waar ik me mee bezig hield, of wat er bij mij speelde. Op het gebied van werk kon ik misschien niet altijd precies in detail uitleggen wat ik aan het doen was, maar ik kon wel altijd me ei kwijt bij jullie. Dit heeft me door veel stressvolle periodes heen geholpen. Ik ben jullie hier ontzettend dankbaar voor, en mogelijk heb ik dat niet vaak genoeg gezegd. Bedankt voor alle steun en liefde; ik hou van jullie.

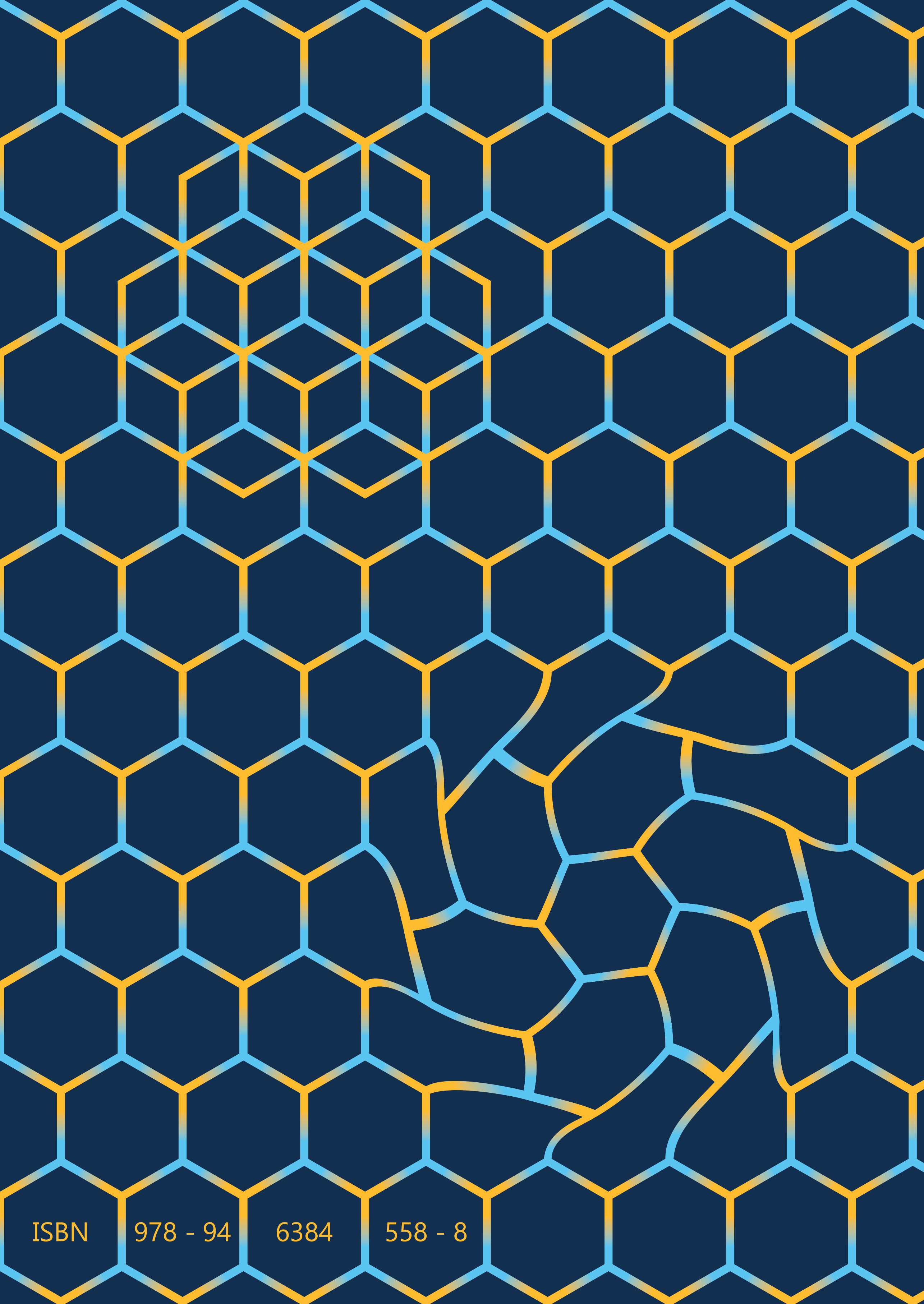

ISBN 978 - 94 6384 558 - 8